Doctoral Thesis

FUNDAMENTAL STUDY ON QUENCHING TECHNIQUE AND DECAYING PROCESSES OF ARC PLASMAS USING SOLID AND GAS MEDIA

Kanazawa University
Graduate school of Natural Science and Technology
Electrical Engineering and Computer Science

Student ID   1524042002

TOMOYUKI NAKANO

Supervisers
Prof.   Yasunori Tanaka
Prof.   Yoshihiko Uesugi
Prof.   Tatsuo Ishijima

December, 2017

Contents

List of Figures

List of Tables

Acknowledgement

First of all, the author would like to express gratitude to Prof. Yasunori Tanaka for devoted supervision. Without his help and devoted supervision, the author could not achieve the research described in this thesis.

The author also would like to express gratitude to Prof. Yoshihiko Uesugi and Prof. Tatsuo Ishijima for their time and help on the author's research works.

The author wants to thank Assis. Prof. Kentaro Tomita in Kyushu University and Assis. Prof Yuki Inada in Saitama University for their supervision and cooperation in the long-term experiments conducted for our research. The author learned a lot of important things through discussions with them. The author was happy to conduct experiments with Sirs. Similarly, the author thanks Prof. Katsumi Suzuki, Prof. Takeshi Shinkai, Assoc. Prof. Takayasu Fujino and Mr. Takanori Iijima for their partnership in the work the author participated in. It was honor for the author to discuss about interesting physics and phenomena with them.

The author also wants to thank a doctoral student, Mr. Naoto Kodama in the Electric Power and Environment Laboratory for many helps not only for the author's research but also student life. He is important partner of the author in spite of having different research themes each other. Additionally, the author would like to thank Mr. Kosuke Murai, Takuya Nakagawa and Yuto Utsunomiya, who were juniors of the author when the author started a doctoral work. Mr. Murai and Nakagawa were superior to the author in some fields and then the author was supported by them. Mr. Utsunomiya gave the author a lot of encouragements and fun times. The author also thanks all of the member of the Electric Power and Environment Laboratory.

Finally, many thanks are given to parents and grand parents of the author for devoted supports and care of the author. Without their helps, the author's research work was difficult to be achieved.

Abstract

Circuit breakers play important roles for secure electric power transmission. The most important duty of a circuit breaker is to interrupt a fault current, which may cause serious damages to humans or equipments. Therefore, installation of circuit breakers is essential both in low voltage system and high voltage system. Nowadays, number of electric generators that use renewable energy is increasing in low voltage system, such as solar power generators. In many cases, they provide direct current and the direct current is converted to alternating current. It is because direct current is not easily to be interrupted especially in short circuit faults. Increasing of direct current generator means that more and more high performance circuit breakers are needed to be equipped. In addition, DC power distribution prevails because of its high transmission efficiency. From the reasons above, low voltage circuit breakers are desired to improve their performance without high-costs. On the other hands, among high voltage circuit breakers, gas circuit breakers (GCBs) also have a big issue. SF_6 gas is widely used as arc quenching medium. However, its global warming potential is extremely high, 22800 times higher than that of CO_2 gas. Much efforts have been made for reduction of SF_6 use. Recently, strong candidates as alternatives to SF_6 has been developed. They are a mixture of CO_2 and perfluoronitrile (PFN) and that of CO_2, O_2 and perfluoroketon (PFK). Although strong candidates are existed, there are still unclear points about current interruption and arc quenching.

Arc quenching media made of polymer are often used in low voltage circuit breakers. For a high voltage circuit breaker, gas is often used for arc quenching. The author investigated arc quenching media in solid phase and gas phase with experiments and numerical approaches.

In the first research, the effect of water absorption in polyamide material irradiated by thermal plasmas was investigated on the occurrence of spallation phenomena. The interaction between polyamide materials and arc plasmas occurs particularly in the low voltage circuit breaker and aerospace fields. Spallation phenomena are those in which polymer

particles are ejected from polymer bulk materials irradiated by high heat flux. To confirm the effect of water absorption into the polyamide material on spallation phenomena, polyamide specimens with and without water absorption were irradiated by Ar inductively coupled thermal plasma. The results show that the polyamide specimen with water absorption ejected spallation particles, whereas the polyamide specimen without water absorption were only slightly ejected, indicating that water absorption promotes the occurrence of spallation. The cooling effects of the spallation polyamide 66 (PA66) particles ablation were also estimated in hot air to assess the arc quenching ability from the spallation particle inclusion. This estimation showed that 10 and more PA66 particles inclusion might decrease the air temperature by 3000 K effectively, which can be useful to enhance arc quenching in circuit breakers working in air.

Secondly, the arc quenching abilities of various gases were investigated using a power semiconductor switching technique fundamentally. The technique uses an insulated gate bi-polar transistor (IGBT) to inject current and apply voltage to the plasma arc. Using this technique, arcs in free recovery condition after a 50 A steady state condition were investigated in SF_6, CO_2, O_2, N_2, air and Ar gas flows. Furthermore, at a specific time high voltages of about 1.1 kV and 1.7 kV μs^{-1} were applied to the residual decaying arcs by the IGBT to elucidate the arc re-ignition process and recovery properties. These systematic experiments further enabled us to estimate the interruption probability versus the voltage application time. From these results, the voltage application time for 50% successful interruption was estimated for various gases, with the results showing a direct relation to the interruption capabilities of the respective gases. These results were then compared to the electron density measurement results and numerical simulation results to confirm their validity. All data obtained from the experiments and simulation is expected to be useful for elucidating the arc quenching physics and also for the practical application of arc quenching phenomena.

Finally, the author focused on the experimental approach to thermally arc re-ignition processes in various gas flow in a nozzle. Using the power semiconductor switches in the experimental system, the arc current and applied voltage to the arc were controlled with time accuracy. With this system, residual arcs were created in decaying phase under free recovery condition, and then arc re-ignition was intentionally made by application of

artificial voltage, i.e. quasi-transient recovery voltage, to study the arc behaviour in both decaying and re-ignition phases. In this study, SF_6, CO_2, N_2, O_2, air and Ar arcs were intentionally re-ignited by quasi-TRV application at 20 μs delay time from initiation of free recovery condition. Through these experiments, the electron density at the nozzle throat was measured using laser Thomson scattering (LTS) method together with a high speed video camera observation during re-ignition process. As results, temporal variations in the electron density from the arc decaying to re-ignition phases were successfully obtained for each gas-blast arc at the nozzle throat. In addition, dielectric recovery properties of SF_6, CO_2, air and Ar arcs were measured under the same condition except gas kinds. Results showed that a SF_6-blast arc decays faster than other gas-blast arcs in decaying phase, and also have a fast increase in the electron density in re-ignition phase. This may be reflected from the high arc quenching ability of SF_6.

These three approaches to investigation of arc quenching techniques firstly propose a new promising method for arc quenching in low voltage circuit breakers, and reliable data of arc quenching ability of various gas flow in a nozzle for high voltage circuit breakers. The author believes that the obtained results are useful for future development of smart grids and eco-friendly energy transport.

Chapter 1

Introduction

1.1 General background of circuit breaker

Circuit breakers play important roles for secure electric power transmission. The most important duty of a circuit breaker is to interrupt a fault current, which may cause serious damages to humans or equipments. Therefore, installation of circuit breakers is essential both in low voltage system and high voltage system. Nowadays, number of electric generators that use renewable energy is increasing in low voltage system, such as solar power generators [1, 2]. In many cases, they provide direct current and the direct current is converted to alternating current. It is because direct current is not easily to be interrupted especially in short circuit faults [3, 4]. Increasing of direct current generator means that more and more high performance circuit breakers are needed to be equipped. In addition, DC power distribution prevails because of its high transmission efficiency. From the reasons above, low voltage circuit breakers are desired to improve their performance without high-costs.

On the other hands, among high voltage circuit breakers, gas circuit breakers (GCBs) also have a big issue. SF_6 gas is widely used as arc quenching medium. However, its global warming potential is extremely high, 22800 times higher than that of CO_2 gas. Much efforts have been made for reduction of SF_6 use [5–10]. Recently, strong candidates as alternatives to SF_6 has been developed. They are a mixture of CO_2 and perfluoronitrile (PFN) and that of CO_2, O_2 and perfluoroketon (PFK) [11–13]. Although strong candidates are existed, there are still unclear points about current interruption and arc quenching.

Arc quenching media made of polymer are used in low voltage circuit breakers. Figure 1.1 depicts schematic cross section of a low voltage circuit breaker on current interruption.
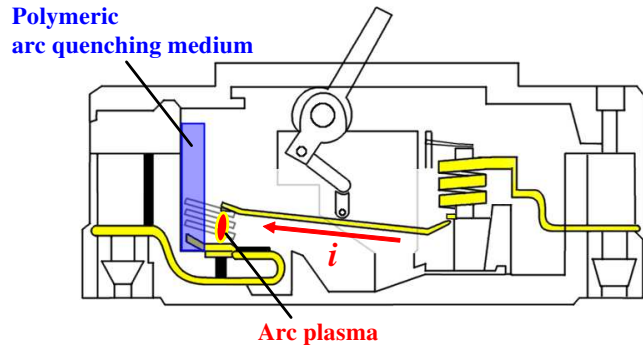
Fig. 1.1: Schematic cross section of a low voltage circuit breaker.
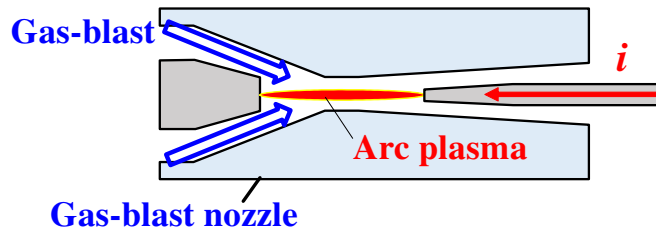
Fig. 1.2: Schematic cross section of a gas circuit breaker.

Electric path is coloured yellow and during the current interruption, electrodes are opened state but an arc plasma is ignited between the electrodes to conduct current. Some low voltage circuit breakers have a polymeric arc quenching medium near the arcing space. This arrangement causes the arc to contact the quenching medium, which causes a fierce ablation of the quenching medium. Ablation of the quenching medium involves strong gas flow that can quench the arc. In this way, solid polymeric arc quenching media work for current interruption. On the other hands, For a high voltage circuit breaker, gas is often used for arc quenching. Figure 1.2 illustrates a schematic cross section of a gas circuit breaker on current interruption. Two pieces of opposing blocks are electrodes and an arc plasma is ignited between the electrodes. The electrodes are surrounded by a gas-blast nozzle. The gas-blast nozzle concentrates the gas flow to the cramped space, called nozzle throat. The arc is quenched effectively by a strong gas flow made by the nozzle throat. In this thesis, the author investigated arc quenching media in solid phase and gas phase with experiments and numerical approaches.

1.2 Objective of this thesis

Arc quenching is an essential technique for current interruption because electric conductivity of arc plasma strongly depends on temperature of the arc path [14–16]. Therefore, arc quenching media is one of the most important parts in circuit breakers, especially for high-voltage circuit breakers. The method of arc quenching has continued to be utilized for tens of year to date.

The main objective of this thesis is fundamental investigation of arc quenching potential or arc quenching performance of various media, including solid and gas media. This objective leads to proposal of a new method or new media for arc quenching. To achieve the objective, the author focused on solid polymer materials and various gases such as SF_6 and CO_2 in this work. In this work, the following issues are discussed.

1. Causes of occurrence of the phenomena of small particles ejection from the surface of a polymer material irradiated by a thermal plasma ("spallation" phenomena).

2. Efficacy of "spallation" phenomena occurred from polyamide materials.

3. Observation and measurement of arc decaying processes in various gas flow.

4. Current interruption ability of various gases.

5. Observation and measurement of arc re-ignition processes in various gas flow.

The first and second aspects were done to consider possibility in application of spallation phenomena to arc quenching. The the third and fourth aspects are for evaluation of fundamental arc quenching ability of various gases. The final aspect was done to understand the arc behaviour in cases of current interruption failure.

1.3 Composition of the thesis

This thesis is composed from following chapters. In the first chapter, which is already described. In the second chapter, a special phenomenon which occurs only from polyamide materials is focused on. The author discovered that small particles were ejected from a surface of a polyamide specimen when it was irradiated by a thermal plasma and named

the phenomenon as "spallation" phenomenon. Furthermore, it was found that spallation phenomenon can be promoted by water absorption into the polyamide specimen before irradiation. The author further examined a relationship between spallation occurrence and composition of plasma irradiating the water absorbed polyamide specimen. As results, inclusion of O_2 into the thermal plasma strongly enhanced occurrence of spallation from the specimen. In addition, the author estimated cooling effects of spallation particles injected into a volume of hot air. Energy equation using enthalpy was solved and the author obtained the results that 10 small particles with radius of 100 μm have 3000 K of cooling effects on 10 cc of air from initial temperature of 10 kK.

In the third chapter, fundamental arc quenching characteristics of gas media were investigated. Using the arc device, SF_6, CO_2, O_2, N_2, air and Ar-blast arcs were ignited in a gas-blast nozzle and kept in direct current of 50 A. After that, the arc current and voltage were intentionally dropped to 0 A and 0 V to make a free recovery condition. This is achieved by switching on a power semiconductor, IGBT parallel connected to the arcing electrodes. In this situation, the gas-blast arc was quenched by the blast gas without energy input. The author evaluated arc quenching characteristics by the arc voltage in steady state, the arc behaviour in steady state and decaying phase, and electron density measurement using laser Thomson scattering (LTS) method. In addition, the author imitated transient recovery voltage by switching the IGBT off with a specified delay time t_d from initiation of the arc decaying. This voltage intentionally applied to the decaying arc is called "quasi-TRV". The prospective peak of the quasi-TRV is 1.2 kV and rise rate (RRRV) is 1.7 kV/μs. The decaying arc may re-ignite by application of quasi-TRV. Statistical results about re-ignition indicated SF_6 gas can prevent arc re-ignition in 30 μs from the start of the arc decaying. CO_2 quenched the arc to withstand the quasi-TRV in 130 μs. The results of electron density measurements by LTS method indicated decay rates of electron density in SF_6 and CO_2 arcs at the nozzle throat is near value.

In the fourth chapter re-ignition processes of gas-blast arcs were studied using the voltage application to decaying arcs. Various gas-blast arcs were intentionally re-ignited by quasi-TRV application for investigation of dielectric recovery properties. Blast gases were SF_6, CO_2, O_2, N_2, air and Ar. In addition to dielectric recovery properties, behaviour of the arcs were observed using a high speed video camera. A sequence of electron density from

decaying to re-ignition of the arc was also obtained and compared tendency of the blast gas. Results showed that dielectric recovery of SF_6-blast arc is the fastest in the tested gases. It was also found that every gas has a inflection point in the dielectric recovery curve. For example, SF_6-blast arcs rapidly recovered from 20 μs after initiation of the arc decaying. The inflection point of CO_2 was 80 μs. From the high speed video camera observation result, SF_6 arc lost its radiation intensity rapidly compared to other gas-blast arcs and regain the radiation intensity soon after the re-ignition. Radiation from CO_2 arcs decreased in a moderate pace and increased with moderate speed after the re-ignition. The results of the electron density measurement was rather complex but the results obtained in this work is precisely measured data of the sequence of electron density at the nozzle throat from the arc decaying to the arc re-ignition. In this respect, the author obtained valuable data for consideration of arc re-ignition process. The final chapter concludes this thesis.

References

[1] Han L, Chen W, Zhuang B and Ahen H 2017 A Review on Development Practice of Smart Grid Technology in China *IOP Conf. Ser.: Mater. Sci. Eng.* **199** 012062

[2] Ghenai C and Bettay M 2017 Optimized design and control of an off grid solar PV/hydrogen fuel cell power system for green buildings *IOP Conf. Ser.: Earth Environ. Sci.* **93** 012073

[3] Fei Y, Yi W, Mingzhe R, Hao S, Murphy A B, Zhigang R and Chunping N 2013 Low-voltage circuit breaker arcs–simulation and measurements *J. Phys. D: Appl. Phys.* **46** 273001 (19pp)

[4] Xuawei X, Jianyun C and Xudong S 2017 A No-Arc DC Circuit Breaker Based on Zero-Current Interruption *IOP Conf. Ser.: Mater. Sci. Eng.* **199** 012079

[5] Gleizes A, Razafinimanana M and Vacquie S 1983 Transport coefficients in arc plasma of SF_6-N_2 mixtures *J. AppL Phys.* **54** pp.3777-3787

[6] Tanaka Y, Yamachi N, Matsumoto S, Kaneko S, Okabe S and Shibuya M 2008 Thermodynamic and transport properties of CO_2, CO_2-O_2, and CO_2-H_2 mixtures at temperatures of 300-30000 K and pressures of 0.1-10 MPa *Electr. Eng. Japan* **163** 18-29

[7] Cressault Y, Connord V, Hingana H, Teulet P and Gleizes A 2011 Transport properties of CF_3I thermal plasmas mixed with CO_2, air or N_2 as an alternative to SF_6 plasmas in high-voltage circuit breakers *J. Phys. D: Appl. Phys.* **44** 495202 (22pp)

[8] Wang W, Rong M, Wu Y and Yan J D 2014 Fundamental properties of high-temperature SF_6 mixed with CO2 as a replacement for SF_6 in high-voltage circuit breakers *J. Phys. D: Appl. Phys.* **47** 255201 (16pp)

[9] Yang A, Liu Y, Sun B, Wang X, Cressault Y, Zhong L, Rong M, Wu Y and Niu C 2015 Thermodynamic properties and transport coefficients of high-temperature CO_2 thermal plasmas mixed with C_2F_4 *J. Phys. D: Appl. Phys.* **48** 495202 (25pp)

[10] Sun Hao, Rong M, Wu Y, Chen Z, Yang F, Murphy A B and Zhang H 2015 Investigation on critical breakdown electric field of hot carbon dioxide for gas circuit breaker applications *J. Phys. D: Appl. Phys.* **48** 055201 (16pp)

[11] Kieffel Y, Biquez F and Ponchon P 2015 Alternative gas to SF_6 for use in high voltage switchgears: g^3 *23*[rd] *International Conference on Electricity Distribution* Paper0230

[12] Hyrenbach M, Hintzen T, Müller and Owens J 2015 Alternative gas insulation in medium-voltage switchgear *Proc. 23*[rd] *Int. Conf. on Electricity Distribution*, paper0587

[13] Yi W, Chunlin W, Hao S, Mingzhe R, Murphy A B, Tianwei L, Jianying Z, Zhexin C, Fei Y, Chunpin N 2017 Evaluation of SF_6-alternative gas C5-PFK based on arc extinguishing performance and electric strength *J. Phys. D: Appl. Phys.* **50** 385202 (15pp)

[14] Tanaka Y, Paul C K and Sakuta T 2000 Thermodynamic and Transport Properties of N_2/O_2 Mixtures at Different Admixture Ratios *Electr. Eng. Japan* **120-B** No.1 pp.24-30

[15] Tanaka Y and Sakuta T Investigation on plasma-quenching efficiency of various gases using the inductively coupled thermal plasma technique: effect of various gas injection on Ar thermal ICP *J. Phys. D: Appl. Phys.* **35** 2149

[16] Cressault Y, Gleizes A and Riquel G 2012 Properties of air-aluminum thermal plasmas *J. Phys. D: Appl. Phys.* **45** 265202 (12pp)

Chapter 2

Spallation occurrence from polyamide materials irradiated by thermal plasma with water absorption

2.1 Introduction

Direct current (dc) power transmission and distribution systems are receiving attention worldwide because the electric devices of today work with inverter power supplies which convert commercially transmitted ac current to dc current and then to high-frequency current. Direct current is also used for electric vehicles (EV), power conditioners, and electronic devices. In addition, recent progress of 'smart grids' is gradually increasing the electric power to be handled. The dc system described above requires high-performance dc circuit breakers for severe accidents. For the reasons described above, low voltage circuit breakers must be developed to improve arc-quenching and current interruption performance. To enhance the arc-quenching capability of circuit breakers, polymer ablation has been widely adopted. During high-current interruption in a circuit breaker, an arc plasma is formed between the electrodes. The arc plasma contacts the polymer material, which involves strong polymer ablation. The polymer ablation engenders a pressure rise and strong gas flow, resulting in arc cooling. To understand these phenomena, it is necessary to investigate details of the interactions between the polymer and arc plasma / thermal plasma because the interactions are extremely complicated, including thermal decomposition and mixing of vapour and decomposition [1 – 24]

To study interactions between polymer materials and arc plasma / thermal plasma, the

author used inductively coupled thermal plasma (ICTP) irradiation technique to polymer material [12, 25]. The ICTP is irradiated to polymer bulk for this fundamental study of the above interaction instead of arc plasma. In ICTP irradiation experiments, the author has pointed out that polyamide materials such as polyamide-6 (PA6) and polyamide-66 (PA66) occasionally eject not only ablation gases but also micro-size particles during ICTP irradiation. This particle ejection phenomenon has been named 'spallation' generally in the aerospace field. The author expects that such spallation particles can be adopted to enhance the arc quenching ability of a circuit breaker. Spallation particles might penetrate the arc discharge core deeply because of the mass inertia. Subsequently, they will be ablated there to reduce the arc temperature [26, 27].

As described in this section, first of all, experimentally obtained results of Ar ICTP irradiation tests are presented for polymer materials of seven kinds including PA6 and PA66. Experiment results indicate that the Ar ICTP irradiation involves the occurrence of spallation phenomena only from PA6 and PA66 specimens. Considering the characteristics of polyamide materials, the author inferred that hydrophilia of polyamide might be related to occurrence of spallation. To confirm the relation between hydrophilia of polyamide and spallation occurrence, PA6 and PA66 specimens of two kinds, with and without water absorption, were prepared. Then they were irradiated by Ar ICTP. Results demonstrated that PA6 and PA66 with water absorption ejected much greater quantities of spallation particles than those of without water absorption. In addition, results show that N_2 or O_2 (contained in air) inclusion to the Ar thermal plasma enhances the occurrence of spallation from PA66 with water absorption. Moreover, the author estimated the cooling effects of spallation particles in high-temperature air for arc quenching. This method of estimation indicated that inclusion of 10 and more PA66 particles to high-temperature air might cause 3000 K drop in air temperature, thereby indicating effective arc quenching.

2.2   Investigation of interactions between thermal plasma / arc plasma and polymers

The author used inductively coupled thermal plasma (ICTP) instead of arc plasma between electrodes to investigate interactions between thermal plasma / arc plasma and poly-

mers. This decision can be attributed to the author's recognition of the following facts: (i) Both the ICTP and the arc plasma between electrodes have extremely high collision frequency among particles, which gives a high heavy-particle temperature approaching the electron temperature. (ii) Their behavior can be described approximately by macroscopic properties such as thermodynamic and transport properties determined by the temperature and the pressure. (iii) Thermal ionization occurs in both an arc and an ICTP to sustain itself with a certain level of electrical conductivity. For these three reasons, both the ICTP and the arc plasma can be categorized as 'thermal plasmas'.

In addition, the ICTP has the following benefits for fundamental investigation: (a) Clean thermal plasma can be produced with no impurities because ICTP needs no electrodes. This fact enables the author to investigate fundamental interactions between thermal plasma and polymers. The conventional arcs require electrodes that ablate and contaminate the arc medium, which makes the arc phenomena more complex. (b) The ICTP shows better repeatability in its production, than one-shot circuit-breaker arc testing. (c) Only the polymer species change enables the author to compare the effects of polymer varieties that are used.

2.3 Thermal plasma irradiation test of various polymer materials

2.3.1 Polymer materials tested

The following polymer materials were chosen for testing. Polytetrafluoroethylene (PTFE) polyethylene (PE) polyoxymethylene (POM) polymethylmethacrylate (PMMA) polyamide-6 (PA6) polyamide-66 (PA66) polyformaldehyde (PF).

Table 2.1 presents a list of the polymer materials tested for Ar-ICTP irradiation. This table presents groups of heat characteristics whether thermoplastic or thermosetting, and the decomposition temperature of each polymer. The decomposition temperatures presented here are those which were actually measured using thermogravimetry and differential thermal analysis (TG-DTA) and differential scanning calorimetry (DSC). The PTFE has the highest decomposition temperature among the seven kinds of polymer materials. When the

Table 2.1: Tested polymer materials for the first experiment.

Material	Group	Decomposition temperature [K]
Poly-Tetra-Fluoro-Ethylene (PTFE)	Thermoplastic	809
Poly-Ethylene (PE)	Thermoplastic	734
Poly-Oxy Methylene (POM)	Thermoplastic	605
Poly-Methyl-Methacrylate (PMMA)	Thermoplastic	618
Poly-Amide-6 (PA6)	Thermoplastic	718
Poly-Amide-66 (PA66)	Thermoplastic	669
Phenol-Formaldehyde (PF)	Thermosetting	-

temperature of a polymer material exceeds the decomposition temperature of the polymer, then the polymer is decomposed to eject ablation vapour containing atoms, molecules or ions from the polymer. Such heat decomposition of the polymer can take thermal energy from the heated arc plasma. In the ICTP irradiation test, every polymer is expected to eject ablation vapour.

2.3.2   Experimental setup and experimental conditions

Figure 2.1 depicts the ICTP system used in the present experiment. The ICTP torch comprises two coaxial water-cooled quartz tubes. Each 345-mm-long quartz tube has different diameter, the inner quartz tube has 70 mmϕ inner diameter. Argon gas is supplied from the top of the plasma torch to the interior of the inner quartz tube as the sheath gas. Different gases, such as N_2 and O_2 can be supplied if ones study the effects of chemical reaction of reactive species on interaction between thermal plasma and polymers. An eight-turn induction coil is located around the torch to generate electromagnetic fields. Then inductively coupled thermal plasma is created inside the torch. The generated thermal plasma
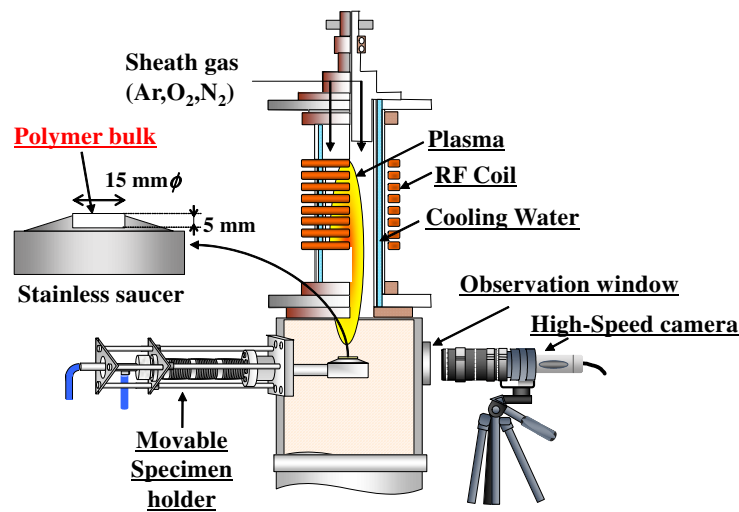
Fig. 2.1: ICTP torch and chamber.

expands downward below the inlet of the chamber by gas flow. A polymer specimen is embedded in a stainless saucer mounted on a movable specimen holder cooled by flowing water. The shape of polymer specimen used in this experiment is shown in figure 2.2, which has 15-mm-diameter and 5 mm thickness. The movable specimen holder can convey the polymer specimen to the position under the thermal plasma flow after the experimental conditions, such as input power, gas flow rate and pressure, are fixed. Subsequently the thermal plasma is irradiated directly to the polymer specimen.

In this experiment, the input power to the ICTP was set to 8.5 kW and the Ar sheath gas flow rate was 30 slpm. The Ar gas was used because Ar ICTP is easily established. Moreover, it is chemically stable gas so ones can investigate thermal interaction between polymer and thermal plasma. The pressure in the chamber was regulated to around 1.0 atm. During thermal plasma irradiation, the polymer specimen surface was observed using a high-speed video camera. The frame rate of the high-speed video camera observation was set to 1000 frames per second.

2.3.3   Spallation occurrence by Ar-ICTP irradiation on PA6 and PA66

Figure 2.3 shows the high-speed video camera observation result of Ar-ICTP irradiation of PTFE, PE, POM, PMMA, PA6, PA66, and PF specimens. The thermal plasma is
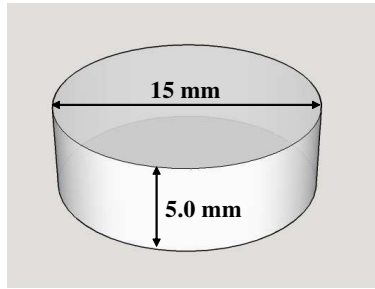
Fig. 2.2: Specimen shape for water absorption tests and thermal plasma irradiation experiments.

irradiated to the specimen from above in this figure. The thermal plasma irradiation to the polymer specimen causes strong ablation of the specimen. As presented in this figure, the radiation from the ablation vapour cloud is clearly visible over the specimen surface. The radiation from the ablated vapour results from the excited molecules and atoms in the ablated vapour irradiated by thermal plasma. The main colour of the radiation is blue, which can originate from C_2 Swan band system at wavelengths around 450–570 nm, as found in a previous work [28]. As each picture shows, all the polymers eject more or less ablation vapour. However, results also show that PA6 and PA66 eject not only ablation vapour but also particles above the ablation vapour. These ejected particles are called 'spallation particles'. A spallation particle can be a small piece of the polymer.

If the spallation phenomenon is applied to arc quenching, then spallation particles might penetrate the arc discharge core deeply because of the mass inertia. Then they will be ablated there to decrease the arc temperature effectively. Therefore, spallation particles can be used for effective arc quenching.

2.4   Influence of water absorption in PA6 and PA66 on the occurrence of spallation phenomena

2.4.1   Features of PA6 and PA66

As the preceding section explained, among polymer materials of several kinds, only PA6 and PA66 materials can eject spallation particles during thermal plasma irradiation. Here, some features of PA6 and PA66 are described for consideration of the essence of spallation
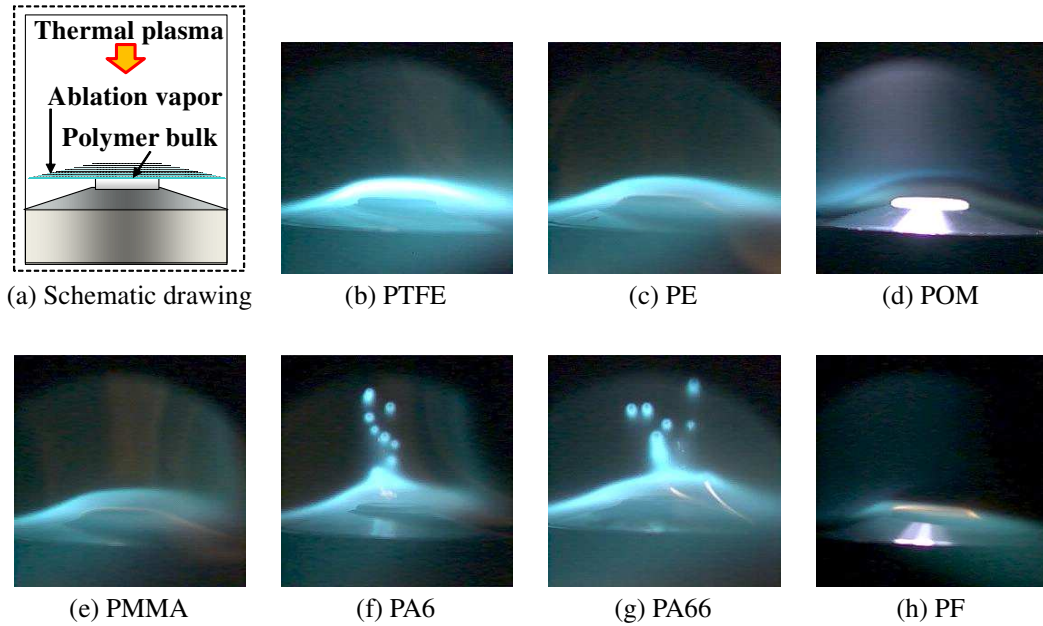
Fig. 2.3: Ar-ICTP irradiation on (b) PTFE, (c) PE, (d) POM, (e) PMMA, (f) PA66, (g) PA6, and (h) PF, (a) is a schematic image.

occurrence. Polymers PA6 and PA66 are classified as polyamide materials. Polyamide materials are widely used in various applications such as food wrap films, fiber products, some parts of automobiles as well as electrical insulation and ablation parts in low-voltage circuit breakers. Among polyamide materials, polyamide-6 (PA6) and polyamide-66 (PA66) are generally categorized as engineering plastics. Both have high mechanical strength and high chemical resistance. Figure 2.4 presents the structural formulas of PA6 and PA66. Actually, PA6 has the chemical formula of $(-C_6H_{11}ON-)_n$, whereas PA66 has $(-C_{12}H_{22}O_2N_2-)_n$. They have mutually similar mechanical, physical, and chemical characteristics. However, PA66 has slightly higher chemical resistance and mechanical strength than the PA6.

Polyamide materials including PA6 and PA66 have amide bonds (-CONH-) in their polymer structures. Polyamide molecules are therefore strongly bonded to each other through amide bonds. Figure 2.5 presents schematics showing hydrogen bonds in polyamide materials. Figure 2.5(a) depicts the normal state of polyamide structure. In the normal state, some amide groups have hydrogen bonds with other amide groups. The mechanical strength of polyamide originates from these amide bonds. In addition, amide bonds can have hydrogen bonds through $-C=O(\delta-)-$ with water (H_2O) because H_2O has an electric dipole. Figure 2.5(b) presents an example of the connection occurring with a H_2O molecule
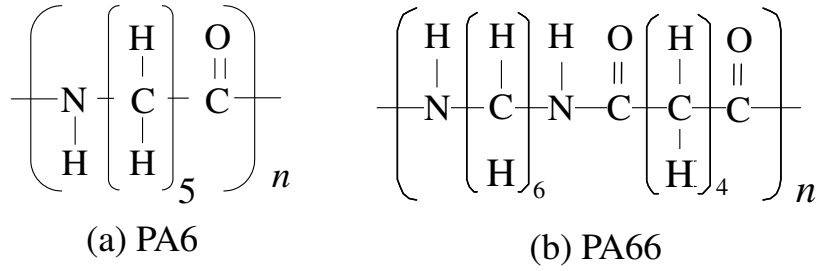
(a) PA6

(b) PA66

Fig. 2.4: Structural formulas of (a) PA6 and (b) PA66.

(a) Normal
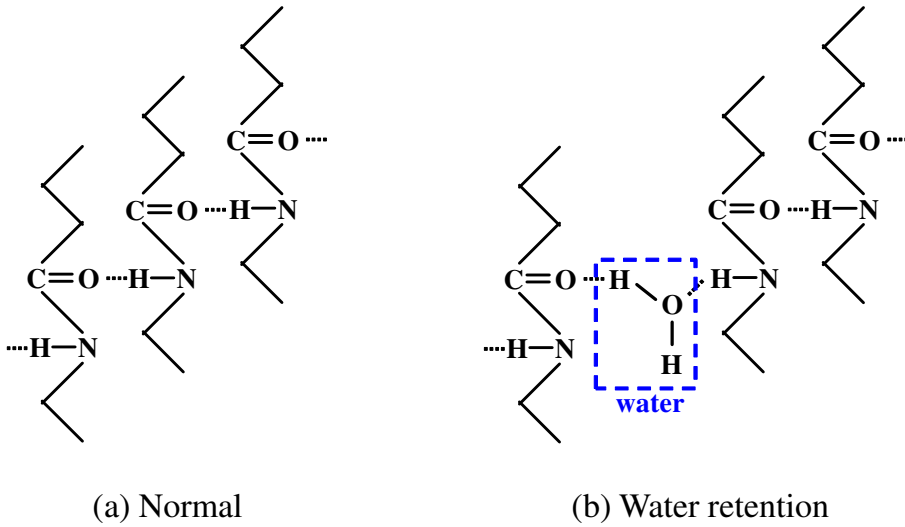
(b) Water retention

Fig. 2.5: Water retention image of polyamide: (a) normal state and (b) water molecule connected with amide bonds in polyamide which causes water retention of polyamide.

in polyamide. The hydrogen atom in amide group has a positive charge. It attracts oxygen atoms of water molecules electro-statically when there are water molecules. Similarly, the hydrogen atom in H_2O is electro-statically attracted by oxygen atoms of the amide group in polyamide. As a result, the polyamide material has a high hydrophilic property. The author inferred that this hydrophilia of polyamide material is related to the occurrence of spallation phenomena.

2.4.2   Water absorption test into PA6 and PA66

First, the author confirmed the water absorption ability of PA6 and PA66 specimens by soaking a polyamide specimen in water. The specimen with a shape shown in figure 2.2 is used for water absorption tests. It is also used in thermal plasma irradiation experiments as described in a later section. Other kinds of polymer material specimens such as PTFE,

PE, POM, and PMMA were also prepared with the same shape for comparison. The mass of a PA6 specimen was measured as 0.95 g. That of PA66 was 1.0 g. First, PA6 specimens were soaked in pure water for 3 hr at different temperatures: cool temperature (283 K), room temperature (295 K), and boiling temperature (373 K).

Figure 2.6 presents results of the water absorption ratio for PA6 for different temperatures of 283 K, 295 K, and 373 K. Here, the water absorption ratio was defined as shown below.

$$R_{\text{water}} = \frac{(M_{\text{after}} - M_{\text{before}})}{M_{\text{before}}} \times 100[\text{wt}\%] \tag{2.1}$$

Therein, M_{after} is the mass after 3 hr soaking; also M_{before} is the mass before soaking. The water absorption ratio of PA6 soaked in boiling water (373 K) was estimated as 4.6wt%, which is the highest value in these three conditions. Results show that the water absorption ratio of PA6 depends strongly on temperature. This might be true because the lattice distance of PA6 increases with temperature. Then more water is absorbed.

For comparison, figure 2.7 presents the water absorption ratio of the above polymers of six kinds in boiling water (373 K) for 3 hr. As this figure shows, PA6 has the highest water absorption ratio of 4.6wt%. The second highest ratio is that of PA66 as 2.6wt%. However, PTFE and PE materials have extremely lower water absorption ratios because these materials have no dipole in polymer molecules.

Figure 2.8 presents the water absorption ratio of PA6 and PA66 soaked in boiling water as a function of soaking time. After 40 hr soaking, the water absorption rate of PA6 is 10wt%; that of PA6 is 6.3wt%. Actually, PA6 seems to have greater water retention capacity than PA66 has. According to this figure, one can control water absorption ratio of PA6 and PA66 to some degree after soaking.

2.4.3   Experimental conditions for Ar-ICTP irradiation on water absorbed PA66 and PA6

The Ar ICTP irradiation test was conducted for polyamide specimens before and after water absorption. The same experimental setup and the shape of the specimen for ICTP irradiation were used, respectively, as those shown in figures 2.1 and 2.2. The input power to ICTP was set to 9.8 kW. The thermal plasma irradiation time duration was 20 s. The
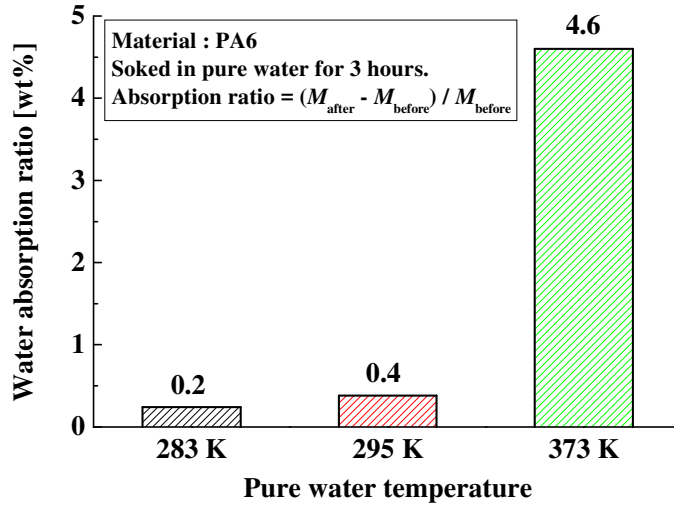
Fig. 2.6: Water absorption ratio of PA6 soaked in pure water at different temperatures for 3 hr.

chamber pressure was regulated at 1.0 atm. The author did high-speed video camera observations and ablation mass measurements. The frame rate of the high-speed video camera was set to 1000 fps.

The author prepared dry PA6 and PA66 specimens, which were placed in a desiccator with silica gel for dry specimens. In addition to these, PA6 and PA66 specimens having soaked in water at room temperature for 10 hr after 5 hr boiling were used for experimentation. This soaking involves the PA6 specimen with 6.8wt% water absorption and the PA66 specimen with 3.9wt% water absorption.

2.4.4   High-speed video camera observation of spallation occurrence from PA6 / PA66 irradiated by Ar ICTP

Figure 2.9 shows high-speed video images of PA6 and PA66 specimens irradiated by Ar ICTP. In each case, the ICTP is generated at input power of 9.8 kW and Ar sheath gas of 50 slpm. The thermal plasma is irradiated from the top side in these figures. The observation direction is perpendicular to the plasma flow direction. Radiation from Ar thermal plasmas is only slightly detectable because the radiation from Ar spectral line is lower than that from ablated vapour. Every panel (a)–(d) shown here is a superimposed image of over 100 images captured in 0.1 s, from 0.9 s after the beginning of irradiation up through 1.0 s.
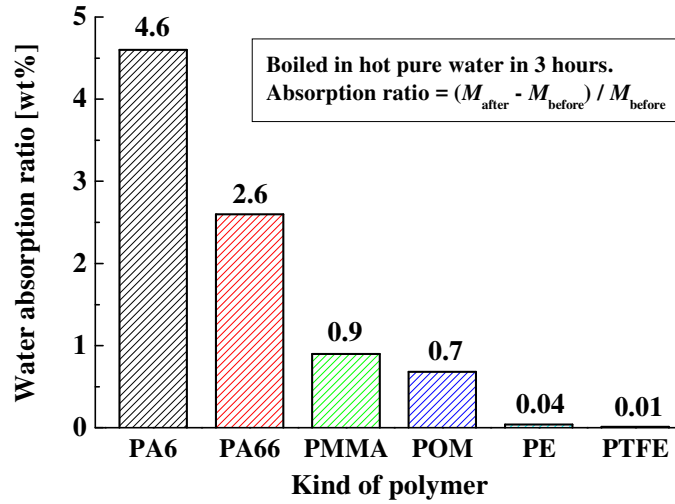
Fig. 2.7: Water absorption ratio of different polymers boiled in hot pure water for 3 hr.

Figure 2.9(a) shows the case of Ar ICTP irradiation on dry PA6 specimen. Light emission from ablation vapour is apparent around the specimen. The main colour of the light is blue, which originated by C_2 Swan system. Faint purple light is also apparent in some parts of the picture. The colour purple comes from the intensity of CN violet spectra at wavelengths around 350–400 nm. In this case of PA6 without water absorption, spallation phenomena only slightly occur.

Figure 2.9(b) depicts the case of Ar ICTP irradiation on PA6 with 6.8wt% water absorption. The image in figure 2.9(b) is clearly different from the previous picture of dry PA6 in figure 2.9(a). Small particles were ejected from the specimen surface They were ablated above the ablation vapour layer. These particles are spallation particles. This result demonstrates that water absorption promotes spallation particle ejection from the PA6 specimen. Ejected spallation particles are ablated in the irradiated thermal plasma. They emit blue light originating from C_2 molecular spectra during their flight. Therefore, spallation particles can penetrate deeply into high-temperature thermal plasma. Then they can be ablated to suppress the thermal plasma temperature. The number of spallation particles ejected high above the ablation gas layer reaches 24 from figure 2.9(b).

Figure 2.9(c) portrays the case of dry PA66. The ablated aspect of PA66 in this figure is similar to the case of dry PA6 shown in figure 2.9(a), although the purple colour strength of PA66 ablation vapour is slightly higher than that of PA6. In this case, no spallation
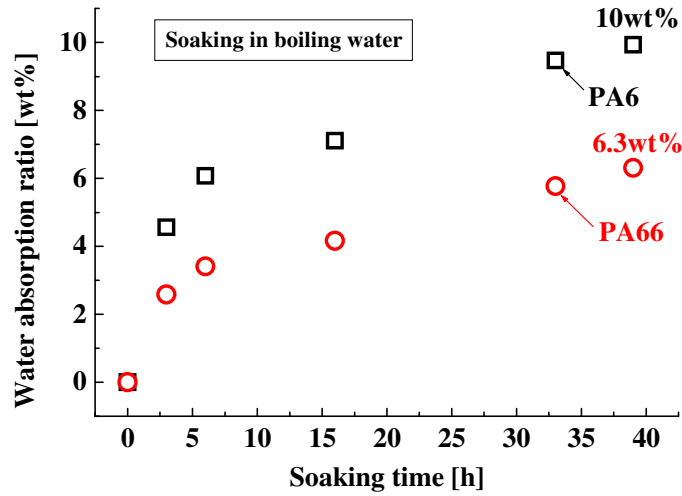
Fig. 2.8: Water absorption ratio of PA6 and PA66 versus soaking time.

particle was ejected from the dry PA66 specimen. Figure 2.9(d) depicts the result of PA66 with 3.9wt% water absorption. Although the water absorption ratio of PA66 in this figure differs from that of the PA6 specimen used in figure 2.9(b) (6.8wt%), spallation particles ejected from the specimen are clearly detectable. The spallation particles ejected high above the ablation gas layer were 17.

These high-speed video camera observation results above confirmed that spallation phenomena result from water absorption in the polyamide materials of PA6 and PA66. The mechanism of spallation occurrence has not been explained completely yet, but the author infers the following description.

1. The heat flux from thermal plasma plasticizes the surface of the polyamide bulk.

2. Water molecules are desorbed. Then they condense into droplets.

3. The water droplets are heated and evaporated to increase the internal pressure under the polymer surface.

4. When the internal pressure increases to withstand pressure of polyamide mechanically, the parts of polyamide are broken up. That effect causes particle ejection to thermal plasmas.

(a) Dry PA6   (b) Water PA6   (c) Dry PA66   (d) Water PA66
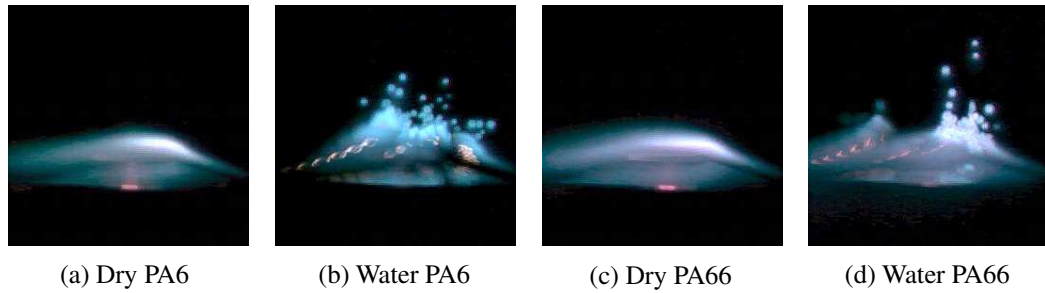
Fig. 2.9: Superimposed image of Ar ICTP irradiation on PA6 and PA66: (a) PA6 without water absorption, (b) PA6 with 6.8wt% water absorption, (c) PA66 without water absorption, (d) PA66 with 3.9wt% water absorption. The input power to the Ar ICTP is 9.8 kW.

2.4.5   Ablation mass of PA6 / PA66 irradiated by Ar ICTP for 20 s

Figure 2.10 presents the ablated mass of polyamide specimens that had been irradiated for 20 s by Ar ICTP. The ablation mass was estimated from the different measurements conducted before and after irradiation of Ar ICTP. The ablated mass of dry PA6 without water absorption is about 60–70 mg, which is approximately equal to that of dry PA66 without water absorption. However, both the water-absorbed PA6 specimen and water-absorbed PA66 specimen were ablated about 100 mg, which is about 1.5 times higher than that of dry PA6 and PA66 specimens. It is noteworthy that the mass of absorbed water is only several percent of the specimen mass. The facts presented above imply that water absorption to polyamide specimens increases the ablation mass. This increase in ablation mass by water absorption might result from the mass loss from spallation particle ejection.
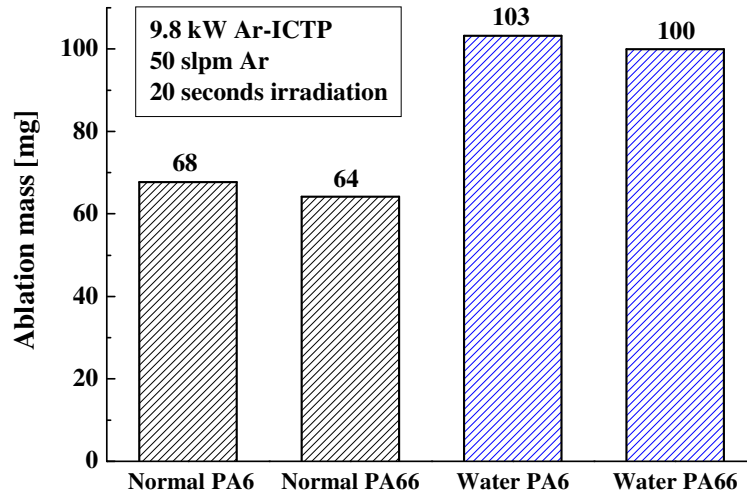
Fig. 2.10: Ablation mass of PA6 / PA66 irradiated by Ar ICTP for 20 s.

2.5   Ar + N_2/O_2 ICTP irradiation on PA66 with water absorption

2.5.1   Experimental conditions for Ar + N_2/O_2 ICTP irradiation on water absorbed PA66

This section presents an examination of the influence of chemical reactions in thermal plasmas irradiated to the PA66 specimen on the occurrence of spallation phenomena from water absorbed PA66. The PA66 specimens used in this work had 3wt% water absorption. Gases N_2 and O_2 and their mixture gas were supplied to Ar ICTP irradiated to the water absorbed PA66 specimen. These gases and gas mixtures were selected for use in this study because they are contents of air. In addition, the author has strived to study the influence of chemical reactions in air thermal plasma on the spallation occurrence, for use in arc quenching in a circuit breaker. In this work, six thermal plasma conditions were tested. The first one is the case of Ar ICTP irradiation, which is designated as *Cond. A = Condition A* in Table 2.2. The second one is N_2 inclusion case to Ar ICTP, designated as *Condition B*. The cases of N_2 and O_2 inclusion to Ar ICTP are *Cond. C^-*, *Cond. C* and *Cond. C^+*. The difference between C^-, C and C^+ is the admixture ratio of N_2/O_2. The last case is O_2 inclusion to Ar ICTP, designated as *Cond. D*.

For each of the six conditions, the heat flux from the thermal plasma to the specimen is

Table 2.2: Thermal plasma conditions for ICTP experiments

Gas condition	Ar [L/min]	N$_2$ [L/min]	O$_2$ [L/min]	Input power [kW]
100%Ar, 800 ºC (*Cond. A*)	30	0	0	8.5
97%Ar+3%N$_2$ (*Cond. B*)	50	1.5	0	12.8
97%Ar+2%N$_2$+1%O$_2$ (*Cond. C$^-$*)	50	1.0	0.5	12.6
97%Ar+1.5%N$_2$+1.5%O$_2$ (*Cond. C*)	50	0.75	0.75	12.4
97%Ar+1%N$_2$+2%O$_2$ (*Cond. C$^+$*)	50	0.5	1.0	12.2
97%Ar+3%O$_2$ (*Cond. D*)	50	0	1.5	10.3

expected to be almost identical because different heat flux might cause different interaction between the thermal plasma and polymer specimen. To ascertain the same heat flux condition for different gas mixtures of thermal plasma, the author set the different input power to different gas mixture thermal plasma in the following manner. Figure 2.11 depicts the surface temperature dependence of a TiO$_2$ specimen with a diameter of 15 mm and a thickness of 5 mm (instead of bulk polymer) on the input power to the thermal plasma given different gas conditions. The surface temperature of TiO$_2$ specimen on the water-cooled specimen holder was measured using a radiation thermometer. The TiO$_2$ specimen was used to estimate the heat flux from the surface temperature measurement because TiO$_2$ is extremely stable for thermal plasmas and chemical species in thermal plasmas. This figure shows that the surface temperature of the TiO$_2$ specimen increases concomitantly with increasing input power to the thermal plasma, and that it depends markedly on the gas mixture condition. Using this figure, the input power for the same heat flux condition for different gas mixtures was determined from the same surface temperature 800 ºC of a TiO$_2$ specimen. This method of inference provides the same heat flux conditions. In this case,
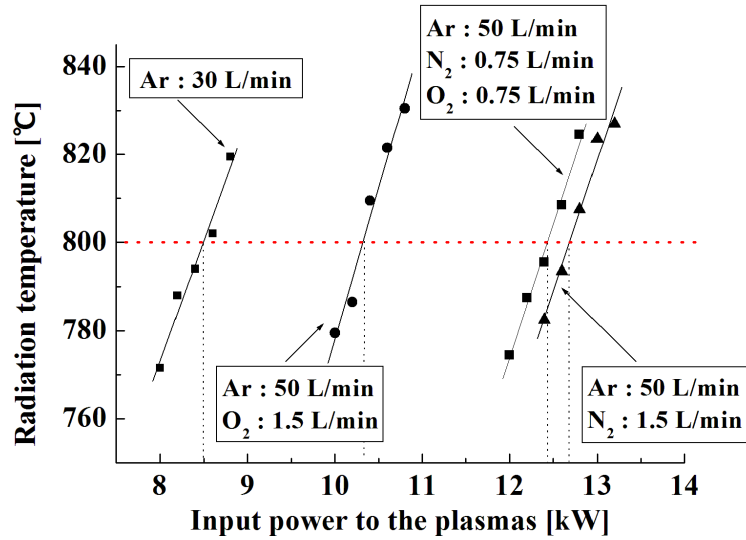
Fig. 2.11: Dependence of surface temperature of a TiO_2 specimen on input power.

the irradiated heat flux was estimated as around 500 kW/m^2 from the aid of a numerical simulation of induction thermal plasma with a specimen. The determined values of input power for different gas mixture conditions were added to Table 2.2.

In the irradiation experiment, high-speed video camera observations and ablation mass measurements were conducted. From the high-speed video camera observation, spallation particles were counted from the PA66 specimens.

2.5.2 High-speed video camera observation on spallation occurrence from PA66 with water absorption irradiated by Ar + N$_2$/O$_2$ ICTP

2.5.2.1 Ablation aspect and spallation occurrence

Figure 2.12 presents four images captured using a high-speed video camera during Ar + N$_2$/O$_2$ ICTP irradiation on water absorbed PA66. Irradiation of the Ar ICTP with different gas mixtures provides a quite different aspect of PA66 ablation. For 100%Ar ICTP irradiation, ablated vapour from PA66 emits white-bluish light, which is mainly attributed to strong spectral intensity from C$_2$ Swan system at wavelengths of 450–570 nm. The 97%Ar ICTP with 3%N$_2$ produces ablated vapour with similar colour but also

(a) Ar   (b) Ar+N$_2$ (c) Ar+N$_2$+O$_2$ (d) Ar+O$_2$
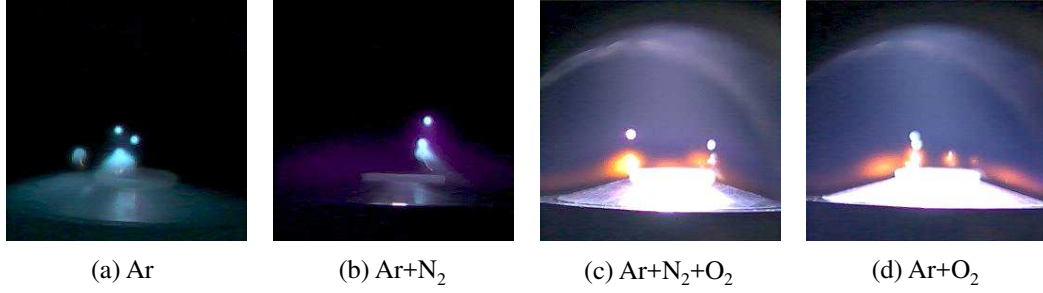
Fig. 2.12: Images of Ar+N$_2$/O$_2$-ICTP irradiation on water absorbed PA66 captured using a high-speed video camera, (a) 100%Ar, *Condition A* in Table 2.2, (b) 97%Ar+3%N$_2$, *Condition B*, (c) 97%Ar+1.5%N$_2$+1.5%O$_2$, *Condition C*, (d) 97%Ar+3%O$_2$, *Condition D*.

with purple around the PA66 surface. The colour purple comes from the high intensity of CN violet spectra at wavelengths of 350–400 nm. Inclusion of O$_2$ in the Ar ICTP involves orange colour in ablated vapour, which might arise from the continuous spectra by black-body radiation according to spectroscopic measurements [28]. This seems attributable to the combustion reaction of graphite particles in ablated vapour. In every case, the PA66 specimens eject spallation particles.

2.5.2.2   Influence of N$_2$ or O$_2$ inclusion on the number of spallation occurrence

Figure 2.13 presents four images produced by accumulation of 100 consecutive video images from 0.9 s to 1.0 s after ICTP irradiation in different conditions. As the figure shows, both N$_2$ and O$_2$ can promote spallation occurrence. Especially, inclusion of N$_2$ and O$_2$ seems to influence the ablation and spallation occurrence. Using sequence images taken by the high-speed video camera, the spallation particles were counted. Only the particles jumping up to the top of the ablation vapour layer were counted.

Figure 2.14 shows the instantaneous and cumulative numbers of spallation particles versus time from the beginning of ICTP irradiation. Each panel corresponds to the results counted from each panel shown in figures 2.12 and 2.13. The left vertical axis shows the instantaneous number of spallation particles, which is indicated by black bars. The right vertical axis shows the cumulative number of spallation particles, which is presented by curves. The 'instantaneous number' treated here is the number of spallation particles ejected at each time. In the case of 100%Ar, the first spallation particle was ejected at 300 ms after the beginning of ICTP irradiation. Spallation particles were ejected thereafter.

(a) Ar   (b) Ar+N$_2$ (c) Ar+N$_2$+O$_2$ (d) Ar+O$_2$
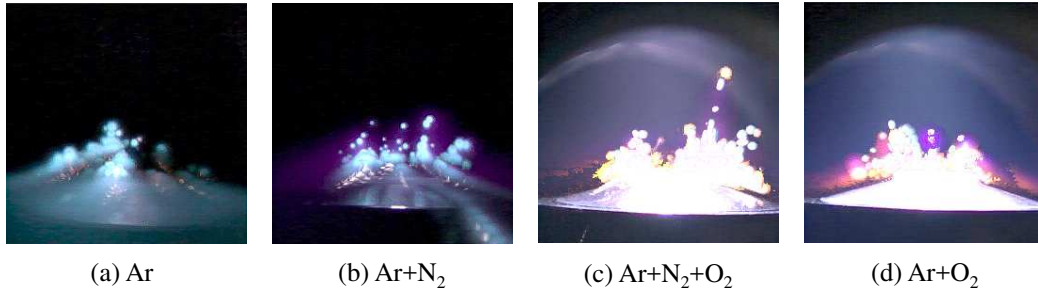
Fig. 2.13: Superimposed image of Ar+N$_2$/O$_2$-ICTP irradiation on water absorbed PA66, (a) 100%Ar, *Condition A* in Table 2.2, (b) 97%Ar+3%N$_2$, *Condition B*, (c) 97%Ar+1.5%N$_2$+1.5%O$_2$, *Condition C*, (d) 97%Ar+3%O$_2$, *Condition D*.

During 1000 ms 100%Ar ICTP irradiation, 75 particles were ejected in all. For 97%Ar + 3%N$_2$, the first ejected spallation particle was detected at 300 ms; 83 particles were ejected in 1000 ms. The 97%Ar + 1.5%N$_2$ + 1.5%O$_2$ ICTP irradiation involves the first ejection of a spallation particle at 300 ms. It has 113 particles ejection in all. Similarly, the 97%Ar + 3%O$_2$ ICTP irradiation causes the first spallation particle ejection at 220 ms; actually, 116 particles were ejected. These results demonstrate that inclusion of O$_2$ promotes spallation occurrence.

The total cumulative quantities of spallation particles ejected in 1.0 s for each ICTP condition are presented in figure 2.15. Each condition has three data. The average of these three experiments is shown there. The figure shows results of six conditions for comparison, including extra conditions *Cond. C$^-$* and *Cond. C$^+$*. One might recall that *Cond. A* is the case of 100%Ar, *Cond. B* is for N$_2$ inclusion, the three series of *Cond. C, C$^+$, C$^-$* are the cases of both N$_2$ and O$_2$ inclusion with change of the mixture ratio. Also, *Cond. D* is the case of O$_2$ inclusion. As this figure shows, pure Ar ICTP engendered 62 spallation particles, which is the lowest value among the six cases. With N$_2$ gas inclusion to Ar ICTP, the number of spallation particles increased to 74. Inclusion of both N$_2$ and O$_2$ mixture further increases the number of spallation particles detected. In the N$_2$ and O$_2$ mixture cases, a higher O$_2$ inclusion ratio tends to enhance the occurrence of spallation. As the O$_2$ mixture ratio rises, the number of spallation particles increases to 120. Only O$_2$ inclusion maintains a high value of the spallation occurrence over 100. This result implies the importance of chemical reactions with oxygen on the polymer surface for spallation occurrence.
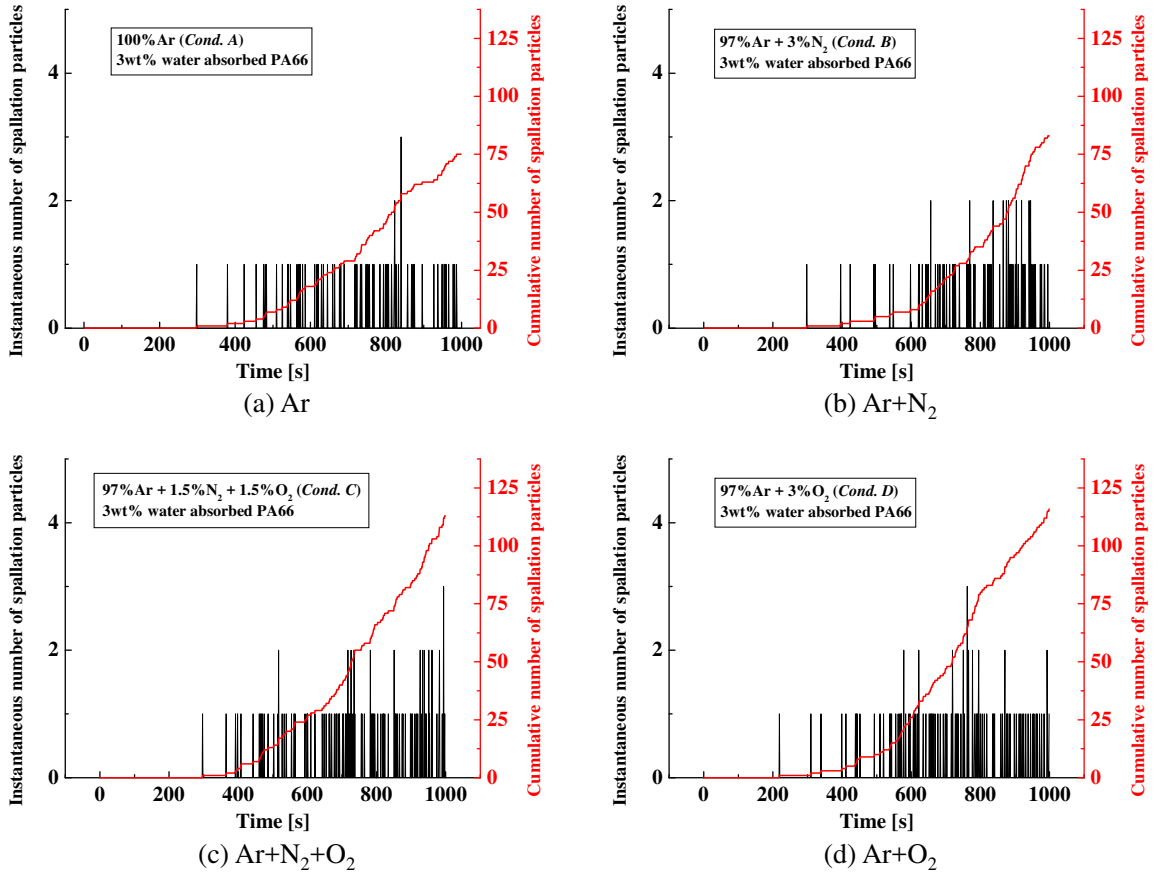
Fig. 2.14: Instantaneous and cumulative number of spallation particles versus time, (a) 100%Ar, *Condition A* in Table 2.2, (b) 97%Ar+3%N$_2$, *Condition B*, (c) 97%Ar+1.5%N$_2$+1.5%O$_2$, *Condition C*, (d) 97%Ar+3%O$_2$, *Condition D*.

2.5.2.3 Ablation of a spallation particle flying in thermal plasma

High-speed video camera observations revealed that the spallation particles flying in thermal plasmas was ablated during their flights. Figure 2.16 depicts the course of ablation of a spallation particle ejected during 97%Ar+1.5%N$_2$+1.5%O$_2$ ICTP irradiation. From this figure, a particle was ejected at the time 2.478 s after the beginning of ICTP irradiation. The particle reached the top of the jump at the time of 2.482 s, which corresponds to 4 ms after the beginning of the ejection. The particle was ablated during their falling down flight. The particle was lost by ablation to the time 2.485 s, corresponding to 7 ms after the ejection. As shown there, most spallation particles were ablated completely in less than 10 ms for all cases. Results show that the time required for ablation is sufficiently short
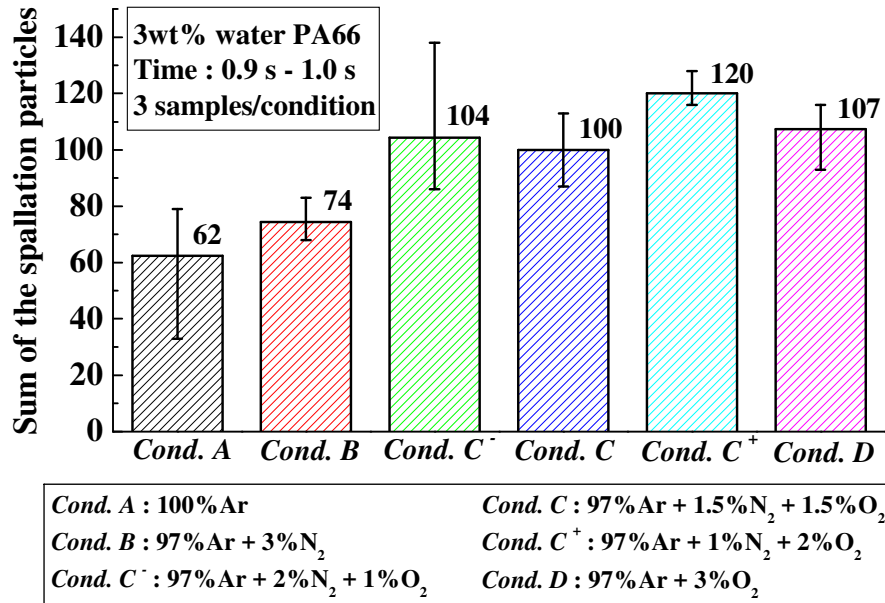
Fig. 2.15: Cumulative number of spallation particles ejected from 0.9 s to 1.0 s for each ICTP condition.

(a) 2.482 sec   (b) 2.483 sec   (c) 2.484 sec   (d) 2.485 sec
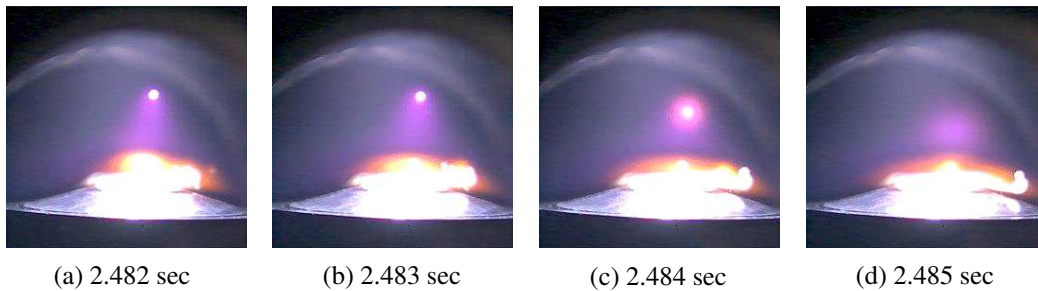
Fig. 2.16: Course of spallation particle ablation in $97\%Ar+1.5\%N_2+1.5\%O_2$ ICTP irradiation, (a) 2.482 sec, (b) 2.483 sec, (c) 2.484 sec, (d) 2.485 sec.

for arc quenching.

2.5.3   Ablation mass of 3wt% water absorbed PA66 irradiated by Ar + N_2/O_2 ICTP for 20 s.

The ablation mass of PA66 irradiated by Ar+N_2/O_2 ICTP for 20 s is described in this section. Figure 2.17 presents the ablation mass of the water absorbed PA66 specimen irradiated by Ar + N_2/O_2 ICTP for 20 s. As described previously, the ablation mass was calculated only as a mass difference between measurements taken before and after
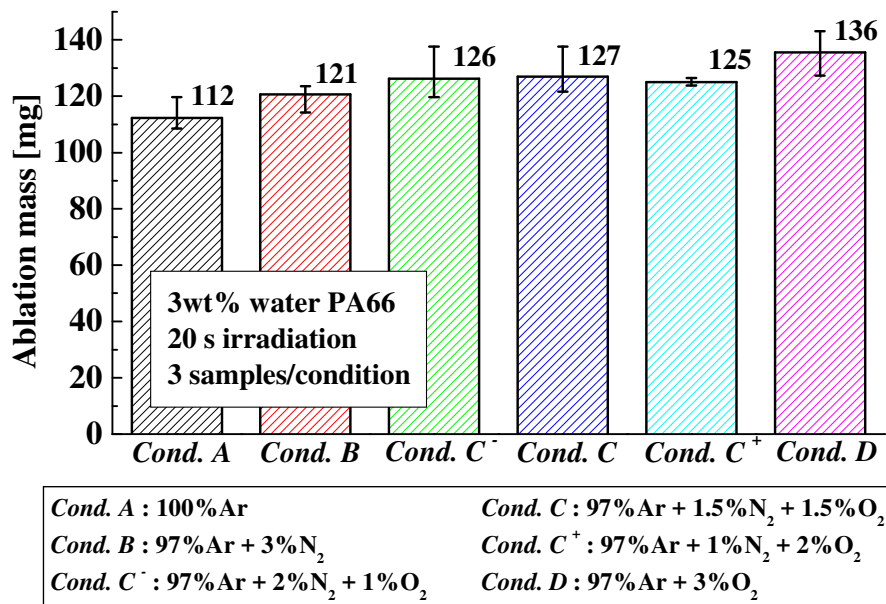
Fig. 2.17: Ablation mass of 3wt% water absorbed PA66 by 20 s irradiation for each ICTP condition.

ICTP irradiation. The bar in this figure shows the average value obtained from three experiments conducted under the same conditions. All experiments used water-absorbed PA66 specimens, which promotes spallation occurrence.

As this figure shows, the ablation mass is 100–150 mg for all conditions. Comparison of results shown in figures 2.15 and 2.17, shows that the ablation mass seems to depend roughly on the number of spallation particles. Increasing the sum of spallation particles elevates the ablation mass slightly, which implies that the spallation particles naturally contribute to the mass loss of the specimen.

The results of Ar + N$_2$/O$_2$ ICTP irradiation experiment confirmed that both N$_2$ and O$_2$ can promote the occurrence of spallation phenomena from water absorbed polyamide. Therefore, the author expects spallation phenomena to promote arc quenching effectively, because many low voltage circuit breakers such as mold case circuit breakers (MCCBs) work in open air.

2.6   Numerical estimation on cooling effects of spallation particles on thermal plasma.

2.6.1   Assumptions

This section presents a description of numerical estimation on the cooling effects of spallation particles on thermal plasmas. As described in the preceding sections, spallation particles are ejected from the PA66 surface to the thermal plasma, where they are ablated. That ablation can involve cooling of thermal plasma because of its latent heat for thermal decomposition and mixing of ablated vapour. The ablated vapour has some polyatomic molecular species. The mixture of these molecules has high effective specific heat capacity. These molecules can have internal energy instead of their kinetic energy. Also, they are decomposed.

Here, the author presumes a high-temperature air with a volume of 10 mL(=10×10^{-6} m^3) at a certain initial temperature T_{air} at atmospheric pressure 101,325 Pa. The volume of 10 mL is one typical volume of an arc in a small moulded case circuit breaker. It is assumed that in this high-temperature air PA66 sphere particles with a radius of 100 μm and a mass of 4.77 μg at 300 K would be injected. They would be evaporated completely because of high-temperature air involving a decrease in the air temperature, and then they would be PA66 vapour including polyatomic molecules of several kinds in high-temperature air at fixed atmospheric pressure. After mixing PA66 vapour with high-temperature air uniformly, the mixture would have to reach final temperature T_{f} and final volume V_{f} at fixed atmospheric pressure. The author calculated T_{f} for those conditions in the following subsections.

The initial temperature of the high-temperature air T_{air} was set to 5000, 7500, 10000, 12500, or 15000 K. The number of injected spallation particles is assumed to be 1, 5, 10, 30, or 50.

2.6.2 Thermodynamic properties for calculating cooling effects

2.6.2.1 Equilibrium composition, mass density and enthalpy of high-temperature air

First, the equilibrium composition of high-temperature air was calculated by minimization of the Gibb's free energy of the system [12, 25, 29, 30]. In this situation, the author assumed that composition of high-temperature air can be described as $78\%N_2 + 21\%O_2 + 1\%Ar$. Figure 2.18 presents the equilibrium composition of air at 101,325 Pa. The vertical axis shows the number density of the constituent species. The horizontal axis shows the gas temperature. At room temperature 300 K, the main components of air are N_2, O_2, and Ar. As the gas temperature rises, decomposition or association reactions of molecules can produce polyatomic molecules. At temperatures of 500 K to 1000 K, NO and N_2O molecules generated by decomposition and association are apparent. At temperatures from 1000 K to 10000 K, atomic species O and N appear. In addition, a small number density of O_3 and N_3 is apparent. At temperatures higher than 10000 K, most species become mono-atomic ions. The number density of electrons rises.

Using this equilibrium composition of air, one can calculate the mass density and the enthalpy of air at a certain temperature. Mass density of air ρ, which is the total mass of constituent species can be described as the following equation.

$$\rho = \sum_i m_i n_i \tag{2.2}$$

Therein, m_i stands for the mass of species i, and n_i denotes the number density of species i. Enthalpy h is calculable with the internal partition function Z_i^{int} and the standard enthalpy of formation $\Delta H_{\text{f}i}$:

$$h = \frac{1}{\rho} \sum_i \left(\frac{5}{2}kT + kT^2 \frac{\partial}{\partial T}(\ln Z_i^{\text{int}}) + \Delta H_{\text{f}i} \right) n_i \tag{2.3}$$

Figures 2.19 and 2.20 respectively show the temperature dependence of the mass density ρ and the enthalpy h of air. Because of the assumption that the initial volume of air is 10 mL($=10\times10^{-6}$ m^3), the author can obtain the mass of the air from the mass density. At a temperature of 5000 K, the mass of 10 mL air is 583 μg, 174 μg for 10000 K, and 78 μg for 15000 K. Results show that the mass of air decreases as the temperature rises at a

Fig. 2.18: Equilibrium composition of air at atmospheric pressure.

Table 2.3: Mass and thermal energy of 10 mL air at atmospheric pressure.

Temperature(K)	Mass(μg)	Enthalpy(J/g)	Thermal energy(J)
5000	583	102000	59.5
7500	267	327000	87.3
10000	174	478000	83.1
12500	122	683000	83.3
15000	78	1140000	88.9

fixed pressure. However, the enthalpy increases with a temperature rise. At a temperature 5000 K, the enthalpy of air is 10.2 kJ/g. It is 114 kJ/g for 15,000 K. By multiplying the initial mass and the enthalpy, one obtains the internal thermal energy of air within 10 mL volume. Table 2.3 expresses the temperature and the internal thermal energy of 10 mL air. At 5000 K, the internal thermal energy of 10 mL air is 59.5 J. For temperatures higher than 7500 K, the internal thermal energy reaches 80–90 J.

Fig. 2.19: Mass density of air versus the temperature.

2.6.2.2 Variation in composition, internal thermal energy of high-temperature air with inclusion of PA66 spallation particles

The author assumed PA66 sphere particles with a radius of 100 μm and a mass of 4.77 μg at 300 K. The PA66 particles would be included in high-temperature air. The particles were decomposed to produce PA66 vapour including polyatomic molecules, which are mixed with air. To consider the dominant species in air-PA66 vapour at a specified temperature, the equilibrium composition of air-PA66 vapour was calculated by minimization of the Gibb's free energy. The air-PA66 vapour admixture ratio depends on the initial temperature T_{air} and the number of PA66 spallation particles. For example, for air with an initial temperature of 5000 K and 1 spallation particle injection, the mass ratio of the air to PA66 is 583 : 4.77. The mass ratio is expected to take a value of 174 : 47.7 with 10 particles injection if the initial temperature of the air were 10,000 K.

Figure 2.21 depicts the equilibrium composition of air-PA66 vapour mixture generated by 1 particle injection into the air of the initial temperature 10000 K at atmospheric pressure. In this case, the mass ratio of air to PA66 is 174 : 4.77. The horizontal axis shows the gas temperature. The vertical axis shows the number density of the constituent species. The composition in figure 2.21 is greatly complicated compared to the composition presented in figure 2.18. This result derives from inclusion of C atoms and H atoms from PA66 vapour. A PA66 ($C_{12}H_{22}O_2N_2$) spallation particle can provide C and H atoms to produce
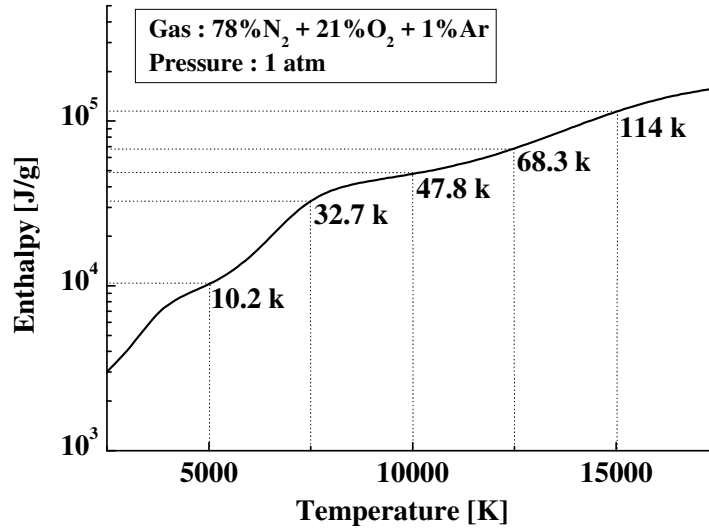
Fig. 2.20: Enthalpy of air versus temperature.

numerous and diverse species. In temperatures of 500 K to 1000 K, polyatomic or diatomic molecules are dominant. At temperatures from 1000 K to 10000 K, the mono-atom species number density of increases. A further increase in temperature to more than 10000 K makes the dominant species ions. In this way, PA66 particle inclusion to air causes considerable changes in the equilibrium composition of the air.

Using the calculated equilibrium compositions, the enthalpy of air-PA66 vapour mixtures is derived from equation (2.3). Figure 2.22 presents the temperature dependence of enthalpy of air-PA66 vapour mixtures with different admixture ratios of PA66. The admixture ratios here correspond to those calculated for 0, 1, 5, 10, 30, and 50 PA66 particles injected into 10 mL volume of air with an initial temperature of 10,000 K at atmospheric pressure, as described previously. As this figure shows, one or more particles injection rises the enthalpy of the vapour mixture at a fixed temperature. As increasing admixture ratio of PA66, which is shown with increasing the number of PA66 particles in this figure, the enthalpy of air-PA66 vapour is elevated at fixed temperatures. This elevation is attributed to the fact that air-PA66 vapour has complex polyatomic species carrying internal energy.
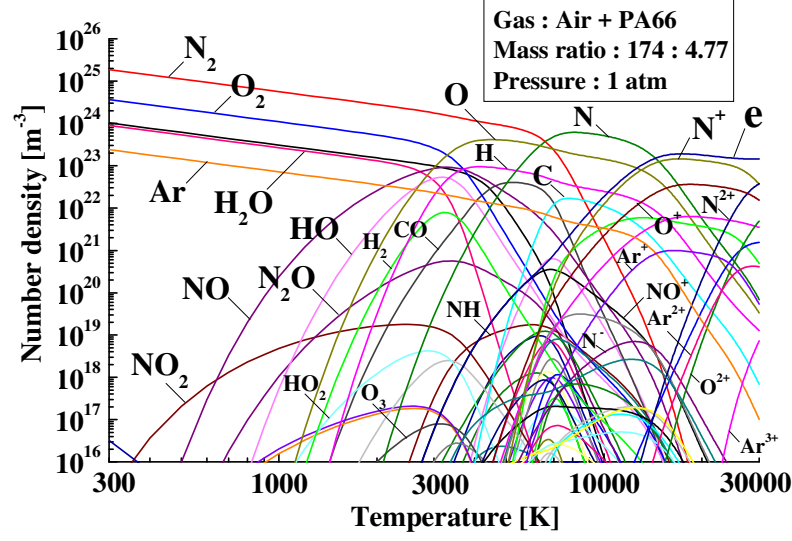
Fig. 2.21: Equilibrium composition of mixed vapour consisting of 10 ml air with initial temperature of 10,000 K and a PA66 spallation particle.

2.6.3 Calculation procedure for cooling effect of PA66 particles in high-temperature air

Thermal decomposition of PA66 particles and PA66 vapour mixing with dissociation reactions of polyatomic species lead to a temperature decrease of air from an initial temperature. After thermal decomposition and mixing, the mixture from 10 mL high-temperature air and PA66 particles has a final temperature T_f. This final temperature T_f is obtainable by solving the following energy conservation equation:

$$m_{\text{air}}h_{\text{air}}(T_{\text{air}}) = h_{\text{PA66-air}}(T_f) \times (m_{\text{air}} + m_{\text{PA66}}) + Q_e \times m_{\text{PA66}} \qquad (2.4)$$

where m_{air} signifies the mass of the high-temperature air, m_{PA66} denotes the mass of PA66 particles, $h_{\text{air}}(T_{\text{air}})$ represents the enthalpy of the air at the initial temperature T_{air}, and $h_{\text{PA66-air}}(T_f)$ stands for the enthalpy of the gas mixture of PA66-air at a final temperature T_f. Also, Q_e is the latent heat of PA66 from 300 K to the thermal decomposition temperature at atmospheric pressure. The value of Q_e is about 2.508 J per particle. Equation 2.4 can be expressed as

$$h_{\text{PA66-air}}(T_f) = \frac{m_{\text{air}}h_{\text{air}}(T_{\text{air}}) - Q_e \times m_{\text{PA66}}}{m_{\text{air}} + m_{\text{PA66}}} \qquad (2.5)$$
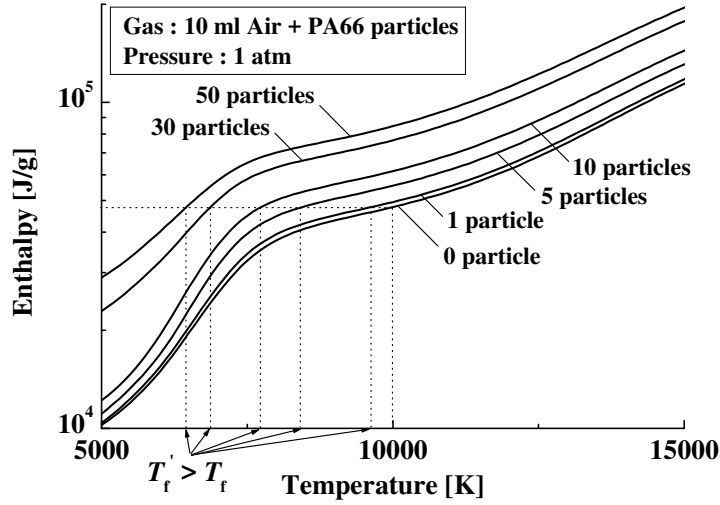
Fig. 2.22: Enthalpy of air-PA66 vapour mixture in cases of the initial temperature of air 10000 K and 0, 1, 5, 30, and 50 PA66 particle injection.

Ones can estimate the final temperature T_f satisfying the above equation (2.5). For $h_{\text{PA66}-\text{air}}$, we can use data in figure 2.22.

2.6.4   Calculation results of spallation particle cooling effects

Table 2.4 quantifies the final temperatures T_f for each initial temperature T_{air} and number of spallation particles. These are also presented in figure 2.23. For the cases of initial air temperature $T_{\text{air}} = 10,000$ K, a single PA66 particle can drop the temperature to 9300 K. This result demonstrates that one PA66 particle has a 700 K cooling effect. This cooling effect increases to more than 3000 K for 10 and more particles. This is a large cooling effect for arc quenching attributable solely to 10 PA66 particles. The primary factor underlying the cooling effects is the energy consumption from dissociation of molecules contained in PA66 ablation vapour. At high initial temperatures, where the mass of initial air is low because of its low density, the ablation of spallation particles results in greater cooling effects for air.

In the Ar + N_2/O_2 ICTP irradiation experiment described above, more than 30 spallation particles were ejected in 0.1 s. Considering the arc plasma ignited in a circuit breaker, the heat flux of the arc will be much higher than that of ICTPs. In addition, an arc in air contains plenty of N_2 and O_2, which can promote spallation occurrence. Tens of spallation

Table 2.4: Final temperature T_f for each number of spallation particles versus initial temperature of the hot air T_{air}.

Initial air temperature	Final temperature T_f for				
T_{air} (K)	1 particle (K)	5 ptcls	10 ptcls	30 ptcls	50 ptcls
5000	4900	4800	4700	4000	3400
7500	7400	7000	6700	5500	4000
10000	9300	7700	7000	5400	3900
12500	12000	9800	7500	5500	3900
15000	14400	12300	9800	5700	4000

particles are expected to drop thousands of Kelvin of the air arc temperature compared to no spallation particles if spallation phenomena are applied as a circuit breaker.

2.7   Summary of chapter 2

This section presents a study of the effect of water absorption to polyamide material on the occurrence of spallation phenomena: the particle ejection after breaking off from polymer materials irradiated by high heat flux. The experimentally obtained results demonstrated that polyamide specimens with water absorption ejected spallation particles, whereas polyamide specimens without water absorption ejected them only slightly. These results demonstrate that water absorption can promote spallation phenomena. Furthermore, N_2 and O_2 inclusions irradiated in thermal plasma enhance spallation phenomena.

Cooling effects of thermal plasmas by spallation PA66 particles were also estimated numerically. This estimation shows that 10 and more PA66 particles inclusion might decrease the air temperature by 3000 K. This temperature drop arises mainly from the energy consumption for dissociation reactions in polyatomic species in air-PA66 ablation vapour.

These results suggest that spallation phenomena can be useful to enhance arc quenching in circuit breakers work in air.
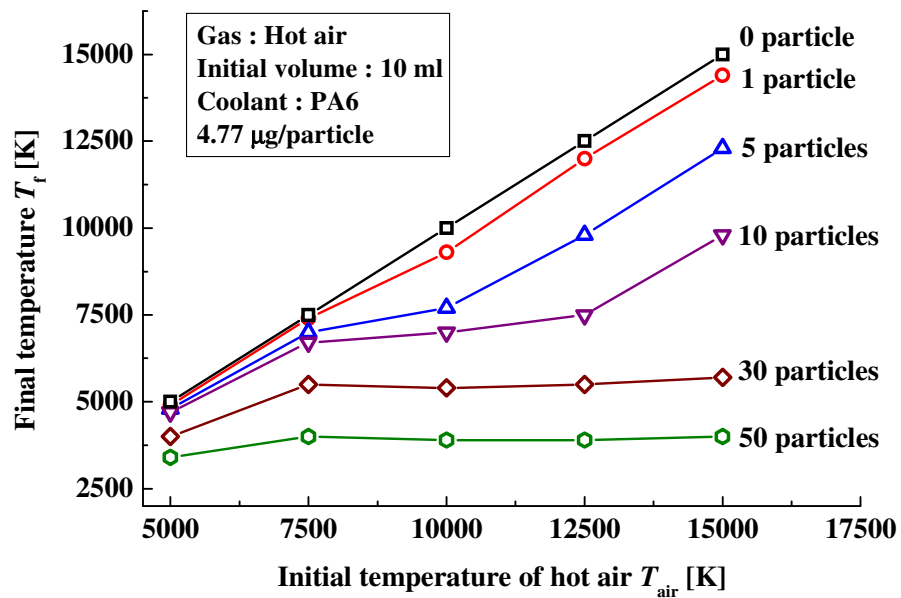
Fig. 2.23: Final temperature T_f of air-PA66 vapour versus initial air temperature T_{air} for each number of spallation particles.

References

[1] Andre P 1996 Composition and thermodynamic properties of ablated vapours of PMMA, PA6-6, PETP, POM and PE *J. Phys. D: Appl. Phys.* **29** 1963–72

[2] Andre P 1997 The influence of graphite on the composition and thermodynamic properties of plasma formed in ablated vapour of PMMA, PA6-6, PETP, POM and PE used in circuit-breakers *J. Phys. D: Appl. Phys.* **30** 475–93

[3] E Domejean, P Chévrier, C Fiévet and P Petit 1997 Arc-wall interaction modelling in a low-voltage circuit breaker *J. Phys. D: Appl. Phys.* **30** 2132–42

[4] C Fiévet, M Barrault, P Petit, P Chévrier, C Fleurier and V André 1997 Optical diagnostics and numerical modelling of arc re-strikes in low-voltage circuit breakers *J. Phys. D: Appl. Phys.* **30** 2991–9

[5] Uchii T, Shinkai T and Suzuki K 2002 Thermal interruption capability of carbon dioxide in a puffer-type circuit breaker utilizing polymer ablation *IEEE/PES Transmission and Distribution Conference and Exhibition 2002 (Yokohama, Japan)* **3** 1750–4

[6] Swierczynski B, Gonzalez J J, Teulet P, Freton P, and Gleizes A 2004 Advances in low-voltage circuit breaker modelling *J. Phys. D: Appl. Phys.* **37** 595–609

[7] Markutsya S, Rapeaux M and Tsukruk V V 2005 Intensive electric arc interaction with polymer surfaces: Reorganization of surface morphology and microstructure *Polymer* **46**(18) 7028–36

[8] Onchi T, Yanase H, Yamazaki M, Kuroda M, Isozaki M, Sugiyama S, Hata J and Yonemitsu K 2007 Properties of arc initiated between the parallel polymer plates *IEEJ Trans. Power and Energy* **127**(6) 692–8

[9] Nossov V V, Hage B, Jusselin B and Fievet C 2007 Simulation of the thermal radiation effect of an arc on polymer walls in low-voltage circuit breakers *Technical Physics* **52**(5) 651–9

[10] Ma Q, Rong M, Murphy A B, Wu Y, Xu T and Yang F 2008 Simulation and experimental study of arc motion in a low-voltage circuit breaker considering wall ablation *IEICE Trans. Electronics* **E91-C**(8) 1240–8

[11] Tanaka Y, Sakuyama T, Yamada D, Uesugi Y, Kanedo S and Okabe S 2008 Effect of polymer ablation on temperature decay of thermal plasmas using induction thermal plasma irradiation technique *Proc. 17th Int. Conf. on Gas Discharges and Applications (Cardiff, UK)* pp 89–92 paper 89

[12] Tanaka Y, Takeuchi Y, Sakuyama T, Uesugi Y, Kaneko S and Okabe S 2008 Numerical and experimental investigations of thermal interaction between thermal plasma and solid polymer powders using induction thermal plasma technique *J. Phys. D: Appl. Phys.* **41** 025203 (15pp)

[13] Vavra Z and Tuma J 2009 A study of electric arc – Polymer materials interaction *18th Symposium on Physics of Switching Arc, FSO 2009; Brno; Czech Republic* 300–3

[14] Becerra M, Piva D, Gati G and Dominguez G 2011 *Proc. 19th Symposium on Physics of Switching Arc 2011, FSO 2011; Brno; Czech Republic* 113–6

[15] Imae T, Kuroki Y, Gaja K, Kaneko E, Hayashida T and Nishi T 2011 Ablation characteristics of the different kinds of polymer insulators *Proc. First International Conference on Electric Power Equipment – Switching Technology, ICEPE2011 (Xi'an, China)* No. 6123062 598-601

[16] Sakuyama T, Tanaka Y, Uesugi Y, Kaneko S and Okabe S 2012 Plasma-quenching efficiency of ablated vapor of polymer containing nitrogen atoms using inductively coupled thermal plasma technique *Electr. Eng. Japan* **178** 461–8

[17] Jonsson E, Runde M, Dominguez G, Friberg A and Johansson E 2012 Arc quenching performance due to ablation; Comparison between four common polymers *Proc.*

26th International Conference on Electrical Contacts, ICEC 2012 (Beijing, China) **2012**(605) 41–4

[18] Onchi T, Tanaka Y and Uesugi Y 2012 Effect of polymer ablation gas on arc quenching properties around current zero *Electr. Eng. Japan* **180**(3) 32–45

[19] Becerra M and Gati R 2013 Time-resolved ablation of polymers exposed to ac arcs in air *Proc. 20th Symposium on Physics of Switching Arc 2013, FSO 2013; Brno; Czech Republic* 84–7

[20] Fei Yang, Yi Wu, Mingzhe Rong, Hao Sun, Anthony B Murphy, Zhigang Ren and Chunping Niu 2008 Low-voltage circuit breaker arcs – simulation and measurements *J. Phys. D: Appl. Phys.* **46** 273001 (19pp)

[21] Okano Y, Kaneko E and Hayashida T 2013 Study on polymer insulators in air discharge *Proc. Second International Conference on Electric Power Equipment – Switching Technology, ICEPE-ST 2013 (Matsue, Japan)* 3-a2-P-1 6804388

[22] Becerra M and Friberg A 2014 Arc jets blown by outgassing polymers in air *Proc. Int. Conf. on Gas Discharge and their Applications* pp 75-78

[23] Choi Y K and Shin J K 2015 Arc Gas-Flow Simulation Algorithm Considering the Effects of Nozzle Ablation in a Self-Blast GCB *IEEE Trans. Power Delivery* **30**(4) 1663–8

[24] Aminlashgari N Becerra M and Hakkarainen M 2016 Characterization of degradation fragments released by arc-induced ablation of polymers in air *J. Phys. D: Appl. Phys.* **49** 055502 (9pp)

[25] Tanaka Y, Numada T, Kaneko S and Okabe S 2005 Thermodynamic and transport properties of polymer ablated vapors and influence of their inclusions on Ar induction thermal plasma temperature *JSME International Journal, Ser.B* **48**(3) 417–24

[26] Tanaka Y, Shinsei N, Amitani K, Wada J and Okabe S 2011 Spallation particle ejection from polymer surface irradiated by thermal plasmas *IEEE Trans. Plasma Sci.* **39**(11) 2776–7

[27] Nakagawa T, Nakano T, Tanaka Y, Uesugi Y and Ishijima T 2015 Numerical simulation on dynamics and thermal decomposition of spallation polymer particles flying in polymer ablated arcs *Trans.IEEJ* **135**(11) (7pp)

[28] Shinsei N, Ishida M, Tanaka Y, Uesugi Y and Ishijima T 2012 *Joint Conference of IWHV2012 & JK 2012 on ED & HVE* ED-12-122, SP-12-050, HV-12-053 (6pp)

[29] Glaizes A, Razafinimanana M and Vacquie S 1986 Calculation of Thermodynamic Properties and Transport Coefficients for SF_6-N_2 Mixtures in the Temperature Range 1,000-30,000 K *Plasma Chemistry and Plasma Processing* **6**(1) 65–78

[30] Andre P and Koalaga Z 2010 Composition of a thermal plasma formed from PTFE with copper in non-oxidant atmosphere. Part I: definition of a test case with the SF_6 *High Temperature Material Processes (An International Quarterly of High-Technology Plasma Processes)* **14**(3) pp.279 <hal-00537752>

Chapter 3

Evaluation of arc quenching characteristics of various gases using power semiconductors

3.1 Introduction

A gas circuit breaker uses SF_6 gas as an arc quenching medium because SF_6 gas has quite high arc-quenching ability and current interruption ability. However, SF_6 has been specified as a greenhouse gas because it has a 22 800 times higher global warming potential (GWP) than CO_2 has. Consequently, it is necessary to reduce the amounts of SF_6 released to the atmosphere by reducing the amounts of SF_6 that are used. One solution for reduction of SF_6 use is to develop alternative gases for SF_6. Some alternative candidates have been investigated to date, such as high pressure CO_2, CO_2-CF_3I, CO_2-CH_4, and N_2-H_2 [6–9]. Recently, fluoronitrile-CO_2 mixture and fluoroketone-CO_2 mixture has been proposed as alternatives to SF_6 [11, 12]. Other approaches to reduce the amount of SF_6 use are to reduce the GCB size with less deterioration of the interruption ability. To substitute SF_6 with alternative materials or to reduce the GCB size, detailed understanding of residual arc properties in the current interruption process is fundamentally important.

The author has been investigating decay processes of gas-blast arcs fundamentally using both numerical [31, 32] and experimental approaches. For the experiment, the author has developed a simple arc device [9]. In the device, an arc plasma can be established between the moving electrode and the fixed electrode in the nozzle space. As a power source, a DC current source has been set up. Its output current can be switched using a

power semiconductor, e.g. insulated gate bipolar transistor (IGBT). The use of IGBT can control the arc current injection or voltage application accurately within a microsecond. By adopting time-accurate control of the current injection and voltage application, the author measured the electron density in arcs around current zero and under free recovery conditions in a gas flow using laser Thomson scattering (LTS) [37,38] and Shack–Hartmann type laser wavefront sensors [39]. In addition to these, the author have developed a new fundamental investigation technique for arc behaviours during the re-ignition process [13,34,35]. This technique uses IGBTs to control not only the arc current but also applied voltage with high accuracy in a time domain. Using the technique, transient voltage can be applied intentionally between the electrodes at specified timing under the free recovery condition. This applied voltage is called "quasi-transient recovery voltage (quasi-TRV)" because it is generated artificially. By application of this quasi-TRV, ones can study arc re-ignition processes and recovery properties in a thermal mode.

In this work, the author systematically obtained the arc quenching properties of SF_6, CO_2, O_2, N_2, air, and Ar using the developed technique [13]. A direct current 50 A arc was ignited in each gas flow at a given flow rate in the nozzle space and was sustained in a steady state. Subsequently, the arc current was commutated by IGBT from the arc plasma to the IGBT to produce the arc under free recovery condition. The arc decay process under the free recovery condition is the most basic property for arc-interruption phenomena. Arc behaviours in a steady state and in a decaying phase were observed using a high-speed video camera. Furthermore, the author found the systematic data on the interruption probability of each gas as a function of the timing of quasi-TRV application through more than 10–30 shots, which can be regarded as the recovery properties in a thermal mode. Electron density measurements were also taken at the nozzle throat using LTS to study arc decaying processes in various gas flows. In addition, numerical simulation was undertaken to investigate the temperature decay process of the arc under a free recovery condition for various gases. All data obtained from the experiments and simulation will be useful to elucidate the arc quenching physics and also for practical application of arc quenching phenomena.

3.2   Experimental setup

3.2.1   Electric circuit for current injection and voltage application

Figure 3.1 depicts the electrical circuit used for this work. The electric circuit has a direct current (dc) source, an IGBT element, and an arc device. The dc current source is an inverter type of dc current source rated at 150 A and 250 V. This dc current source is connected in series to the arc device to sustain an arc discharge between the electrodes in the arc device. To the electrodes, an IGBT element ($IGBT_p$) is connected in parallel. Switching-on this $IGBT_p$ can commutate the arc current from the arc discharge between the electrodes to the $IGBT_p$. This switching-on the $IGBT_p$ creates a free recovery condition between the electrodes, in which the arc discharge decays with time without current injection and voltage application. In addition, at the specified timing during arc decay, switching-off the $IGBT_p$ can apply the source voltage again to the decaying arc discharge between the electrodes. At that time, a steep voltage from the current source is applied respectively between the electrodes with a peak and a rise rate of 1.1 kV and 1.7 kV/μs, respectively. This applied voltage is called 'quasi-transient recovery voltage (quasi-TRV)' because it is similar to a regular TRV, but it is artificially generated. One feature of the use of the IGBT element is that it can provide high time accuracy to create the current commutation for a free recovery condition and the application of quasi-TRV. The IGBT element has a short response time and jitter of less than 1.0 μs. Therefore, the quasi-TRV can be applied to the decaying arc discharge at the specified delay time t_d from initiation of the arc decay.

When the quasi-TRV is applied during the arc decay, then the arc plasma is re-ignited in some conditions. This arc re-ignition is regarded as a current interruption failure. If the arc plasma continues to decay in spite of the quasi-TRV application and the current converges to zero, then this situation is regarded as a successful interruption. The probability of the successful interruption depends on the delay time t_d for quasi-TRV application. In addition, this successful interruption probability versus t_d is strongly dependent on the gas species, the gas flow rate, and other factors that determine the arc quenching ability. The voltage between the electrodes was measured using a CR potential divider. The source current, the arc current, and the IGBT current were measured respectively using current
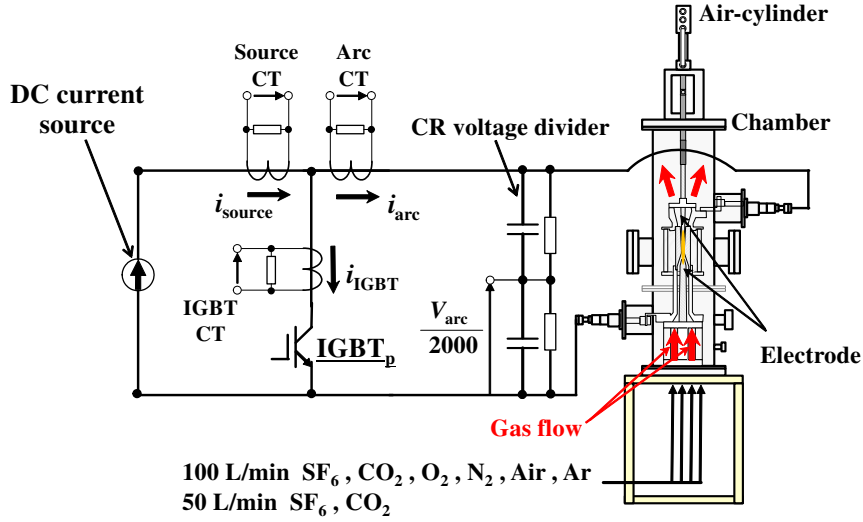
Fig. 3.1: Schematic of the experimental electric circuit.

transformers.

3.2.2   Configuration of the arc device and the nozzle

Figure 4.2 depicts the configuration of the arc device used in this work. The arc device consists of a vacuum chamber, a moving electrode and a fixed electrode, and a nozzle for gas flow. The outer diameter of the chamber is 200 mm. The upper electrode, which works as the anode, is the moving electrode driven by a compressed air cylinder. The lower electrode works as the cathode. It is the fixed electrode. These electrodes are surrounded by a gas-blast nozzle.

Figure 4.3 presents a schematic diagram of the nozzle and the electrodes, and a photograph of the nozzle made of transparent polymethylmethacrylate (PMMA). The electrode tips are made of copper tungsten (70%Cu-30%W). The moving electrode has 6 mm body diameter and 3 mm tip diameter. The body diameter and the tip diameter of the fixed electrodes are, respectively, 30 mm and 10 mm. The gap separating these electrodes has a distance of 50 mm at a full open position. These electrodes are surrounded by the nozzle. The gas inlet diameter is 40 mm, whereas that of the outlet is 18.75 mm. This nozzle has a throat with 10 mm diameter and 10 mm length. The author used nozzles made of polytetrafluoroethylene (PTFE) for arc tests. For observation of arc behaviour in the nozzle only, a nozzle made of transparent PMMA was used.
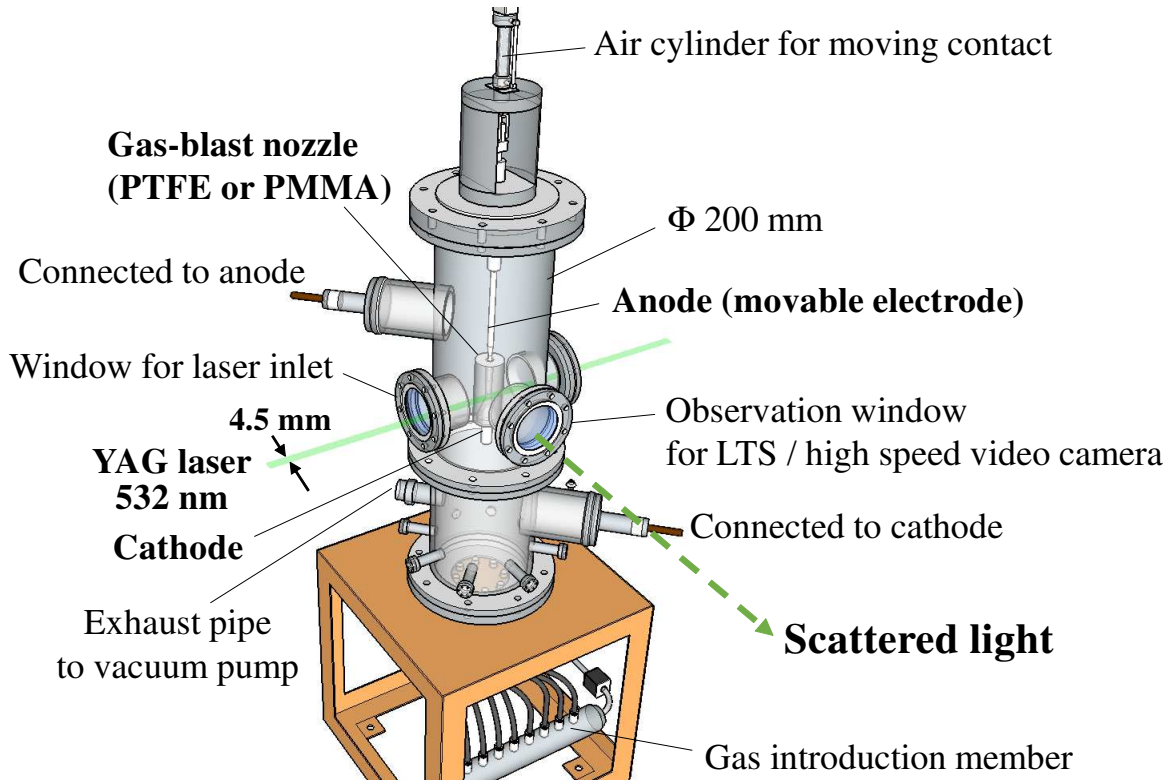
Fig. 3.2: Experimental arc device.

3.2.3 Experimental arrangements for Laser Thomson scattering method

Laser Thomson scattering (LTS) is widely used for precise measurements of electron density in arc plasmas. When a laser light is injected to an arc plasma, free electrons in the arc plasma are excited by electromagnetic field of the laser light, resulting in the light scattering. This is called Thomson scattering. One of the characteristics of LTS measurement is that it can measure local values of electron density and electron temperature without local thermodynamic equilibrium (LTE) assumption [16]. Details for LTS measurements have already been described for this system in a previous literature [37].

Electron density in the arc near the nozzle throat is a key physical parameter to ascertain arc interruption phenomena. The electron density at the nozzle throat was measured using LTS method. One characteristic of LTS measurement is that it can measure local values of electron density and electron temperature without a local thermodynamic equilibrium (LTE) assumption [16]. For LTS measurement, the second harmonic of an Nd:YAG laser at
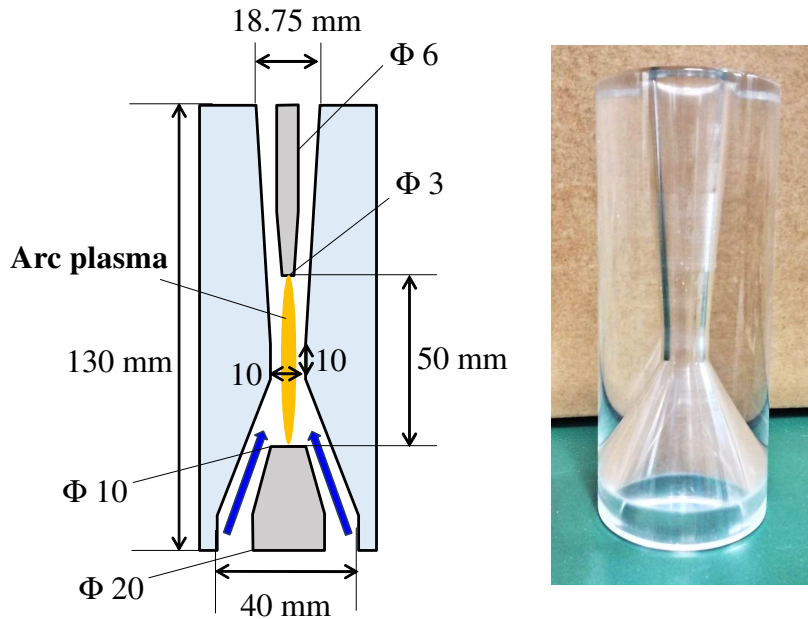
Fig. 3.3: Schematic diagram of a gas-blast nozzle and a photograph of a PMMA transparent nozzle.

a wavelength of 532 nm was used. The pulse width of the laser beam was 10 ns. The laser energy was 200 mJ. Figure 4.5 shows an image of the PTFE nozzle for LTS measurement and schematic cross sections of the nozzle. As this figure shows, the PTFE nozzle has a hole with 3.5 mm × 3 mm and a hole 10 mm × 3 mm for LTS measurement. These holes are positioned at the nozzle throat, which is at a height of 28 mm from the lower electrode surface. These two holes are arranged in a horizontal direction and are mutually perpendicular. The smaller hole is for the incident laser beam path. The larger hole is for observation of 90º scattered laser light. The laser beam has a focused spot diameter of less than 0.5 mm. However, the laser beam size is spread intentionally in the horizontal direction using a cylindrical lens to have 4.5 mm width. The horizontally spread laser beam is used because the laser beam can be irradiated to the arc column even if the arc axis is shifted from the nozzle axis. The arc plasmas in SF_6 or CO_2 flow are well known to be unstable and to fluctuate. The larger hole was covered with glass plates to prevent hot gas ejection from the holes. The covering hole by glass plates reduced influences of the hole on the arc behaviours.
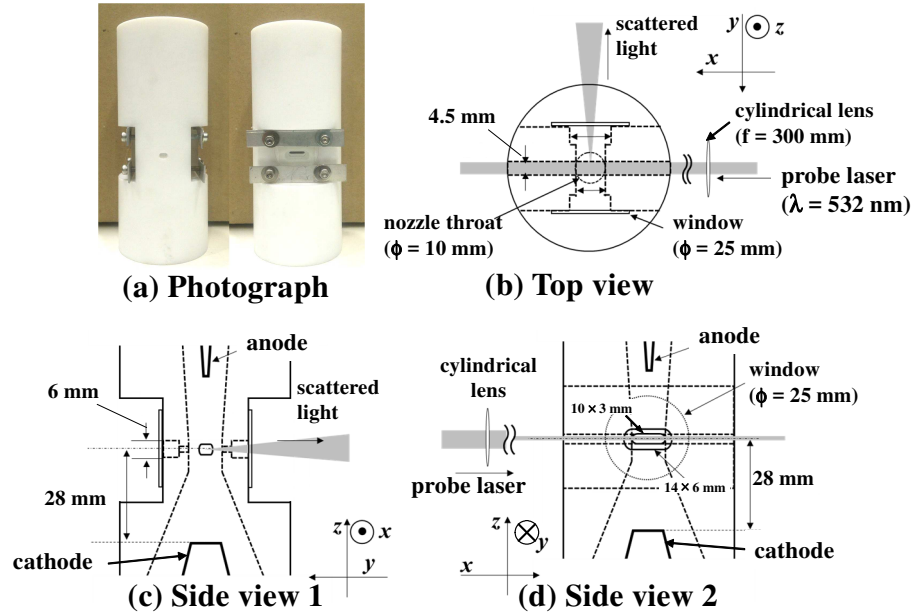
Fig. 3.4: PTFE nozzle for electron density measurement using laser Thomson scattering (LTS): (a) photograph of the PTFE nozzle from both sides, (b) top view of the cross section of the nozzle, (c) view from the laser inlet side, and (d) view from the observation side.

3.3 Experimental measurements

3.3.1 Experimental condition and procedure

The author used gases SF_6, CO_2, O_2, N_2, air, and Ar with a 100 L/min flow rate which corresponds to a gas flow velocity of 1.768 m/s at the nozzle inlet, and SF_6 and CO_2 with a 50 L/min flow rate which corresponds to a gas flow velocity of 0.884 m/s at the nozzle inlet. The electric arc current was fixed at dc 50 A. The pressure inside the chamber and the nozzle at the initiation of an arc discharge was set to 0.1 MPa. The arc behaviour was observed using a high-speed video camera. Its frame rate was set to 300 000 frames/s. The exposure time was 1.0 μs. The PMMA nozzle was used only for the high-speed video camera observation. In other experiments, the PTFE nozzle with holes was used for LTS measurement and also for evaluation of the arc quenching ability of the gases. The author measured the output current of the dc current source (i_{source}), the current between the electrodes (i_{arc}), the current in $IGBT_p$ (i_{IGBT}), the voltage between the electrodes (V_{arc}), and the $IGBT_p$ gate voltage and the electrode driving voltage.

Figure 4.6 presents an example of the measured current and voltage waveforms through

one experiment. The experimental procedure is explained below.

1. Before the experiment, the electrode is closed by supplying ac 100 V of the electrode driving voltage, as shown in panel (f). The $IGBT_p$ is switched off, which can be done by application of the gate voltage of -15 V as shown in panel (e).

2. The chamber including the arc device is evacuated using a vacuum pump to reduce the pressure inside the chamber to about 50 Pa. Subsequently the valve between the chamber and the vacuum pump is shut.

3. Gas is supplied from the lower part of the chamber at specified inlet flow velocity: 1.768 m/s (= a gas flow rate of 100 L/min) or 0.884 m/s (=50 L/min).

4. When the pressure inside the chamber reaches 0.1 MPa, the electric source current of 30 A is supplied to the closed electrodes for 100 ms. This process is shown at $t=-0.47$ s to -0.37 s in panels (a) and (b) of figure 4.6. Subsequently, the current source increases the current from 30 A to 50 A in 20 ms, corresponding to waveforms from $t=-0.37$ s to -0.35 s in panels (a) and (b).

5. At 120 ms after the current reaches 50 A, the upper electrode is initiated to open by stopping application of the electrode driving voltage as presented in panel (f). The duration of 80 ms is necessary for the moving electrode for its full opening stroke. At this time, the arc plasma is established between the electrodes. The arc voltage is increased with the stroke.

6. After opening the electrode, arc plasma of dc 50 A is sustained in 160 ms between the electrodes. Then, the arc voltage becomes stable in this steady state. One can find the stable arc voltage in time from -0.1 s to 0 s in panel (d). From this time region, the arc is observed using a high-speed video camera.

7. At $t=0$ s, the $IGBT_p$ is switched-on to commutate the source current from the arc plasma to the $IGBT_p$. As a result, the arc current and arc voltage smoothly decrease respectively to 0 A and 0 V. leading to the so-called free recovery condition.

8. After a specified delay time t_d from the $IGBT_p$ switching-on, the $IGBT_p$ is switched-off again. This switching-off of the $IGBT_p$ applies a quasi-TRV to the electrodes. If the
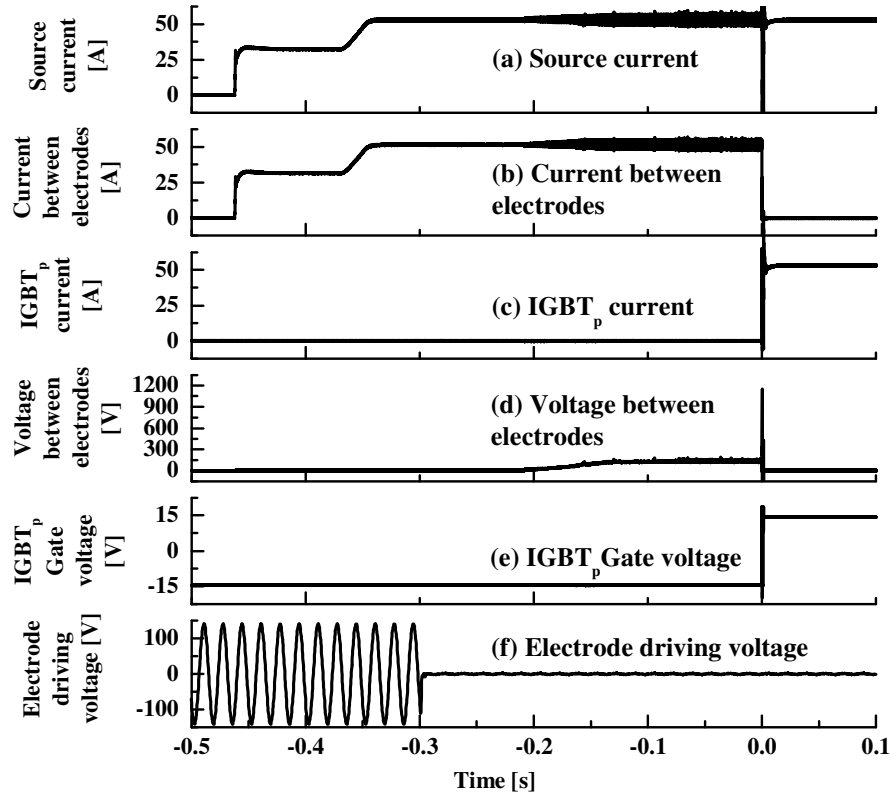
Fig. 3.5: Example of measured current and voltage waveforms through one experimental shot.

arc current increases between the electrodes after quasi-TRV application, then judge the arc re-ignition and the current interruption failure. If the arc current continues to decrease to 0 A, then judge the successful current interruption. In this work, t_d can be set from 10 μs to 500 μs.

9. After 1.0 ms from initiation of quasi-TRV application, the $IGBT_p$ is switched on again to commutate the current from the arc plasma to the IGBT.

10. The current source is turned off to halt the experiment.

This experimental procedure provides (I) a gas blast arc sustained in a steady state, (II) free recovery condition generated using the IGBT control, (III) application of quasi-TRV to the electrodes, and (IV) judgment between the success or failure of current interruption.

3.3.2   Application of quasi-transient recovery voltage to gas-blast arcs under a free recovery condition

Figures 3.6 and 3.7 respectively present the conceptual diagram of the source current, the arc current, and the voltage between the electrodes, in cases of successful interruption and arc re-ignition. These figures include only the waveforms around the current commutation and quasi-TRV application. Successful interruption is recognized when the electric current continues to decrease even after quasi-TRV application. However, if the current increases through the residual arc after quasi-TRV application, it is recognized as the interruption failure or arc re-ignition. From the waveforms of the current and voltage between the electrode, one can judge successful interruption and interruption failure clearly. Furthermore, changing the delay time t_d enables the author to investigate the dielectric recovery property between the electrodes. At the same time, arc behaviour was observed using a high-speed video camera to study the arc decay and the position of the electrical breakdown between the electrodes.

It is necessary to fix the quasi-TRV waveform for comparison. Figure 3.8 presents the prospective waveform of quasi-TRV. The vertical axis shows voltage between the electrodes. The horizontal axis presents time from initiation of a quasi-TRV application. The prospective quasi-TRV is an oscillating voltage governed by inductance in the dc current source and a strayed impedance in the circuit. The first peak of the quasi-TRV reaches 1.1 kV. Its rise rate is 1.7 kV /μs. In this work, the quasi-TRV is applied to an arc plasma under a free recovery condition.

3.4   Experimental results

3.4.1   Arc shape and arc voltage in a steady state before the free recovery condition

Before describing arc decaying processes under free recovery condition, the arc behaviour under a steady state condition before the free recovery condition is shown because arc stability under a steady state condition with a gas flow is fundamental and is then also related to the arc behaviour under a transient condition.

Figure 3.9(a) depicts arc behaviour in a steady state in SF_6 with inlet flow velocity of 1.768 m/s (= a gas flow rate of 100 L/min) and 0.884 m/s (=50 L/min). The shape of the nozzle and the electrodes are drawn with white lines. The gas inlet is located at the bottom of the figure. Each image is captured by a high speed video camera with a sensitivity for visible light in a wavelength range from 400 to 800 nm. Originally, the radiation of visible light from the arc is expressed as a monochrome image signal with a depth of 8 bits = 256 levels. The author have converted this monochrome image signal to coloured image signal according to the magnitude of radiation intensity. Here, the red colour corresponds to high intensity and the blue indicates low intensity. The images shown here are colour maps on a logarithmic scale. The images include timings of photographs on the bottom of the figure. The time base is equivalent to that of figure 4.6. As the pictures show, the SF_6 arc has a frequently changed shape in the nozzle space, even with spiral shapes for 1.768 m/s and 0.884 m/s. This shape instability of the arc might originate from the turbulent flow because of SF_6 characteristics. Generally, SF_6 has a heavy mass density and a high Reynolds number (Re), that can be written as

$$Re = \frac{\rho u L}{\mu} \tag{3.1}$$

where ρ is the mass density of the gas, u is the velocity of the gas flow, μ is the viscosity of the gas, and L is a characteristic length like the size of the gas flow inlet. Higher Reynolds number of SF_6 gas flow with higher mass density is thus subject to the production of turbulent flows. Furthermore, SF_6 can be dissociated thermally to SF_4, SF_2, SF, respectively, at 1800 K, 2000 K and 2200 K involving local expansion and also causing turbulent flow. These dissociations also offer a high specific heat and thermal conductivity of SF_6, leading to a high arc quenching ability, which also might make the arc discharge unstable and fluctuating. The arc current and voltage in the steady state are presented in figure 3.10(a) for SF_6 gas inlet flow velocity of 1.768 m/s and 0.884 m/s. The upper panel presents the arc current. The lower panel presents the arc voltage. As shown there, the arc current was almost constant around dc 50 A. The arc voltages fluctuate considerably, especially for the case of 1.768 m/s inlet flow velocity. The arc voltage fluctuation is attributable to arc length fluctuation by turbulent flow. In spite of that, these SF_6 arcs at 50 mm length could be sustained because of a direct current input.

The arc behaviours in CO_2 gas flow were also measured as depicted in figure 3.9(b) for

inlet flow velocity of 1.768 m/s and 0.884 m/s. The CO_2 arc is also bent with 1.768 m/s inlet flow, not markedly compared to SF_6 arcs. However, the CO_2 arc with 0.884 m/s inlet velocity has a straight stable shape. This stability can be confirmed in the measured arc voltage, as presented in figure 3.10(b). As the figure shows, the arc voltage for 0.884 m/s inlet flow velocity is absolutely stable around 120 V, whereas the arc voltage with 1.768 m/s inlet flow velocity shows random fluctuation. CO_2 has relatively higher density than air and N_2, but it is quite lower compared to that of SF_6. Only the higher inlet flow velocity can cause appearance of turbulent effects for CO_2 arcs.

The arc behaviours in a steady state are presented in figure 3.11 in O_2, N_2, air, and Ar with 1.768 m/s inlet flow velocity. As shown in this figure, arcs in these gas flows have quite a straight shape stably. Moreover, it is well controlled with almost no fluctuation. The main difference between these gas arcs is the diameter of the arcs. The Ar arc has the largest diameter among the gases. The second largest arc is the O_2 arc. The N_2 and air arcs seem to have similar diameters. The Ar arc has the largest diameter because Ar has noble gas without dissociations leading to energy consumption and then shrinkage of the arc plasma. Figure 3.12 presents the arc current and voltage in O_2, N_2, air, and Ar with 1.768 m/s inlet flow velocity. The arc voltage waveform in each gas is stable only with voltage fluctuation from the inverter current output. The N_2, air and O_2 arcs have similar arc voltage of around 110–130 V. That of O_2 is slightly lower than that of either N_2 or air. The arc voltage of Ar is about 50 V. It is markedly lower than others. In terms of passage diameter of the current, these results of the arc voltage show good agreement with the observed arc diameters shown in figure 3.11.

3.4.2 Dynamic arc behaviours in the decaying phase

Figure 3.13(a) depicts the arc behaviour in a decaying phase under free recovery conditions in SF_6 gas flow at inlet flow velocity of 1.768 m/s. This figure presents images taken at the timing t of 0, 3.3, 6.7, 10, 20 and 30 μs from the initiation of the arc decay. As the pictures show, the SF_6 arc discharge decays with time, keeping its shape at time 0 μs. The radiation intensity from the SF_6 arc decreases almost uniformly along the arc, roughly speaking, although some parts, between the lower electrode and the nozzle throat inlet for example, decline more rapidly. As a result, at t=20 μs, the radiation from the arc becomes

very weak, remaining downstream of the nozzle throat in this case. Furthermore, at $t=30$ μs, the arc plasma has weak radiation in the nozzle space. If SF_6 with the inlet flow velocity of 0.884 m/s is blown, then the arc behaviour is distinctive, as depicted in figure 3.13(b). In this case, the arc plasma also decays over the entire part of the nozzle space with a slightly lower decay rate than that at 1.768 m/s. However, one distinct feature is the local rapid decay in the arc plasma along the arc. In spite of that, rapid decay in the radiation intensity between the lower electrode and the nozzle throat is obtainable. Such a reduction and local rapid decay along the arc plasma are attributed to a high arc quenching ability of SF_6 and turbulent effects.

In the case of CO_2, local decay from the gas flow around the nozzle throat is apparent. Figure 3.14 presents the arc behaviour in a decaying phase in CO_2 with inlet flow velocity of 1.768 m/s and 0.884 m/s. For both cases, CO_2 arc decay was initiated near the nozzle throat. Fast decay around the nozzle throat is apparent, especially in the case of 1.768 m/s. At $t=6.7$ μs, the radiation intensity around the upper side of the nozzle throat already became much weaker than other parts. At $t=30$ μs, the intensity also at the lower side of the nozzle throat decreases with time. As this figure shows, the CO_2 gas flow enhances the arc plasma decay around the nozzle throat, which implies the importance of the nozzle throat for CO_2 arc decay. This tendency is also apparent in case of 0.884 m/s inlet flow velocity, but the decay rate at 0.884 m/s is much lower than that at 1.768 m/s.

The arc behaviours in decaying phase in O_2, N_2, air and Ar are obtainable in figure 3.15 at inlet flow velocity of 1.768 m/s. The arc decaying process depends on the gas kinds markedly. The O_2 arc still has a high radiation intensity at $t=10$ μs, whereas the radiation intensity from the N_2 and air arcs decreases faster than that of O_2 arcs. Through a test, a nozzle burned with a flame in a case of O_2 gas introduction. It would be thus possible that combustion of ablation vapour restrains a decrease in radiation intensity from O_2 arcs. Similarly, the radiation intensity from the air arc is comparably higher than that of the N_2 arc at 30 μs. For O_2, N_2 and air arcs, the arcs decline remarkably around the nozzle throat. The Ar arc shows a gradual and slow decay in the radiation intensity.

High-speed video camera observations confirmed that the nozzle throat plays important roles in arc decay in most cases. At the nozzle, cold gas from the inlet is blown directly to the arc plasma, which results in high convection loss to reduce the arc diameter; then

a high thermal conduction loss there. However, those effects on decaying arcs in each gas mutually differ. Such behaviour is obtainable by numerical simulation, as described in a later section.

3.4.3   Probability of successful interruption versus quasi-TRV application

One important feature of experimental tests in this work is to estimate arc interruption ability by application of quasi-TRV in the fixed conditions. In a free recovery condition, quasi-TRV was applied by switching off the IGBT again at a specified delay time $t_{\rm d}$. This test was applied to investigate the recovery properties of the space between the electrodes.

Figure 3.16 presents the IGBT signal, the arc current, and the arc voltage for a SF_6 arc with 1.768 m/s inlet flow velocity for $t_{\rm d}$=20 μs. The arc current is commutated to the IGBT at t=0 μs by switching on the IGBT. In this case, the arc current has a finite current decay rate di/dt because it requires a finite time for transition of IGBT from off-state to on-state, and circuit inductance. At $t_{\rm d}$=20 μs, the IGBT is switched off again to apply source voltage of 1.1 kV with a rise rate of 1.7 kV/μs between the electrodes. As panel (a) shows, the arc current continues to decrease to 0 A with time, which is regarded as successful interruption. Panel (b) depicts the waveforms in the interruption failure case, although the same delay time $t_{\rm d}$=20 μs for quasi-TRV application was used. In this figure, the arc current again increases to 50 A through arc re-ignition at applied voltage of 0.75 kV. This interruption failure seems to be a thermal failure or a failure in a thermal mode, not in a dielectric mode, because the arc current increases gradually with time during 8 μs. Generally in a dielectric mode, the current jumps up with a voltage drop at the arc re-strike. In this way, successful interruption occurs with a certain probability. If the delay time $t_{\rm d}$ for quasi-TRV application is sufficiently long, then the probability of successful interruption reaches 100%. When $t_{\rm d}$ is short, the arc is always re-ignited easily between the electrodes.

Figure 3.17 presents the experimentally obtained probability of successful interruption in a thermal mode versus the delay time $t_{\rm d}$ for quasi-TRV application. This figure includes results for inlet flow velocity of 1.768 m/s. Each of the probabilities was obtained through

10–40 shots for each condition. As this figure shows, SF_6 requires a delay time t_d less than 28 μs for quasi-TRV application to prevent arc re-ignition in thermal mode. In other words, a shorter t_d than 20 μs engenders arc re-ignition. In addition, an important matter for SF_6 is that the interruption probability increases extremely with t_d from 20 to 30 μs. That point above implies an extremely high arc interruption ability in a thermal mode and remarkably rapid recovery of SF_6 against voltage application. In other words, a SF_6 residual arc under a free recovery condition can lose its electrical conductivity at a point or points along the arc discharge between the electrodes. As a result, the delay time $t_{d50\%}$ = 28 μs obtains 50% successful interruption, where the $t_{d50\%}$ is defined as t_d, with which the interruption probability becomes 50%.

For other gases, much longer t_d is necessary for quasi-TRV application without arc re-ignition, compared to t_d for SF_6. The CO_2 and O_2 shows similar results for the interruption probability versus t_d. Therefore, these gases have similar recovery properties in thermal mode. For CO_2 and O_2, the quantity $t_{d50\%}$ can be estimated as 108 μs. Air and N_2 gases require longer t_d for successful interruption in thermal mode. The delay times for 50% successful interruption $t_{d50\%}$ were estimated as 190 μs for air and as 230 μs for N_2. It is reasonable that air shows results that are intermediate between N_2 and O_2 because air is a mixture of 78%N_2 and 22%O_2. However, Ar has an extremely long $t_{d50\%}$ of 480 μs, which indicates very slow recovery of Ar for electrical conductivity. This result is consistent with the fact that Ar is used widely as working gas for plasma applications for stable plasma sustainment.

The successful interruption property is related to recovery properties in a thermal mode, which depends on the decay rate in the electrical conductivity. The decay rate in the electrical conductivity is directly connected to decay in the electron density, and to the temperature. The temperature decay at the nozzle throat is again influenced by the gas flow convection loss with high specific heat at low temperature $\rho C_p \boldsymbol{u} \cdot \nabla T$ and the thermal conduction $\nabla \cdot \kappa \nabla T$, where ρ is the mass density, C_p denotes the specific heat, $\boldsymbol{u}$ represents the gas flow velocity, κ is the thermal conductivity, and T is the temperature. The gas SF_6 has a higher specific heat ρC_p and thermal conductivity κ at low temperatures of about 1800, 2000 and 2200 K, arising from dissociation–association reactions from SF_6 to SF_4, SF_4 to SF_2, and SF_2 to S and F. This higher specific heat and thermal conductivity are

favourable for decay of the temperature and electrical conductivity.

Such a successful interruption probability versus t_d can be adopted for different gas conditions such as gas flow rates. Figure 3.18 presents the probability of successful interruption versus t_d for SF_6 and CO_2 at two different inlet gas flow velocities of 1.768 m/s and 0.884 m/s. Open squares represent the results for 1.768 m/s SF_6 gas introduction. Open squares with a cross correspond to 0.884 m/s SF_6 gas introduction. Similarly, results for 1.768 m/s CO_2 gas introduction are shown by open triangles. Triangles with a cross are for 0.884 m/s CO_2 gas introduction. For SF_6 gas flow, the increase rate in the successful interruption probability versus t_d is rather gradual at 0.884 m/s compared to 1.768 m/s. As a result, $t_{d50\%}$ is estimated as 40 μs for SF_6 at 0.884 m/s, which is 1.4 times as long as $t_{d50\%}$ at 1.768 m/s. This result suggests a quantitative reduction in the interruption ability in a thermal mode by a decrease in the gas inlet flow velocity for SF_6. The interruption ability of CO_2 was also degraded by a decrease in the gas inlet flow velocity. Actually, the quantity $t_{d50\%}$ becomes 150 μs for CO_2 at 0.884 m/s, which is 1.4 times as long as $t_{d50\%}$ at 1.768 m/s. This result might imply that a decrease in gas inlet flow velocity from 1.768 to 0.884 m/s reduces the recovery rate similarly for SF_6 and CO_2.

The successful interruption probability versus the delay time t_d for voltage application was obtained systematically.

It is noted that the relationship between interruption probabilities versus t_d in figures 3.17 and 3.18 is just a relative relationship for different gas kind conditions and gas flow rates at a fixed TRV application. If higher voltage of TRV is applied, the results of figures 3.17 and 3.18 would be shifted to longer delay time side. This means that, longer time is needed for the space between the electrodes to recover enough to withstand higher TRV application. Nevertheless, the author could compare a relative relationship for different gas kinds and different gas flow rates. SF_6 could need only a shorter delay time for current interruption compared to the other gases because of SF_6's rapid recovery property. These data include useful information and contribute to the elucidation of arc interruption phenomena for fundamental and practical sides.

3.4.4   Waveforms of current and voltage on interruption failure

The experiment results revealed some interruption failure cases at the critical t_{d}. Figure 3.19 presents the waveforms of current and voltage on the interruption failure at the 1.768 m/s gas introduction. The upper panel presents the voltage between the electrodes. The lower panel presents the arc current. The horizontal axis shows the time from the initiation of quasi-TRV, t' in this figure. All waveforms were acquired as a 'failure case' with quasi-TRV application at nearly $t_{\mathrm{d50\%}}$, i.e. t_{d}, which provides 50% probability of successful interruption for each gas.

Figure 3.19(a) shows the current and voltage after quasi-TRV application at t_{d} of 30 μs for SF_6 at the 1.768 m/s gas introduction. In this case, the arc current started increasing just from $t' = 2$ μs. The voltage dropped, which means that the SF_6 arc was re-ignited almost at t'=2 μs. In this way, SF_6 arc re-ignition mostly occurs before the first peak of quasi-TRV, which might be attributable to the fact that the residual SF_6 arc channel remained at a high temperature and became conductive again because of joule heating by a small current injection. Otherwise the arc re-ignition is avoided by rapid quenching of SF_6. Therefore, the thermal mode determines the success or failure of current interruption at $t_{\mathrm{d}} = 30$ μs for SF_6.

Arc re-ignition occurs in CO_2 gas at 1.768 m/s inlet flow velocity as presented in figure 3.19(b) for $t_{\mathrm{d}} = 110$ μs. In this case, the arc was re-ignited at more than 5 μs after quasi-TRV application initiation. Many cases show such microsecond arc re-ignition for $t_{\mathrm{d50\%}}$ TRV application. In this figure, current of less than 5 A can be confirmed to flow immediately before the rapid increase in current. This result suggests that the residual CO_2 arc became conductive gradually because of joule heating caused by a small current after quasi-TRV application in a thermal mode. Figure 3.19(c) depicts the result for N_2 gas at 1.768 m/s and $t_{\mathrm{d}} = 240$ μs. In this case, the arc was re-ignited more than 10 μs after quasi-TRV application. Furthermore, the arc current increases and the voltage drops after re-ignition slowly because the electrical conductance change in N_2 arc was very slow in this case. From the results described above, it was also inferred that SF_6 gas has extremely high arc-quenching performance and high post-arc current withstand capability, and that CO_2 gas has medium quenching ability and post-arc current withstand capability, compared to N_2.

3.5   Discussion

3.5.1   Electron density measured using laser Thomson scattering

Through the current interruption tests, the electron density of the arc in decaying process was measured using the laser Thomson scattering (LTS) method [37, 38]. This section presents a description of a part of the measured electron density for consideration of current interruption capabilities of SF_6, CO_2, and N_2.

Figure 3.20 presents time evolutions in the electron density in SF_6, CO_2, and N_2 residual arcs under free recovery conditions at 1.768 m/s gas introduction. The LTS measurement was done at the nozzle throat outlet, as shown in figure 4.5. The nozzle throat is regarded as an important location for arc-quenching phenomena. Results for 3–5 shots were derived at each timing and for each kind of gas. A mean value and maximum and minimum values are shown with error bars in the figure. Before $t=0$ μs in this figure, the arc plasma is established using dc current of 50 A. At $t=0$ μs, the electron density n_e is 6.0×10^{22} m^{-3} for SF_6 and CO_2, whereas n_e is estimated as 10.0×10^{22} m^{-3}. After current decreases to 0 A at $t > 0$ μs, the electron density decreases rapidly with time. In N_2 gas, the electron density decreases gradually with time to reach 0.3×10^{22} m^{-3}. SF_6 and CO_6 cause a rapid decrease in the electron density with time. At $t=20$ μs, the electron densities for SF_6 and CO_2 become 1.1×10^{22} m^{-3}. Additionally, it is noteworthy that the electron density in SF_6 could not be determined from LTS at $t > 20$ μs because the electron density might decay to its lower limitation of $< 10^{21}$ m^{-3} detectable by LTS. This fact suggests a remarkable decay ability of SF_6 for the electron density at $t > 20$ μs compared to CO_2 and N_2.

These results of decay in the electron density show good agreement with the results on radiation intensity in arcs observed from high-speed video camera observation. As shown in figure 3.13, at $t=0$ μs, the shape of SF_6 arc tends to be a spiral. After current down to 0 A at $t > 0$ μs, the entire part of the residual SF_6 arc quickly decays simultaneously. Then the overall decay with some local decay in the residual arc can also be obtained at $t > 20$ μs. This quick decay of SF_6 arcs agrees with a rapid decay in the electron density shown in figure 3.20. However, the shape instability of CO_2 arcs is not as high as that of SF_6 arcs, as shown in figure 3.14. The CO_2 arc decays more rapidly from the vicinity of the nozzle throat, which is the LTS measurement point of the electron density. Figure 3.20

shows that these characteristics of a CO_2 arc might cause a rapid decay in the electron density at the nozzle throat. Finally, the N_2 arc is extremely stable. It decays slowly with time, as depicted in figure 3.15(b). Therefore, the obtained electron density is greater and decays with time more slowly than either SF_6 or CO_2, as presented in figure 3.20.

As described in this section, the results of the electron density measurement fairly agree with the arc behaviour observed using a high-speed video camera. In addition, no contradiction exists with the results of current interruption tests. Nevertheless, results also show that the current interruption is determined not only at one point of the nozzle throat, especially in SF_6. Further experiments must be conducted to elucidate the arc interruption phenomena.

3.5.2 Transient temperature distribution of various gas arcs in nozzle by numerical simulation

In several gas conditions, the arcs decayed from near the nozzle throat. To investigate the effects of the nozzle throat on arc decay, a numerical simulation of the arc in flows of different gases was conducted [31]. Numerical simulation uses the LTE model, with the following assumptions: (1) The calculation domain is axisymmetric. (2) The arc plasma is in an LTE condition. All temperatures such as electron temperature, heavy particle temperature, and excitation temperature are equal. In addition, all reactions including dissociation/ association and ionization/ recombination take place under the equilibrium condition. (3) The flow is laminar flow. Therefore, the turbulent effect is neglected. (4) The arc plasma is optically thin. (5) Phenomena on the electrode surface such as electron emission and ion bombardment are neglected. (6) The electric field has only an axial direction component. (7) The author neglects density fluctuations caused by pressure fluctuations in a steady state, but in a transient state it is included. (8) Ablation effects of the electrodes and nozzle are neglected. (9)The author considers heat conduction inside the electrodes and nozzle. Based on the assumptions presented above, the author solved the conservation equations of mass, momentum, and energy as well as electromagnetic fields, together with the equation of state. Thermodynamic and transport properties of each gas were calculated in advance as functions of temperature using the calculated equilibrium

composition of each gas. The program is a hand-made code based on All-speed SIMPLE algorithm reported by Patankar. Using this model, two-dimensional transient temperature and gas flow fields were calculated for SF_6, CO_2, and N_2 arcs.

Figure 3.21 presents the calculated two-dimensional temperature distributions of CO_2, N_2 and SF_6 arcs under a free recovery condition after a dc 50 A steady state condition. The temperature is expressed by a logarithmic colour scale. The configuration of the nozzle and electrodes is the same as that in the experiment, as presented in figure 4.3. Figure 3.21(a) depicts results for a CO_2 arc with 0.884 m/s gas introduction. It is readily apparent that the arc temperature decreases with time. Furthermore, a decrease rate in the arc temperature is greater around the nozzle throat, especially just at the nozzle throat inlet. Figure 3.14(b) shows that this calculated result agrees well with the time evaluation in the radiation intensity from CO_2 arcs. This rapid decay in the temperature around the nozzle throat inlet is attributable to high convection loss $\rho C_p \boldsymbol{u} \cdot \nabla T$ there because the gas flow velocity $\boldsymbol{u}$ is high and the radial temperature gradient ∇T is higher than at other positions. This high radial temperature gradient arises from the cooling gas flow supplied to the nozzle throat inlet. In addition, the calculated results for 1.768 m/s CO_2 gas introduction are found in figure 3.21(b). In this case, the arc temperature starts decreasing around the nozzle throat, exhibiting a more rapid decrease in the temperature at 1.768 m/s than at 0.884 m/s. Results showed further that the experimentally obtained results of the radiation intensity from a CO_2 arc with 1.768 m/s gas introduction in figure 3.14(a) seems to decay more rapidly than those predicted by the present numerical simulation in figure 3.21(a). Perhaps this is true because turbulent flow effects are not considered in the calculation model.

Figure 3.21(c) presents calculated results for a N_2 arc with 1.768 m/s gas introduction. The calculation model predicts that a N_2 arc also decays from the nozzle throat inlet. This calculated transient temperature distribution closely resembles the experimentally observed result depicted in figure 3.15(b), from viewpoints of the arc decaying spatial position. Therefore, the present LTE model can predict arc behaviour with validity because N_2 arcs are quite stable during both steady state and decay without turbulent effects etc. in the experiment.

However, a difference exists between the calculated result and the observed result for SF_6

arcs. Figure 3.21(d) represents the results for a SF_6 arc with inlet flow velocity of 1.768 m/s. The simulation predicts that SF_6 arc decays remarkably fast around the nozzle throat inlet because of a strong convection loss by cold and heavy SF_6 gas. This rapid decay in SF_6 arc temperature is attributed to the high convection loss caused by high specific heat, and high thermal conduction loss. The high specific heat and high thermal conductivity of SF_6 is involved equivalently by dissociation reactions of mainly SF_6, SF_4 and SF_2. This simulated temperature distributions shows a reasonably fast decay of the SF_6 arc, comparing with the observation result presented in figure 3.13(a). However, a difference between them remains. In the experiment, SF_6 actually produces strong turbulent flow, which makes the arc fluctuate. Furthermore, the actual SF_6 arc process is under a chemically non-equilibrium condition in which dissociation/ association reactions take finite time. Such turbulent effects and non-equilibrium effect should be considered in future work. In other words, the present comparison between the experimentally obtained results and the LTE simulated results are useful to ascertain the importance of these effects.

3.5.3   Influence of holes in the nozzle for LTS on arc behaviour

LTS measurements were done using a nozzle with a laser path hole and an observation hole. The observation hole was covered by a glass plate to prevent hot gas ejection from the nozzle throat, as described in the previous section. However, the current interruption test was conducted using nozzles with and without the holes. It is therefore necessary to confirm the influence of the presence of these holes in the nozzle on the arc behaviour.

Figure 3.22 shows the averaged arc voltage in a steady state in various gas conditions for the nozzles of the two types. One bar stands for results for the nozzle without the holes. The other bar shows results for the nozzle with holes for LTS measurement. The arc voltage measured from the time -5 ms to 0 ms was averaged for each gas condition. Each error bar is produced by at least 6 samples except a case of O_2 without a hole. As this figure shows, effects of the hole presence on the arc behaviours were not significant for all gases examined in this study. Except for SF_6, the arc voltage is slightly lower with the holes. Consequently, the influences of the hole presence might be neglected in the present work.

3.6   Summary of chapter 3

This chapter presents current interruption capabilities of various gas quantified using a newly developed method. The method uses an insulated gate bi-polar transistor (IGBT) as a current and voltage control device. SF_6, CO_2, O_2, N_2, air and Ar arcs in DC current of 50 A were ignited in a gas-flow nozzle, after which they decayed because of the current commutation to the IGBT parallel connected to the arcing electrodes. After specified delay time t_d from initiation of the arc decaying, a steep voltage was intentionally applied to the electrodes. A case in which the arc did not re-ignite is regarded as successful interruption. The probability of successful interruption was investigated statistically for every gas. Consequently, SF_6 was estimated as taking 28 μs to have 50% probability of successful interruption ($t_{d50\%} = 28$ μs): the fastest of these gases. Also, $t_{d50\%}$ of CO_2 was 108 μs. $t_{d50\%}$ of N_2 was 240 μs. In this way, current interruption capabilities of various gases can be evaluated quantitatively using the developed method. Furthermore, arc behaviour in a steady state and decaying phase were observed using a high-speed video camera. The electron density of the residual arc in decaying phase was measured using LTS method. Comparison between arc behaviour and the electron density showed good agreement. No contradiction was found with results of current interruption tests.

Results obtained in this work will support consideration of the fundamental characteristics of arc discharge and development of alternatives to SF_6. Additional approaches must be made to ascertain the fundamental properties of current interruption phenomena. The author is planning further investigation such as the influence of TRV peak voltage and rise rate using advanced technique with power semiconductors.
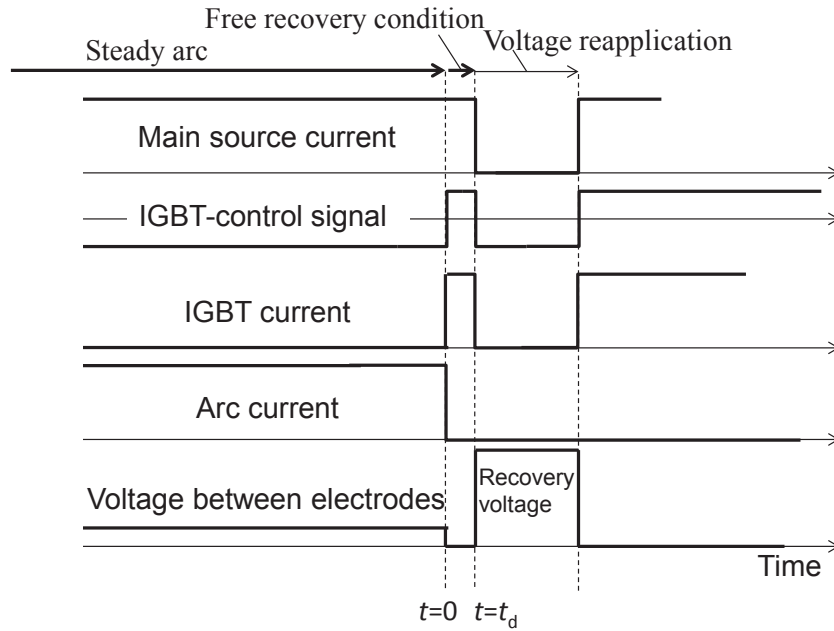
Fig. 3.6: Conceptual current and voltage behaviours in cases of success of arc interruption after quasi-transient recovery voltage application.
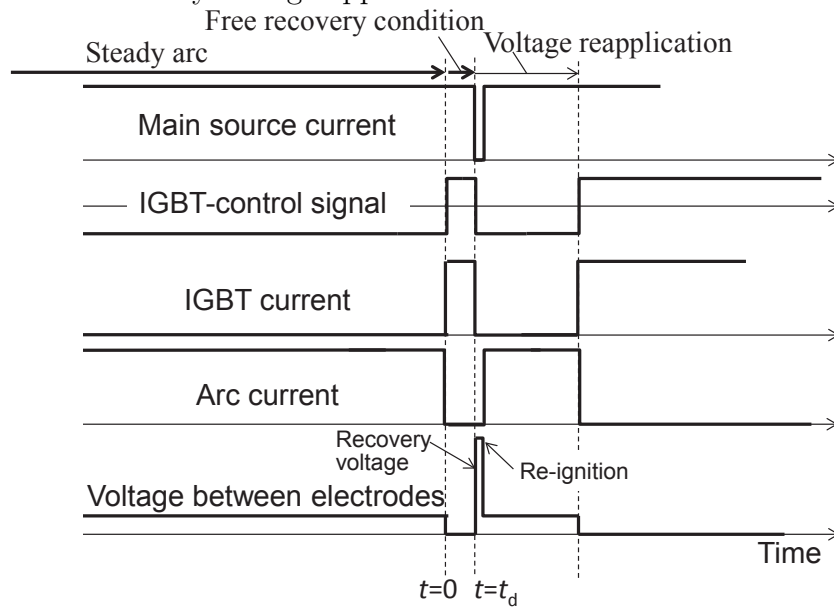
Fig. 3.7: Conceptual current and voltage behaviours in cases of arc re-ignition after quasi-transient recovery voltage application.
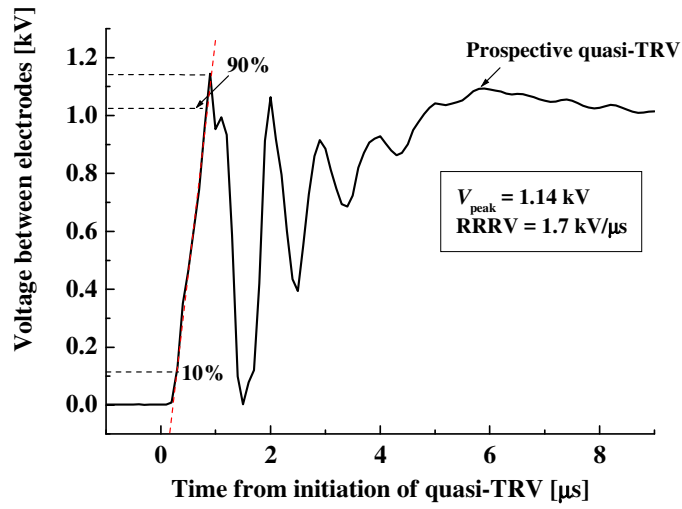
Fig. 3.8: Waveform of prospective quasi-transient recovery voltage (quasi-TRV).
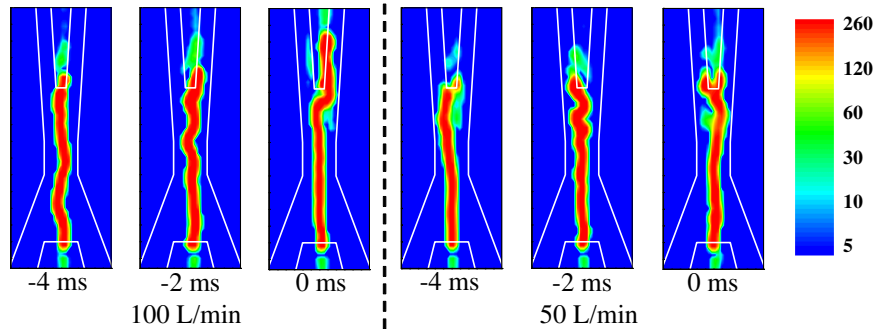
(a) SF_6
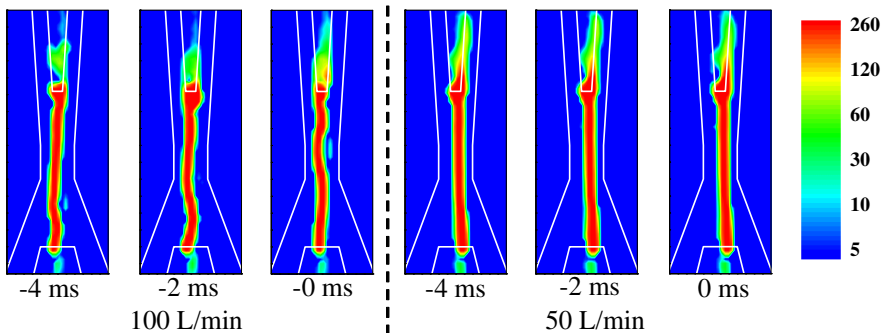
(b) CO_2

Fig. 3.9: Arc behaviour in a steady state before free recovery condition in (a) SF_6 and (b) CO_2 with 100 and 50 L/min flow rates (logarithmic scale colour map).
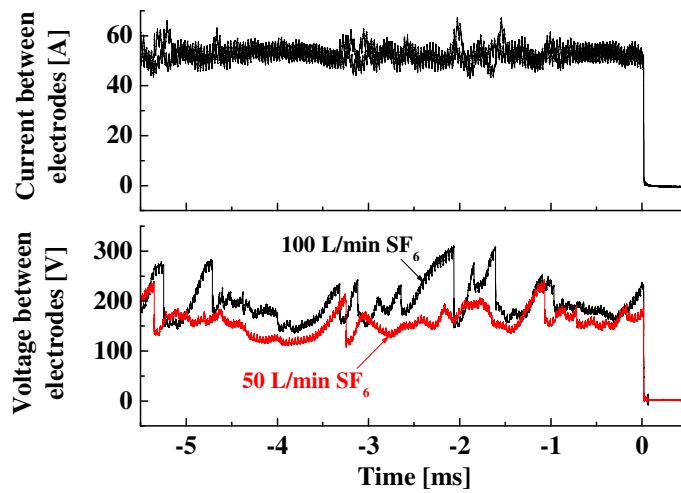
(a) SF_6
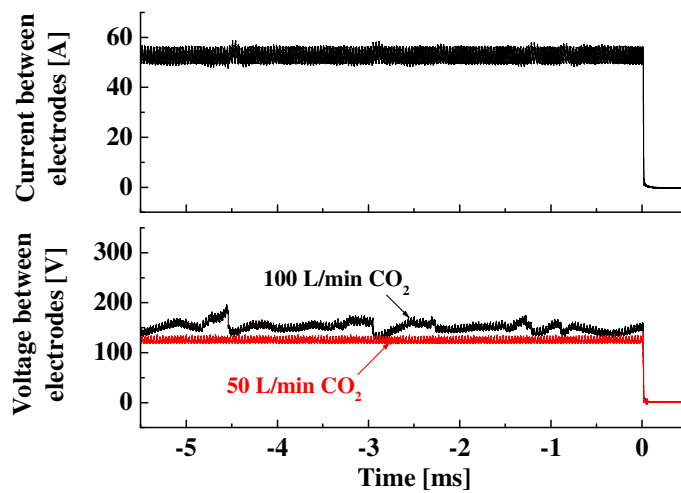
(b) CO_2

Fig. 3.10: Arc current and voltage waveforms in a steady state before the free recovery condition in (a) SF_6 and (b) CO_2 with 100 L/min and 50 L/min flow rates.
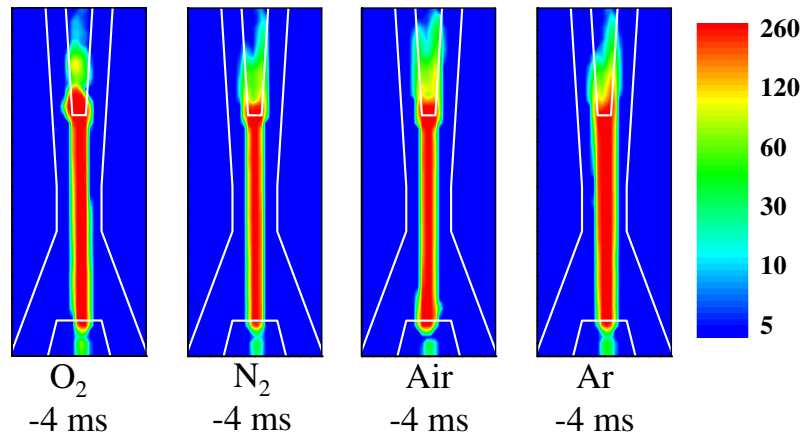
Fig. 3.11: Arc behaviour in a steady state in O_2, N_2, air and Ar with a 100 L/min flow rate (logarithmic scale colour map).
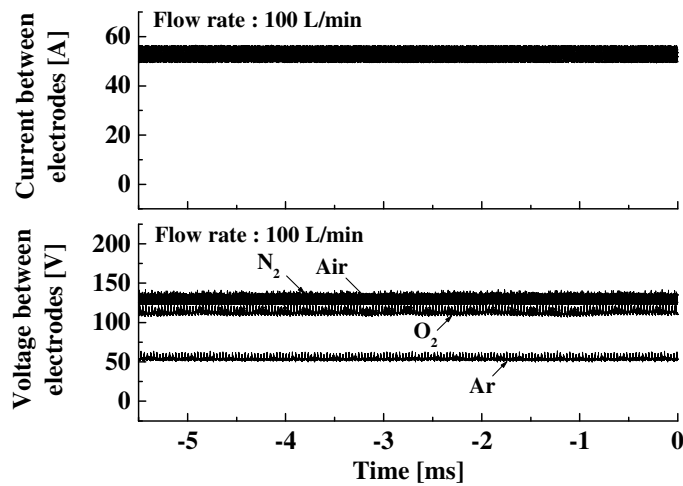
Fig. 3.12: Arc current and voltage waveforms in a steady state in O_2, N_2, air and Ar with a 100 L/min flow rate.

(a) 100 L/min SF_6
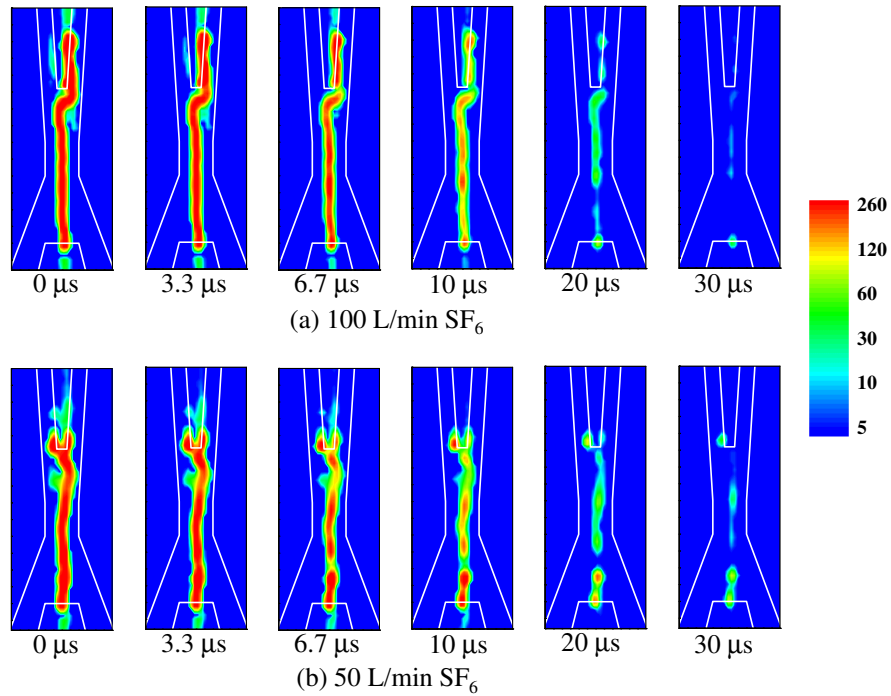
(b) 50 L/min SF_6

Fig. 3.13: Arc behaviour in decaying phase in SF_6 with 100 and 50 L/min flow rates (logarithmic scale colour map).

(a) 100 L/min CO_2
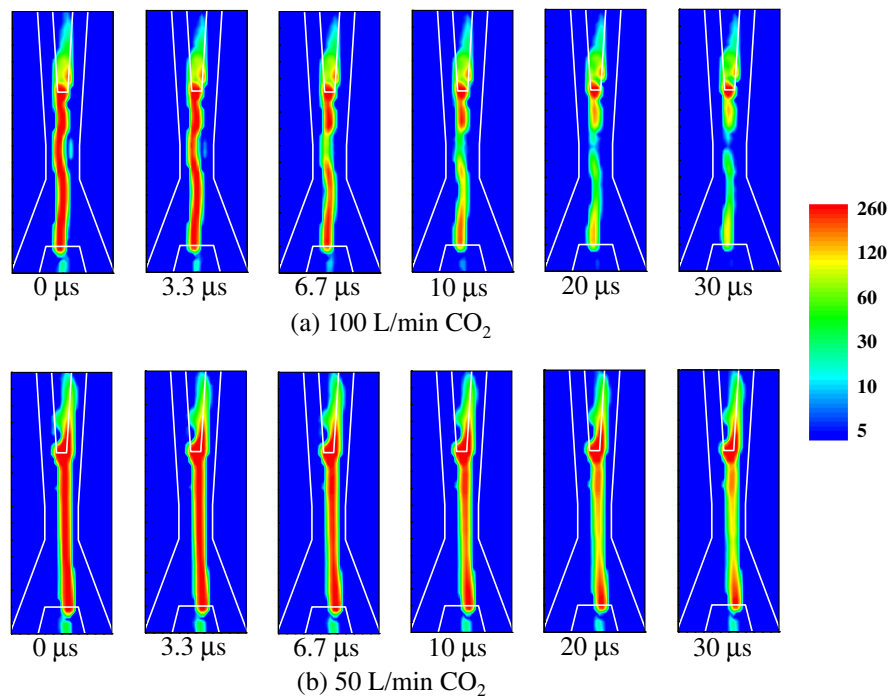
(b) 50 L/min CO_2

Fig. 3.14: Arc behaviour in decaying phase in CO_2 with a 100 or 50 L/min flow rate (logarithmic scale colour map).
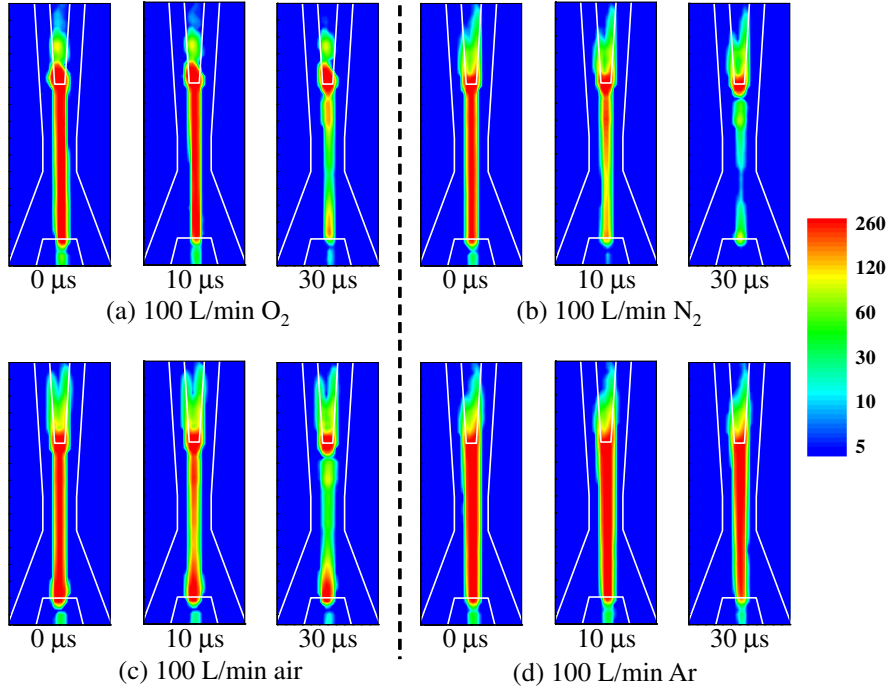
Fig. 3.15: Arc behaviour in decaying phase in O_2, N_2, air and Ar with a 100 L/min flow rate (logarithmic scale colour map).
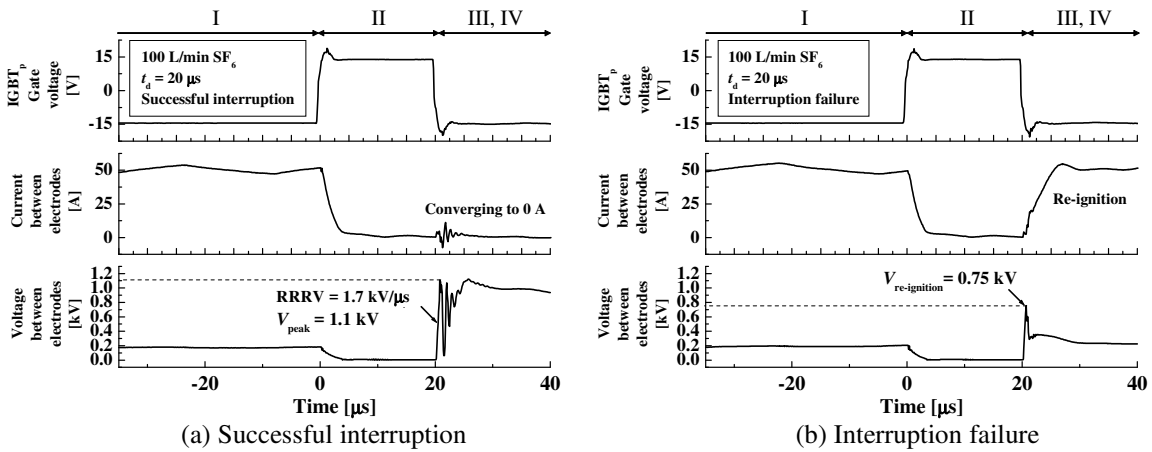
Fig. 3.16: Examples of measured current and voltage waveforms around a quasi-TRV application.
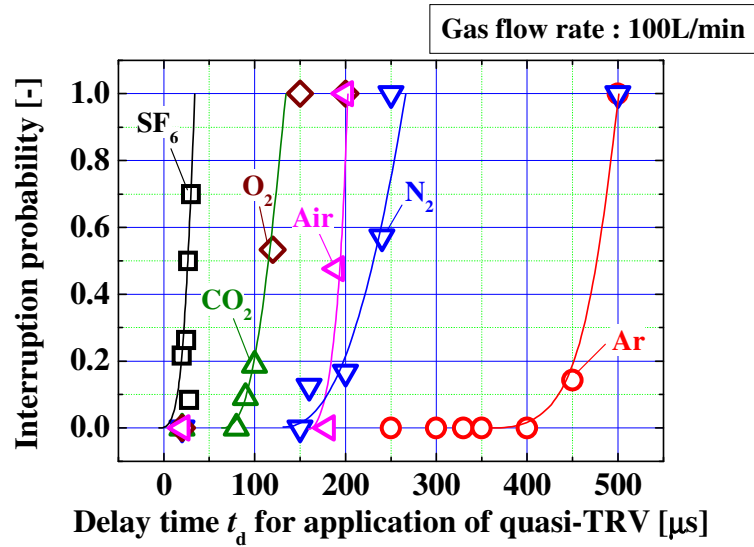
Fig. 3.17: Probability of successful interruption versus voltage application delay time t_d for cases with a 100 L/min gas flow rate.
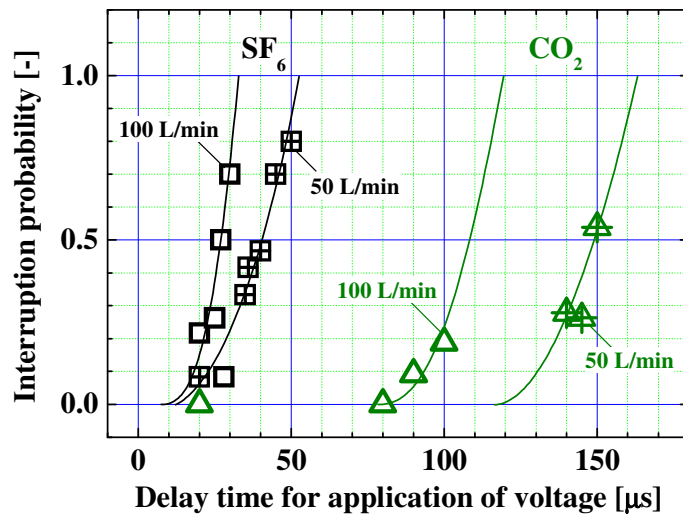
Fig. 3.18: Probability of successful interruption versus voltage application delay time t_d for the cases of SF_6 and CO_2 at 50 and 100 L/min flow rates.
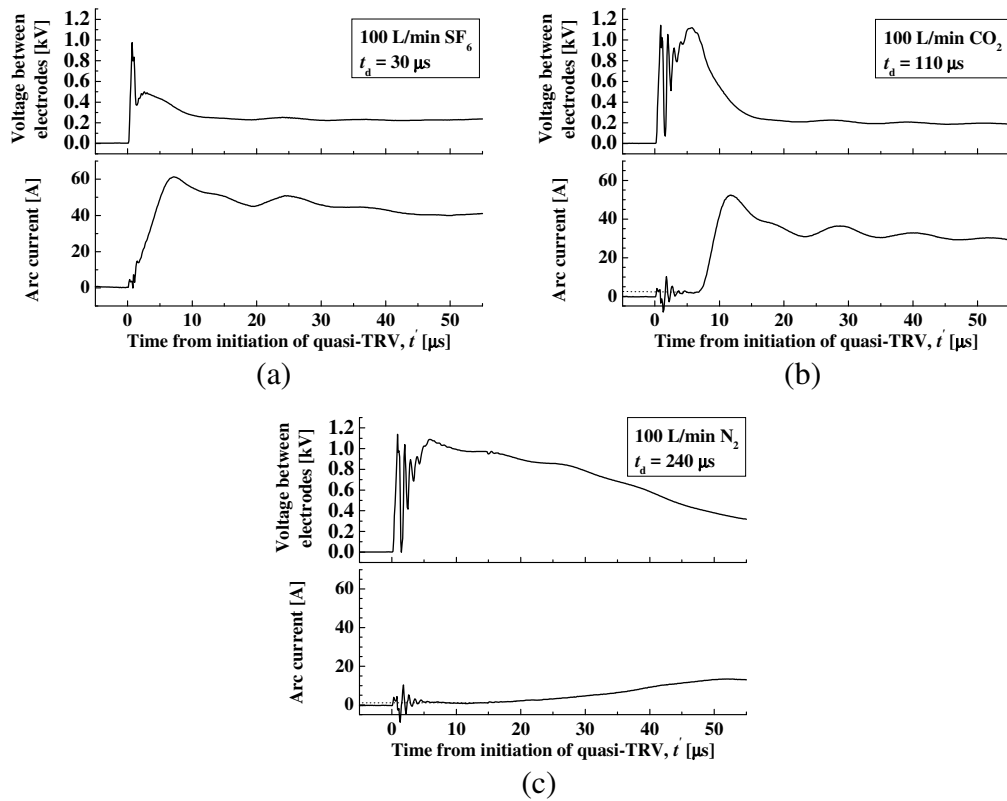
Fig. 3.19: Waveforms of current and voltage on interruption failure for SF_6, CO_2, and N_2 at a 100 L/min flow rate.
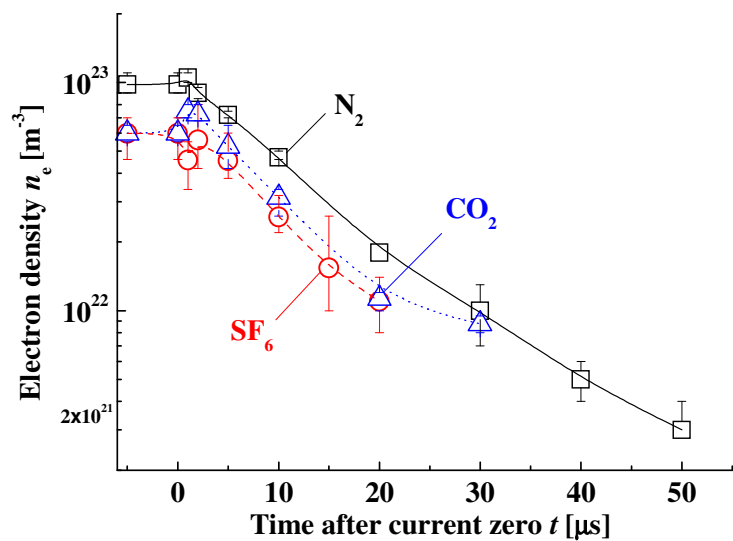
Fig. 3.20: Time evolution in the electron density in SF_6, CO_2 and N_2 arcs after current reduction to zero.
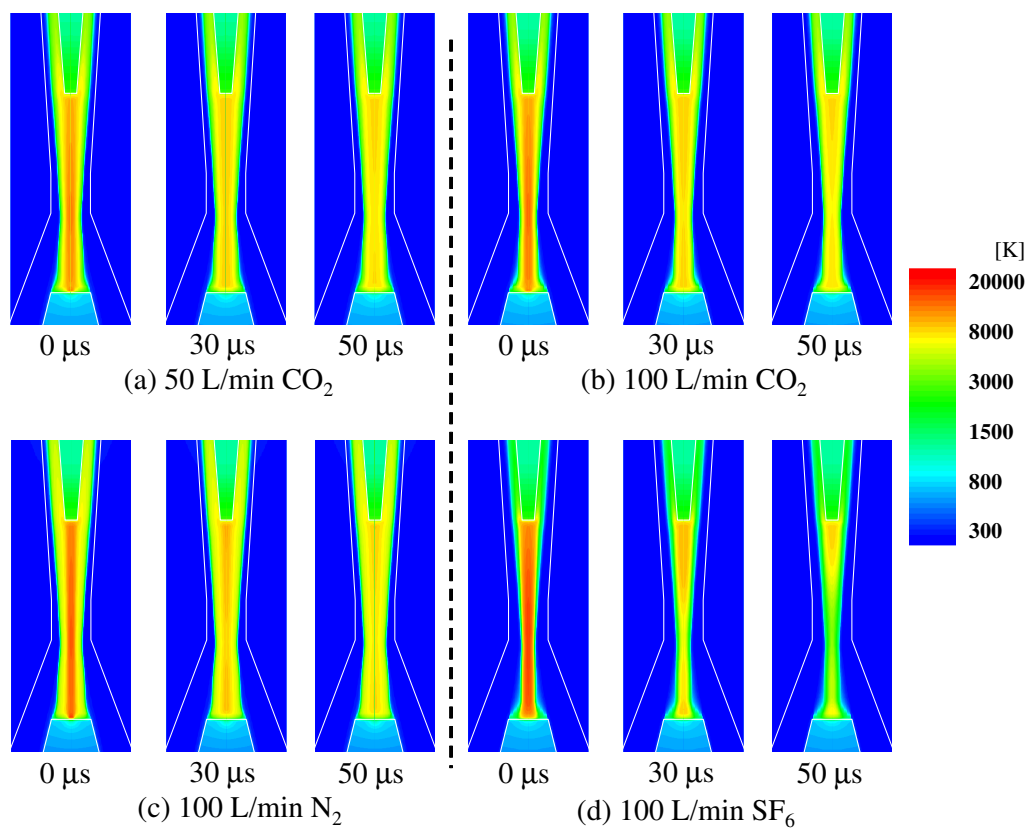
Fig. 3.21: Simulated time variation of the two-dimensional temperature distribution of CO_2, N_2 and SF_6 arcs in the decaying process.
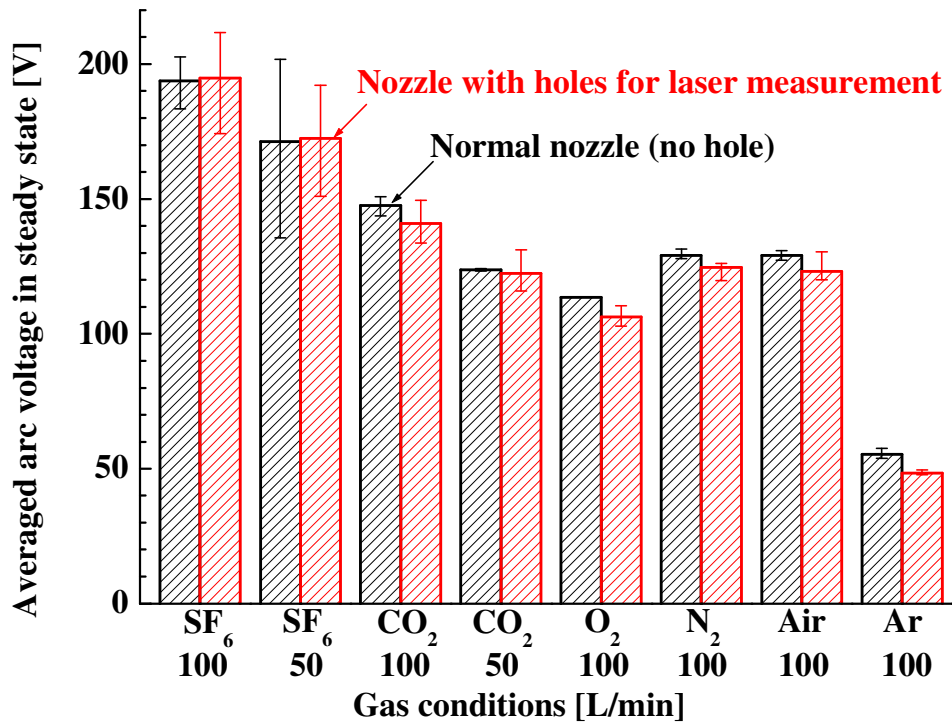
Fig. 3.22: Averaged arc voltage in a steady state in various gas conditions.

References

[1] Cressault Y, Connord V, Hingana H, Teulet P and Gleizes A 2011 Transport properties of CF_3I thermal plasmas mixed with CO_2, air or N_2 as an alternative to SF_6 plasmas in high-voltage circuit breakers *J. Phys. D: Appl. Phys.* **44** 495202 (22pp)

[2] Wang W, Rong M, Wu Y and Yan J D 2014 Fundamental properties of high-temperature SF_6 mixed with CO2 as a replacement for SF_6 in high-voltage circuit breakers *J. Phys. D: Appl. Phys.* **47** 255201 (16pp)

[3] Yang A, Liu Y, Sun B, Wang X, Cressault Y, Zhong L, Rong M, Wu Y and Niu C 2015 Thermodynamic properties and transport coefficients of high-temperature CO_2 thermal plasmas mixed with C_2F_4 *J. Phys. D: Appl. Phys.* **48** 495202 (25pp)

[4] Sun Hao, Rong M, Wu Y, Chen Z, Yang F, Murphy A B and Zhang H 2015 Investigation on critical breakdown electric field of hot carbon dioxide for gas circuit breaker applications *J. Phys. D: Appl. Phys.* **48** 055201 (16pp)

[5] Kieffel Y, Biquez F and Ponchon P 2015 Alternative gas to SF_6 for use in high voltage switchgears: g^3 *23*$^{\text{rd}}$ *International Conference on Electricity Distribution* Paper0230

[6] Hyrenbach M, Hintzen T, Müller and Owens J 2015 Alternative gas insulation in medium-voltage switchgear *Proc. 23*$^{\text{rd}}$ *Int. Conf. on Electricity Distribution*, paper0587

[7] Murai K, Nakano T, Tanaka Y, Uesugi Y, Ishijima T, Tomita K, Suzuki K, Iijima T and Shinkai T 2016 The LTE thermofluid simulation of Ar/SF_6 gas-blast arcs in a nozzle space in an arc device *IEEJ Trans. PE* **136**(9) pp.741-748

[8] Sun H, Tanaka Y, Tomita K, Wu Y, Rong M, Uesugi Y and Ishijima T 2015 Computational non-chemically equilibrium model on the current zero simulation in a model N_2 circuit breaker under the free recovery condition *J. Phys. D: Appl. Phys.* **49** 055204 (17pp)

[9] Kamimae R, Tanaka Y, Uesugi Y, Ishijima T and Shinkai T 2012 Observation of decaying arc behaviors in Ar and Ar/SF_6 gas confined in a nozzle using a high speed video camera *Joint Conference of IWHV 2012 & JK 2012 on ED & HVE* ED-12-147, SP-12-074, HV-12-077

[10] Tomita K, Gojima D, Nagai K, Uchino K, Kamimae R, Tanaka Y, Suzuki K, Iijima T, Uchii T and Shinkai T 2013 Thomson scattering diagnostics of decay processes of Ar/SF_6 gas-blast arcs confined by a nozzle *J. Phys. D: Appl. Phys.* **46** 382001 (5pp)

[11] Tomita K, Gojima D, Shimizu T, Uchino K, Nakano T, Tanaka Y, Suzuki K, Iijima T and Shinkai T 2015 Thomson scattering diagnostics of SF_6 gas-blasted arcs confined by a nozzle under free-recovery conditions *J. Phys. D: Appl. Phys.* **48** 265201 (14pp)

[12] Inada Y, Kumada A, Ikeda H, Hidaka K, Nakano T, Murai K, Tanaka Y and Shinkai T 2017 Comparative study on extinction process of gas-blasted air and CO_2 arc discharge using two-dimensional electron density imaging sensor *J. Phys. D: Appl. Phys.* **50** 175202

[13] Tanaka Y, Nakano T, Shimizu T, Tomita K and Fujino T and Suzuki K 2015 Fundamental Investigation Technique on Gas-Blast Arc Behaviors in Decaying Re-ignition Processes using Power Semiconductors *Trans.IEEJ* **135**(1) pp.1-8

[14] Nakano T, Murai K, Tanaka Y, Uesugi Y, Ishijima T, Shiraishi T, Shimizu T, Tomita K, Suzuki K and Shinkai T 2015 Evaluation on Current Interruption Ability of CO_2 and SF_6 using Current and Voltage Application Highly Controlled by Power Semiconductors *3rd International Conference on Electric Power Equipment - Switching Technology ICEPE-ST2015 (Busan, Korea)* GO-438

[15] Nakano T, Murai K, Tanaka Y, Uesugi Y, Ishijima T, Shiraishi T, Shimizu T, Tomita K, Suzuki K and Shinkai T 2016 Evaluation on Current Interruption Ability of Various Gases using Current and Voltage Application Highly Controlled by Power Semiconductors *21th International Conference on Gas Discharges and their Applications GD2014 (Nagoya, Japan)* A25 pp.97-100

[16] Muraoka K and Kono A 2011 Laser Thomson scattering for low-temperature plasmas *J. Phys. D: Appl. Phys.* **44** 043001 (15pp)

[17] Tanaka Y, Yamachi N, Matsumoto S, Kaneko S, Okabe S, Shibuya M 2008 Thermodynamic and Transport Properties of CO_2, CO_2-O_2, and CO_2-H_2 Mixtures at Temperatures of 300 to 30,000 K and Pressures of 0.1 to 10 MPa *Electrical Engineering in Japan* **163**(4) pp.18-29

[18] Tanaka Y, Paul K C, Sakuta T 2000 Thermodynamic and Transport Properties of N_2/O_2 Mixtures at Different Admixture Ratios *Trans.IEEJ* **120-B**(1) pp.24-30

Chapter 4

Fundamental study on thermal re-ignition process of various gas-blast arcs using voltage application highly controlled by powersemiconductors

4.1 Introduction

As mentioned before sulfur hexafluoride (SF_6) gas is widely used as an arc quenching medium for gas circuit breakers (GCB) from its high current interruption ability. However, SF_6 has a 22800-23500 times higher global warming potential (GWP) than CO_2 over 100 years [1–3]. From this reason, SF_6 emissions are strictly regulated, and it has thus been desired to reduce the amount of SF_6 use in GCBs. One idea to reduce SF_6 use is to develop alternative gases for SF_6. Some alternative candidates have been investigated to date, such as high pressure CO_2, CO_2-CF_3I, CO_2-CH_4, and N_2-H_2 [4–10]. Recently, perfluoronitrile(C4-PFN)/CO_2 mixture and perfluoroketone(C5-PFK)/CO_2/O_2 mixture etc. have been proposed as alternative candidates to SF_6 [11–17]. For these candidates, comparisons have been actively researched in current interruption ability and dielectric strength [18–21]. Another solution to reduce the amount of SF_6 use is to reduce the size of GCBs with keeping their interruption performance ability. To study current interruption abilities fundamentally, it is important to understand the dynamic behaviour of residual

arcs in various gas flow. Especially, detailed understanding of the residual arc behaviour after current zero is quite important to achieve SF_6-less or reduced-SF_6 arc quenching. For this reason, arc decaying process and also arc re-ignition phenomena have been investigated by experimental and numerical approaches [22–30]. However, there are still few fundamental researches with arc behaviour and physical parameters such as electron density in arc re-ignition process.

The author has been investigating decay and re-ignition processes of gas-blast arcs fundamentally using both numerical [31, 32] and experimental approaches [33–36], although the current level is still lower compared to the real circuit breaker situation. For the experiment, the author has developed a simple arc device, in which an arc plasma can be established between the moving electrode and the fixed electrode in the nozzle space. As a power source, a dc current source has been set up and its output current can be switched on and off with temporal-accuracy using a power semiconductor, e.g. insulated gate bipolar transistor (IGBT). Actually, the use of IGBT can control the arc current injection and voltage application to the arc accurately within a microsecond. Using this technique with IGBT switching, steep voltage can be intentionally applied to decaying arcs. The author calls this applied voltage the quasi-transient recovery voltage (quasi-TRV) here because it is different but similar to a regular TRV. The application of quasi-TRV with time accuracy can cause a thermally arc re-ignition intentionally. In our previous work, the author investigated interruption capability in various gas flow [33–36]. In addition, adoption of this time-accurate control of the current switching enabled us to measure the electron density in the arcs around current zero and under free recovery conditions in various gas flow using laser Thomson scattering (LTS) [37, 38] and Shack–Hartmann type laser wavefront sensors [39].

In this work, the author investigated both decaying processes and re-ignition processes of gas-blast arcs fundamentally from the electrical and optical approaches for arcs and the electron density measurement. First of all, the quasi-TRV application tests were done to decaying arcs in SF_6, CO_2, N_2, O_2, air and Ar flow with a specified delay time t_d=20 μs after initiation of the arc decaying. In these tests, the quasi-TRV was applied with time accuracy by an IGBT connected in parallel to the arcing electrodes. The timing 20 μs is a critical point for re-ignition of a SF_6-blast arc, and thus the application of the quasi-

TRV causes arc re-ignition. During these tests, the author observed arc re-ignition aspect by a high speed video camera observation. In addition to this, the electron density at the nozzle throat was measured using LTS both in decaying and re-ignition processes. Through our tests, the initial dielectric recovery properties of SF_6, CO_2, air and Ar-blast arcs were fundamentally obtained under the same condition in the same device except gas kinds. It was found that re-ignition voltage of SF_6-blast arc rapidly increased from 20 μs after initiation of the arc decaying. Such the above fundamental data both in decaying phase and re-ignition phase were successfully obtained for different gas kinds flow under the same condition in the same device. From these results, fundamental data can be provided on the thermal re-ignition processes of arc discharges in various gas flow even though in low current cases.

4.2   Experimental setup and procedure

4.2.1   Experimental circuit and the arc device

Figure 4.1 shows the diagram of the experimental circuit and the arc device used in this work. The experimental circuit is composed of mainly two parts; the IGBT-SG (Insulated Gate Bipolar Transistor - Steady state current Generator) part, and the IGBT-IG (Insulated Gate Bipolar Transistor - Impulse Generator) part. Each part will be described in the following sections.

4.2.1.1   Arc device, gas-blast nozzle and electrodes

Figure 4.2 represents schematics of the experimental arc device, which is the same to the one in our previous work [36]. The arc device consists of a vacuum chamber, a moving electrode and a fixed electrode, and a nozzle for gas flow. The outer diameter of the chamber is 200 mm. The upper electrode is the moving anode, which is driven by a compressed air cylinder. The lower electrode is the fixed cathode. Around these electrodes, a gas-blast nozzle is located.

Figure 4.3 represents (a) a schematic diagram of the nozzle and the electrodes, and (b) a photograph of the nozzle made of transparent polymethylmethacrylate (PMMA) [36]. The
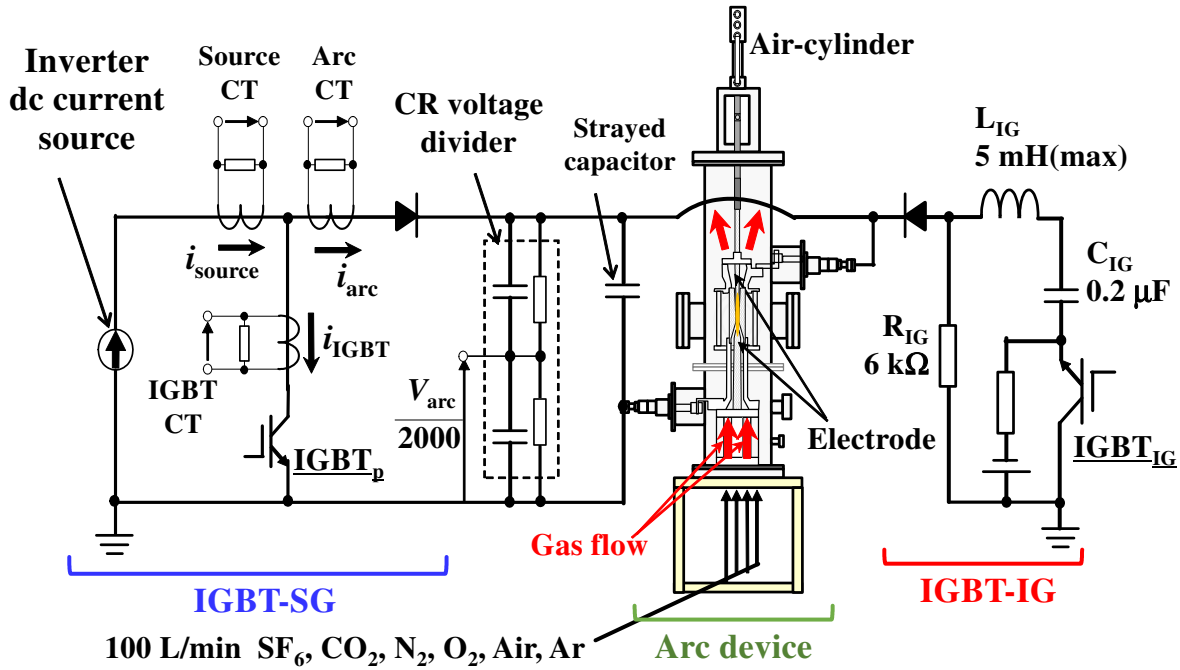
Fig. 4.1: Experimental circuit and arc device.

electrode tips are made of copper tungsten (70%Cu-30%W). The moving electrode has 6 mm body diameter and 3 mm tip diameter. The body diameter and the tip diameter of the fixed electrodes are, respectively, 20 mm and 10 mm. The gap length is 50 mm at a full open position. These electrodes are surrounded by the gas-blast nozzle that can blow introduced gas to the arc ignited between the electrodes. The diameter of the gas inlet is 40 mm, and that of the outlet is 18.8 mm. This nozzle has a throat with 10 mm diameter and 10 mm length. The author used nozzles made of polytetrafluoroethylene (PTFE) for arc tests. Only for observation of arc behaviour in the nozzle, a nozzle made of transparent PMMA was used. There are almost no difference in arc current and arc voltage with PTFE and PMMA nozzles, which indicates little influence of PTFE and PMMA on the arc behavior.

4.2.1.2   Functions of IGBT-SG part

The IGBT-SG (Insulated Gate Bipolar Transistor- Steady state current Generator) part consists of a dc current source and an IGBT element connected in parallel with the electrodes of the arc device, named IGBT$_p$, as indicated in figure 4.1. The dc current source
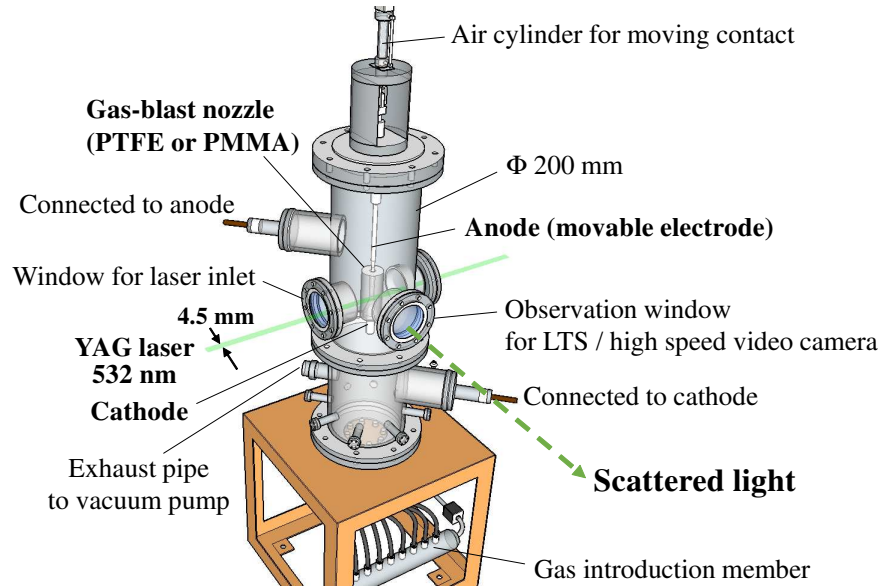
Fig. 4.2: Experimental arc device.
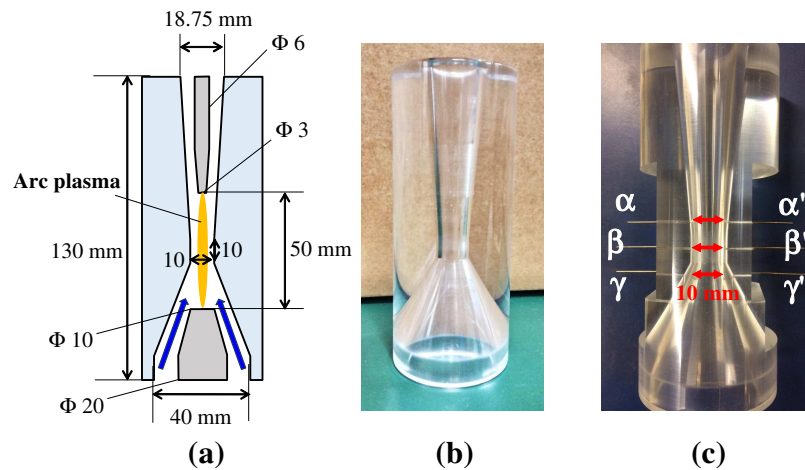
Fig. 4.3: Schematic diagram of a gas-blast nozzle and a photograph of a PMMA transparent nozzle.

is an inverter type dc power supply rated at 150 A and 250 V. This dc current source is connected in series to the arc device. The IGBT-SG part can be used for an initial arc ignition, arc sustenance, and then arc decaying in a free recovery condition. During an arc ignition and sustenance, $IGBT_p$ is in "off" state, which corresponds to non-conductive state. Thus, all the current from the dc current source flows toward the arc. If the $IGBT_p$ is switched "on" during the arc burning, the current flowing along the arc is commutated to the $IGBT_p$ because the impedance of the $IGBT_p$ becomes much lower than that of the arcs ignited in the arc device. In this situation, the current and voltage between the electrodes rapidly turn into nearly 0 A and 0 V, respectively. In this way, decaying arcs under so-called free recovery conditions can be obtained. In addition to this, during the free recovery condition, switching-"off" the $IGBT_p$ with a certain delay time t_d after initiation of arc decaying gives application of the source voltage to this decaying arc. At this time, a steep voltage appears between the electrodes depending on the transition speed of $IGBT_p$ from in conductive state to in non-conductive state and also the decaying speed in the electrical conductivity of the residual arc between the electrodes. In other words, IGBT-SG can be used for voltage application to the decaying arc as well. This voltage applied to the decaying arc between the electrodes is similar but different to the so-called transient recovery voltage (TRV). Thus, the author call this applied voltage "quasi-TRV", which is an artificial applied voltage to study the recovery speed of the residual arc. Figure 4.4(a) presents a prospective waveform of the quasi-TRV applied by the IGBT-SG under no arc condition between the electrodes. The vertical axis indicates voltage between the electrodes and the horizontal axis indicates time from initiation of quasi-TRV application. As seen in this figure, the prospective voltage is an oscillated voltage. At the first oscillation in the prospective voltage, a voltage reaches to a peak of 1.14 kV with a rate of rise of recovery voltage (RRRV) of 1.7 kV/μs. Such an oscillated voltage can be applied between the electrodes during the arc decaying as a quasi-TRV using this IGBT-SG. After the oscillation, the voltage becomes a almost constant of 400 V no later than 100 μs after application of the quasi-TRV. This quasi-TRV is characterized by inductance and strayed capacitance inside the circuit, the speed of the gate driving circuit, flowing current in the main circuit, etc. In this work, the authoe used a relatively low constant current of 50 A as a supplied current to the arc plasma so that the peak voltage and RRRV are almost fixed at a constant value

of 1.14 kV and constant value of 1.7 kV/μs for every shots. Although this peak voltage of 1.14 kV is quite lower than regular TRV or experimental voltage for some reported papers for actual circuit breakers, it is enough high voltage to cause thermally arc re-ignition with a short t_d after initiation of arc decaying in our arc device. Therefore, the time accurate application of quasi-TRV with a constant RRRV is rather important than peak voltage.

Using the system, the author evaluated fundamental arc quenching characteristics of various gases in decaying phase from our previous works [33, 36]. Additionally, the present study also deals with dynamic behaviour of intentionally pre- and post- reignited gas-blast arcs using quasi-TRV application. Especially re-ignition processes are treated in the present paper.

4.2.1.3   Function of IGBT-IG

As mentioned before, the IGBT-SG is used as a current source for arc plasma. Furthermore, it is also used as a voltage source for quasi-TRV application with a fixed peak voltage and a fixed RRRV. In addition to this, it is useful to study influence of different RRRVs of quasi-TRV on the thermal re-ignition of the decaying arcs. For this purpose, the author developed the IGBT-IG (Insulated Gate Bipolar Transistor - Impulse Generator) as a voltage source for quasi-TRV application with variable RRRVs with time-accuracy for voltage application as follows: The IGBT-IG is a modified Marx type impulse generator, consisting of capacitors C_{IG}, an inductance L_{IG} and resistances R_{IG}, as indicated in figure 4.1. In this IGBT-IG circuit, several IGBTs are used as switching elements. Thus, the author named this modified impulse generator as "IGBT-IG" in this paper. The use of IGBTs instead of conventional gap switches makes it possible to output the voltage from the IG to the residual arcs with a time-accuracy in a microsecond. The IGBT-IG can output the quasi-TRV with different voltage peaks and different of RRRVs by varying charge voltage in C_{IG} and replacing the L_{IG} element.

Figure 4.4(b) represents prospective waveforms of quasi-TRV with different rates of rise of of recovery voltage (RRRVs). The vertical axis in this figure indicates voltage between electrodes and the horizontal axis indicates time from initiation of quasi-TRV application. As seen, the peak voltage of 1.2 kV can be set with different RRRVs of 2.0 kV/μs, 0.7 kV/μs, 0.5 kV/μs and 0.25 kV/μs. After oscillation, all of impulse voltage waveforms converge to
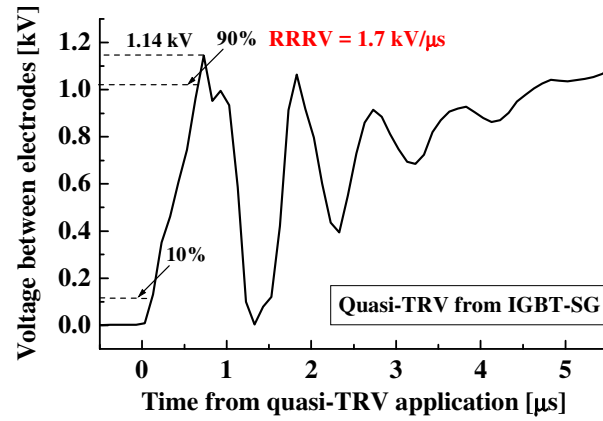
(a) IGBT-SG prospective
(Reference)
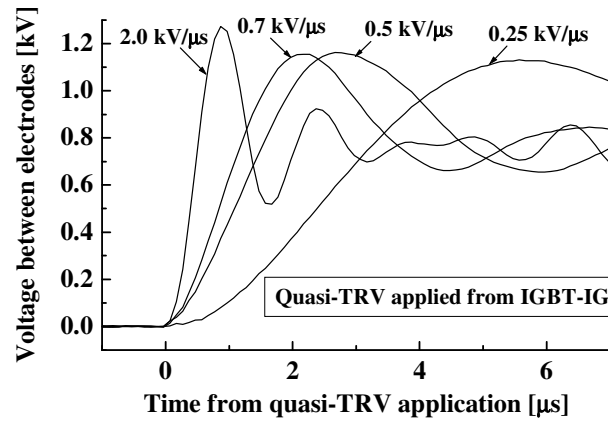
(b) RRRV variation of IGBT-IG

Fig. 4.4: The waveform of prospective quasi-transient recovery voltage (quasi-TRV) applied from IGBT-SG and IGBT-IG.

0 V in hundreds of micro seconds. In the present work in this paper, this oscillated impulse voltage was also applied to the residual arcs as a quasi-TRV to investigate initial dielectric recovery properties of gas-blast arcs.

Another use of the IGBT-IG is to apply high voltage between other three perpendicular electrode pairs indicated in figure 4.3(c). This voltage application to these three perpendicular electrode pairs by this IGBT-IG was used to detect the axial dependence of the dielectric recovery process. The details of this voltage application will be described in later section 4.4.2.

4.2.2 Experimental arrangements for Laser Thomson scattering method

To study the electron density variation in residual arcs in decaying phase and arc re-ignition phase, Laser Thomson scattering (LTS) method was utilized. The LTS is widely adopted to measure electron density in arc plasmas precisely without local thermodynamic equilibrium (LTE) assumption. The author group has already measured temporal variations in electron density in decaying arcs in various gas flows [37]. This time, the author deals with the electron density variation in the arc re-ignition process.

For LTS measurement, the second harmonic of an Nd:YAG laser at a wavelength of 532 nm was used. The pulse width of the laser beam was 10 ns. The laser energy was 200 mJ. Using this, the author measured the electron density around the nozzle throat. The reason of targeting the nozzle throat is because the electron density in the arc near the nozzle throat is a key physical parameter to ascertain arc extinction phenomena, as mentioned in literatures [37]and [39]. Figure 4.5 shows the photo and the cross sections of the PTFE nozzle for LTS measurement. This PTFE nozzle has a hole with 3.5 mm × 3 mm and a hole 10 mm × 3 mm for LTS measurement. These holes are located at the nozzle throat at a height of 28 mm from the lower electrode surface. These two holes are arranged in a horizontal direction and are mutually perpendicular. The smaller hole is for the incident laser beam path. The larger hole is for observation of 90º scattered laser light. The laser beam has a focused spot diameter of less than 0.5 mm originally. This laser beam size is spread intentionally in the horizontal direction using a cylindrical lens to have 4.5 mm width. The horizontally spread laser beam is used because the laser beam can be irradiated to the arc column even if the arc axis is shifted from the nozzle axis. The arc plasmas in SF_6 or CO_2 flow are well known to be unstable and to fluctuate [36, 40]. The larger hole was covered with glass plates to prevent hot gas ejection from the holes. The covering hole by glass plates is expected to reduce influences of the hole on the arc behaviours.

4.2.3 Experimental conditions and experimental procedure

The author used gases SF_6, CO_2, O_2, N_2, air, and Ar with a 100 L/min flow rate. This gas flow rate corresponds to a gas flow velocity of about 1.77 m/s at the gas inlet. The
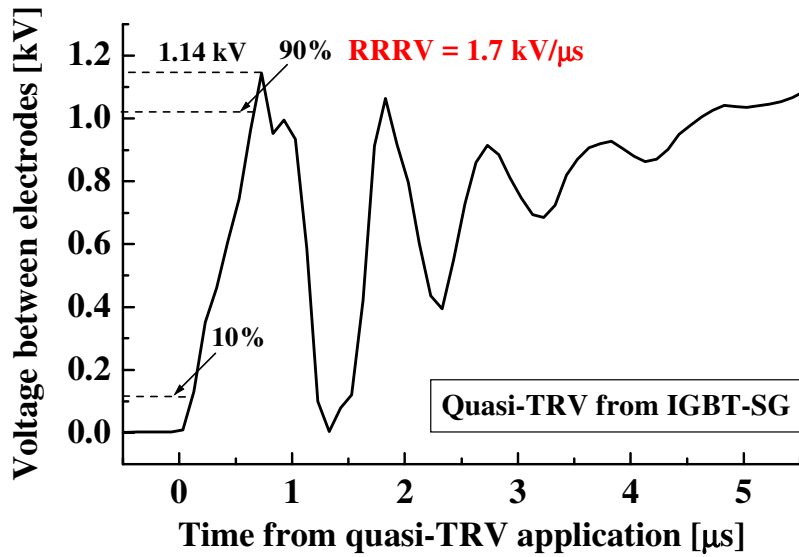
(a) IGBT-SG prospective
(Reference)
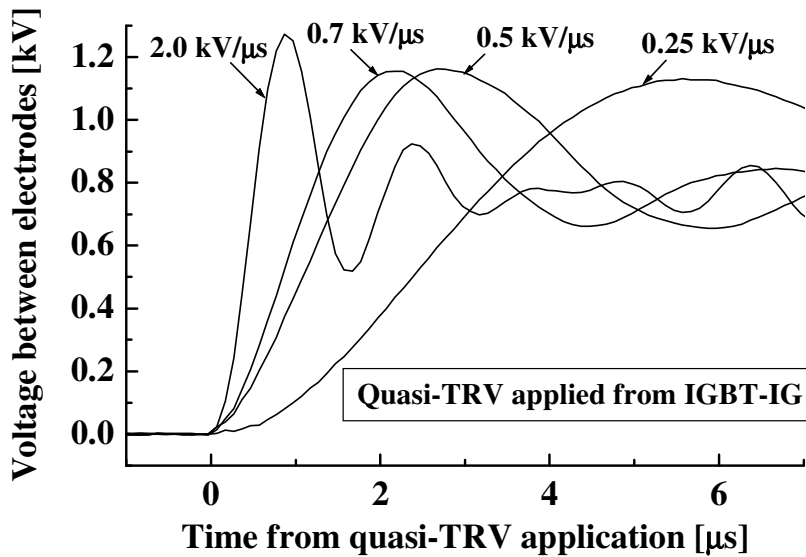
(b) RRRV variation of IGBT-IG

Fig. 4.5: PTFE nozzle for electron density measurement using laser Thomson scattering (LTS): (a) photograph of the PTFE nozzle from both sides, (b) top view of the cross section of the nozzle, (c) view from the laser inlet side, and (d) view from the observation side.

electric arc current was fixed at dc 50 A. The pressure inside the chamber and the nozzle at the initiation of an arc discharge was set to 0.1 MPa. The arc behaviour was observed using a high-speed video camera. Its frame rate was set to 300 000 frames/s. The exposure time was 1.0 μs. The PMMA nozzle was used only for the high-speed video camera observation. In other experiments, the PTFE nozzle with holes shown in figure 4.5 was used. Through the all experiments, the author measured the arc current, the IGBT current, the source current, and the voltage between the electrodes.

Figure 4.6 presents conceptual waveforms of the measured current and voltage through one experiment. The experimental procedure is as follows:

1. Before the experiment, the electrode is closed by supplying ac 100 V of the electrode driving voltage, as shown in panel (f). The IGBT$_p$ is in off state by application of the gate voltage of -15 V as shown in panel (e).

2. The chamber of the arc device is evacuated using a vacuum pump to reduce the pressure inside the chamber to about 50 Pa. After evacuation, the valve between the chamber and the vacuum pump is closed.

3. Gas is supplied from the lower part of the chamber at the specified inlet flow velocity of 1.77 m/s (= the gas flow rate of 100 L/min).

4. When the pressure inside the chamber becomes close to 0.1 MPa, the source current of 50 A is fed to the closed electrodes.

5. During the current of 50 A flows between the closed electrodes, the upper electrode starts to open by zero application of the electrode driving voltage as indicated in panel (f). It takes about 80 ms for the moving electrode to travel for its full opening stroke. By opening the electrode, the arc discharge is formed between the electrodes. The arc voltage is increased with the stroke.

6. After the electrode opens, the arc discharge is sustained at 50 A between the electrodes. In this case, the arc voltage becomes almost constant. This state is sustained for 50 ms.

7. At the time $t=0$ s, the IGBT$_p$ is switched-on to commutate the source current from the arc discharge to the IGBT$_p$. As a result, the arc current and arc voltage between

the electrodes decline to 0 A and 0 V, respectively. This is the so-called free recovery condition.

8. At the timing after a given delay time t_d from the IGBT$_p$ switching-on, quasi-TRV is applied between the electrodes using IGBT-SG or IGBT-IG. If we use the IGBT-SG, the quasi-TRV is applied by switching off the IGBT$_p$. If we use the IGBT-IG, the quasi-TRV is applied by switching on the IGBT$_{IG}$. The quasi-TRV application may cause an arc re-ignition between the electrodes.

   For experiments of detection of slow recovering position as described in section 4.4.2, high voltage is applied to the electrodes at positions $\alpha - \alpha'$, $\beta - \beta'$ and $\gamma - \gamma'$ shown in figure 4.3(c) using the IGBT-IG.

9. The current source is turned off to finish the experiment.

This procedure allows us to obtain a sequence of "arcs in steady state", "decaying arcs under free recovery conditions" and "re-igniting arcs by the quasi-TRV application" in the gas-blast nozzle. In this work, arc behaviour in decaying and re-igniting phases was observed with a high speed video camera. In addition, arc re-ignition voltage was measured. Furthermore, the electron densities in the arc in decaying phase and re-ignition phase at the nozzle throat were measured using LTS method. It should be noted that the arc current of 50 A and applied voltage as quasi-TRV are quite lower compared to those under the actual circuit breaker condition. Nevertheless, the systematic data using this well-controlled system will be useful to fundamentally understand the arc decaying process and re-ignition process of the residual arcs under gas flow of different gas kinds at the same condition.

4.3   Experimental results

4.3.1   Current and voltage of decaying and re-igniting gas-blast arcs

Figure 4.7 depicts examples of measured current and voltage waveforms of arc discharges in decaying and re-igniting phases in different kind gas flow. The gas inlet velocity was 1.77 m/s, which corresponds to the flow rate of 100 L/min. The horizontal axis indicates

(a) Photograph   **(b) Top view**

(c) Side view 1   **(d) Side view 2**
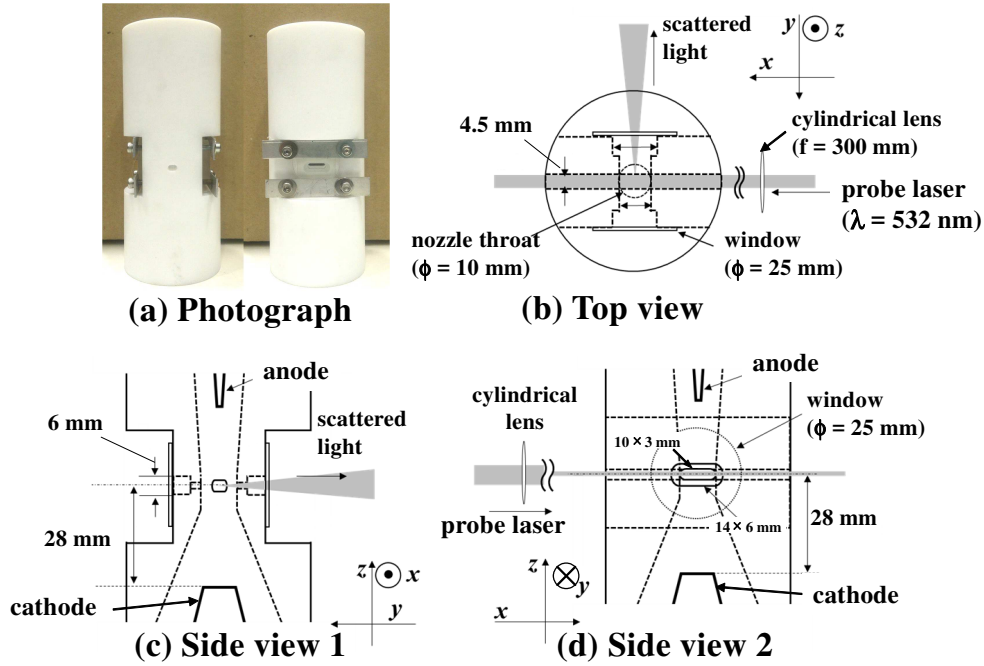
Fig. 4.6: Conceptual waveforms of measured current and voltage through one experimental shot.

time from initiation of the arc decaying $t=0$ μs. The measured arc current and voltage in transitions to free recovery condition and to re-ignition arcs are influenced by a fundamental characteristics of gas kinds related to temporal change in arc resistance and recovery feature, as described later.

As seen in this figure, the current and voltage of the arc decay from $t=0$ μs with time, leading to the free recovery condition. This decay rate of the current is dependent on the gas kind because the current commutation from the arc discharge to the $IGBT_p$ is conducted with a relation between the arc resistance and the on-resistance of $IGBT_p$. The influence of gas kind on the speed of the current commutation will be discussed later. In spite of that, all the arc discharges in different gas flow decay with time in the free recovery condition. At $t=20$ μs, a quasi-TRV with a RRRV of 1.7 kV/μs was intentionally applied between the electrodes in this case. The timing of 20 μs for application of quasi-TRV, which corresponds to the delay time $t_d=20$ μs, was selected to cause intentional arc re-ignition for any gases in this work. The timing of 20μs for quasi-TRV application is a critical delay time in SF_6 gas flow from the successful interruption or interruption failure according to our previous work [33]. In this case of short delay time $t_d = 20$ μs, the space between the

electrodes under the free recovery condition would not recover enough to withstand the quasi-TRV application. In other words, the arc can be re-ignited almost all tests.

Figure 4.7(a) indicates the waveforms of the arc current and arc voltage in SF_6 gas flow. Before decaying, the SF_6 arc voltage was about 0.25 kV in the arc current of about 50 A. From the time $t=0$ μs, both of the arc current and the arc voltage decreased to nearly 0 A and 0 V, respectively, in less than 3 μs. This implies that SF_6 arc has a rapid decay rate of electrical conductivity just after initiation of free recovery condition. At $t=20$ μs, quasi-TRV was applied to the decaying SF_6 arc. As a result, the arc re-ignited between the electrodes at about 0.7 kV in this case, and the arc current regained to about 50 A. This re-ignited voltage is relatively higher than others as mentioned later. This suggests that SF_6 would withstand at higher voltage in the residual arc. The arc current and arc voltage in CO_2 gas flow are indicated in figure 4.7(b). Similarly, the arc current and arc voltage in CO_2 gas flow decreased to 0 V and 0 A in 5 μs from the initiation of the arc decaying. By application of the quasi-TRV to the CO_2 residual arc, the arc re-ignition occurred at 0.35 kV. This arc re-ignition voltage was lower than that in SF_6 gas flow shown in figure 4.7(a). Figure 4.7(c) indicates the results for arcs in N_2 gas flow. In this case, the N_2 arc re-ignition voltage was measured as about 0.35 kV, which is close to that in CO_2 gas flow. As for Ar arcs, the arc current and arc voltage are different from others, as presented in figure 4.7(d). It took 15 μs to decay the arc current and voltage to 0 A and 0 V. This is due to the fact that the Ar arc discharge has a lower arc-resistance arising from its large arc diameter than other gases. Thus, the arc current in the Ar arc is slowly commutated to decay to zero ampere. By application of the quasi-TRV at $t=20$ μs, the arc easily re-ignited at about 0.1 kV, which was much lower value than others here. This suggests that Ar arc much slowly decays and is quite easily re-ignited.

From many arc re-ignition tests, the author evaluated the averaged arc re-ignition voltage for different gases. Figure 4.8 indicates the averaged re-ignition voltage of different gases by quasi-TRV application with RRRV of 1.7 kV/μs at a delay time $t_d=20$ μs. This figure depicts the averaged arc re-ignition voltage for 12 - 20 samples per condition. Fluctuation bars show the maximum and the minimum re-ignition voltage. As seen, the arc re-ignition voltage in SF_6 gas flow is much higher about 0.73 kV on average than the five other kinds of gas flow. This result clearly shows that SF_6 residual arc has a rapid recovery ability to

withstand quasi-TRV application. On the other hands, CO_2 and O_2 blast arcs have the similar averaged re-ignition voltage of 0.38 kV. Air had slightly lower value compared to CO_2 and N_2. Finally, the arc re-ignition voltage in Ar is much lower than the five other gases. It should be noted that the order in arc re-ignition voltage corresponds to recovery speed for withstand strength for different gases.

The author investigated the influence of RRRV in quasi-TRV on this order for different gas kinds. Figure 4.9 indicates the averaged arc re-ignition voltage in (a) SF_6, (b) CO_2 and (c) air gas flow for different RRRVs of quasi-TRV applied at t=20 μs. Each datum was derived from 10 samples of the arc re-ignition tests. The arc re-ignition voltage in SF_6 gas flow is about 0.55-0.68 kV, almost irrespective of RRRV in range of 0.25–2.0 kV/μs, although the fluctuation in arc re-ignition voltage is large as indicated by fluctuation bars. These large fluctuation bars may be due to SF_6 arcs instability in shape and low reproducibility due to turbulent effect and critical situation for arc re-ignition.

For CO_2 and air arcs, the arc re-ignition voltages are 0.33-0.36 kV and 0.34-0.35 kV, respectively, almost independent of RRRV. From the above results, we can compare these arc re-ignition voltage relatively among gas kinds under the same arc condition in the same arc device.

4.3.2   Initial dielectric recovery properties of SF_6, CO_2, air and Ar-blast arcs

Using the IGBT-SG and IGBT-IG adopted in this work, the author studied the initial dielectric recovery properties of residual arcs under free recovery condition in different gas kind flow by changing application timing of quasi-TRV (t_d). It should be noted that the initial dielectric recovery properties for different gas kinds measured here are the ones obtained under the same condition with the well-controlled system.

Figure 4.10 shows the initial dielectric recovery properties of SF_6 and CO_2-blast arcs in panel (a), and those of CO_2, air and Ar-blast arcs in panel (b). The tests were conducted using quasi-TRV with a RRRV of 2.0 kV/μs. The horizontal axis indicates the timing t from initiation of the arc decaying. From panel (a), the dielectric strength of SF_6 residual arc recovered extremely fast with time. At t=5 μs after from initiation of the arc decaying,
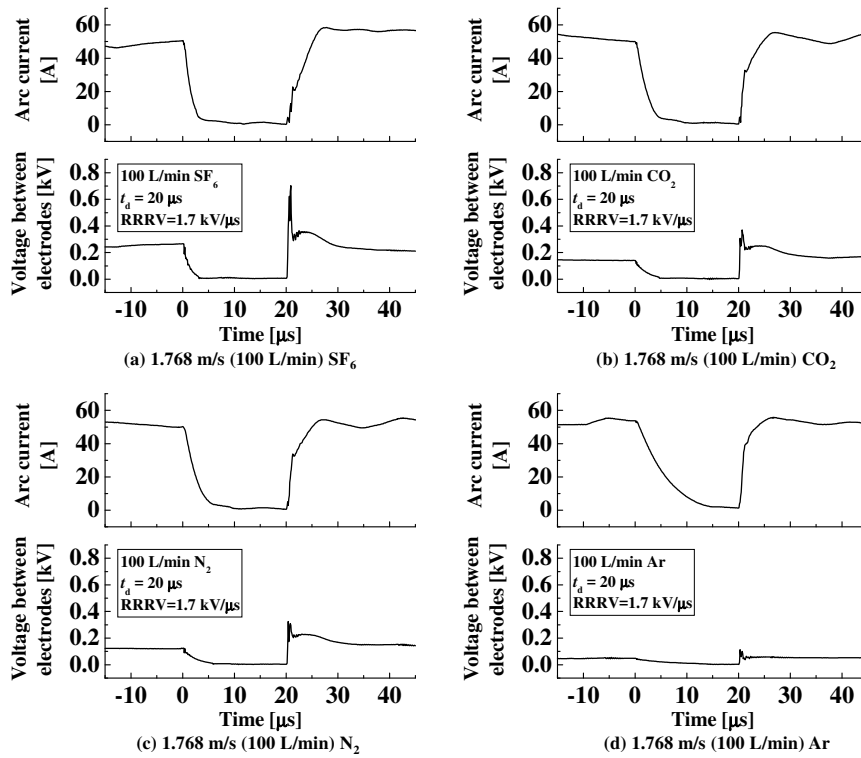
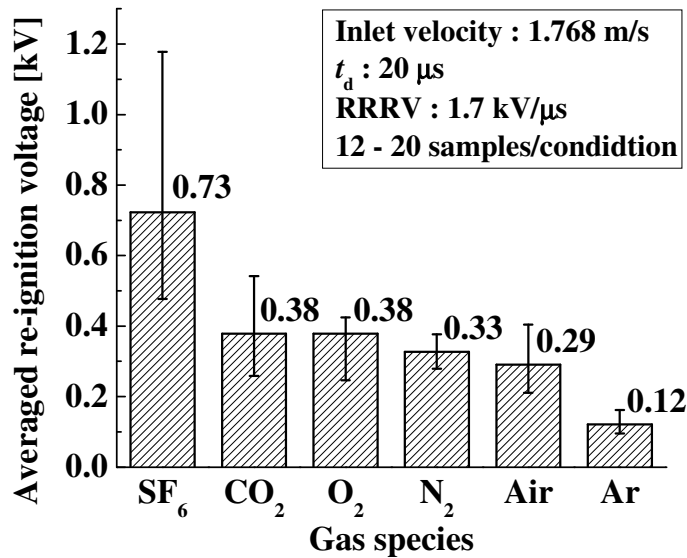Fig. 4.7: Current and voltage waveforms of each gas-blast arcs from decaying to re-igniting.

Fig. 4.8: Averaged re-ignition voltage of each gas-blast arc by quasi-TRV application from IGBT-SG with RRRV of 1.7 kV/μs.
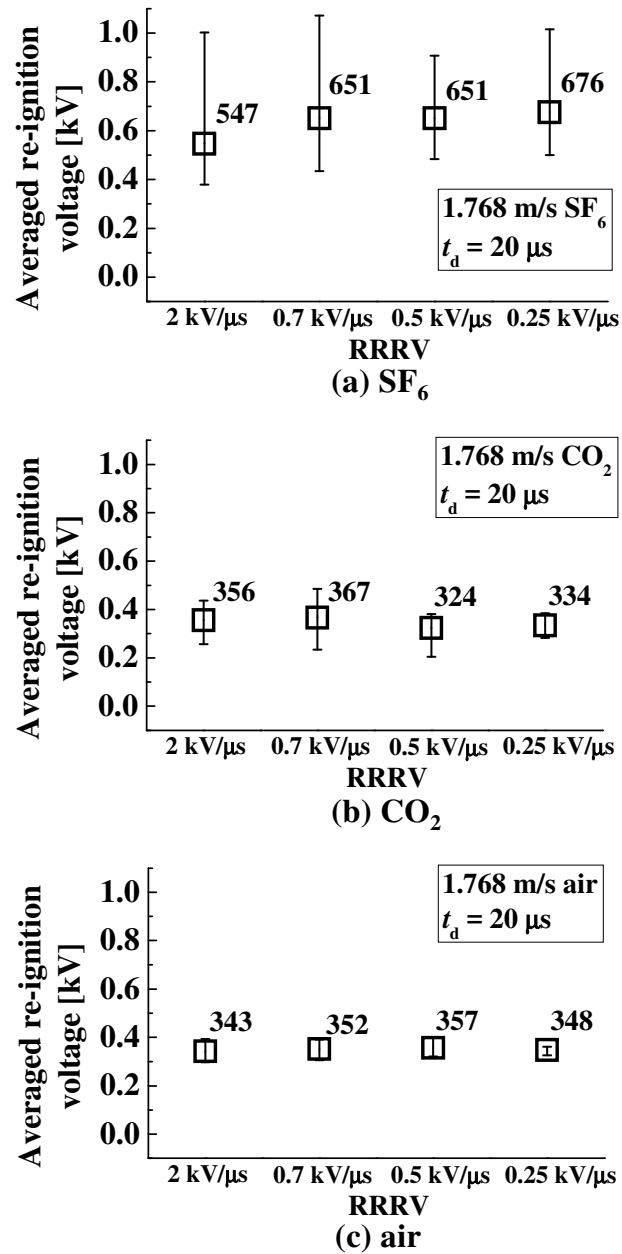
Fig. 4.9: Averaged re-ignition voltage of (a) SF_6, (b) CO_2 and (c) air blast arcs for different RRRVs.

the dielectric strength, that is, the averaged arc re-ignition voltage was obtained as 0.3 kV. This value is higher than SF_6 arc voltage in steady state. The dielectric strength of SF_6 increases with time, leading to 0.55 kV at t=20 μs. After t=20 μs, rapid rise of the arc re-ignition voltage was observed with time, and it reaches more than 0.8 kV at t=22.5 μs. We can guess from this result that the timing t=20 μs is a critical point of a SF_6 arc for thermal re-ignition. Such a fast recovery seems so important for thermal interruption success. On the other hands, CO_2-blast arcs showed a moderate speed of the dielectric recovery compared to SF_6-blast arcs. At t=20 μs, the averaged re-ignition voltage reaches 0.35 kV. Afterwards, the recovery voltage of CO_2 is almost in proportion to time till t=80 μs. From t=80 μs, the re-ignition voltage increases rapidly with time than before. The dielectric strength reaches 1.1 kV at t=90 μs.

Figure 4.10(b) represents comparison in initial dielectric recovery properties for CO_2, air and Ar-blast residual arcs. Air residual arcs have the similar re-ignition voltage around 0.3-0.35 kV at around t=10-20 μs to CO_2-blast arcs. Subsequently, the air residual arc has recovered slowly till 100 μs with time. The air residual arc also has a rapid increase in the recovery voltage after t=100 μs. On the other hand, the Ar residual arc has a distinctive properties, indicating very slow recovery with time. The above systematic test results are useful and important to discuss the dielectric recovery properties in different gases.

4.3.3   Decaying and re-igniting arc behaviours observed by the high speed video camera

Decaying process and also re-ignition process of arcs are crucial characteristics to understand the arc performance in different gas flow under the same condition in the same device. To study the decaying and re-ignition behaviour of the arcs, high-speed video observation was conducted.

Figure 4.11 depicts the sequential video pictures of radiation intensity in visible light from arcs in different gas flow. These were observed by the high speed video camera using the transparent PMMA nozzle. The profiles of the nozzle and electrodes are drawn with white lines. The radiation intensity from the arc is expressed by logarithmic scaled colour map. The red colour corresponds to high radiation intensity, and the blue shows low

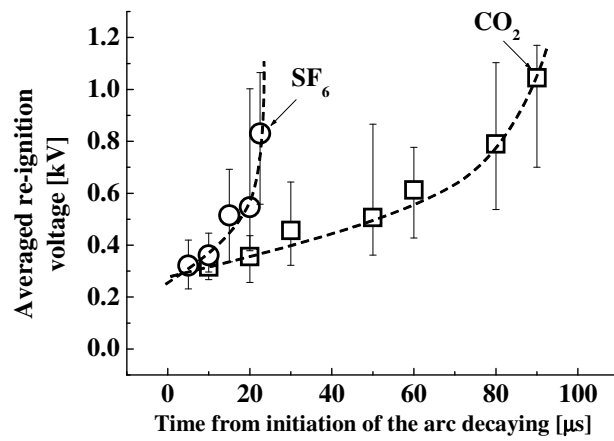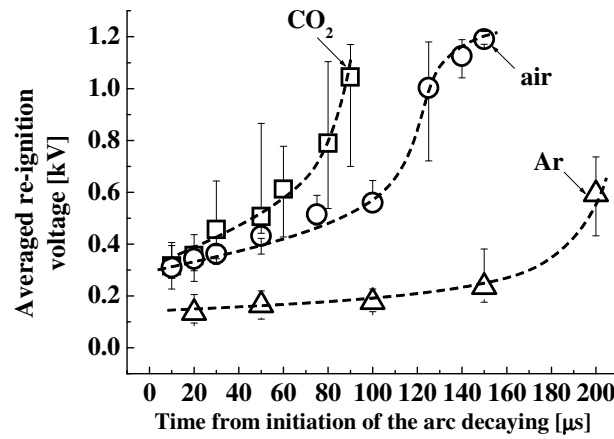Fig. 4.10: Initial dielectric recovery properties of (a) SF_6 and CO_2 (b) CO_2, air and Ar blast arcs for quasi-TRV with the RRRV of 2.0 kV/μs.

radiation intensity. Panel (a) shows the SF_6-blast arc with inlet velocity of 1.77 m/s during its decaying phase from $t=0$ μs to 20 μs, and during re-ignition phase from $t=20$ μs to 27 μs. As indicated here, from the time $t=0$ μs, the arc started decaying till $t=20$ μs rapidly. The radiation intensity from the arc discharge decays especially at the nozzle throat and downstream with time. At $t=20$ μs, the quasi-TRV was applied to this decaying arc by the IGBT-SG with a RRRV of 1.7 kV/μs. This quasi-TRV application results in the arc re-ignition in less than 1 μs after $t=20$ μs. From this reason of the arc re-ignition, the radiation intensity from the arc again increases scatteringly between the electrodes. It is interesting in this figure that the radiation intensity becomes high again around $t=23$ μs at the positions where the radiation intensity decays more between the electrodes during the free recovery condition. In other words, the higher decay area under decaying phase has higher radiation intensity in arc re-ignition phase. This is because the higher decay area has lower electrical conductivity, which results in higher electric field after the quasi-TRV application. This high electric field causes joule heating and increases the arc temperature in the arc re-ignition just there. Subsequently, at $t=27$ μs, the arc discharge in whole area between the electrodes is again formed with high radiation intensity similar to those in the steady state at $t=0$ μs. In this case, the shape of the re-ignited arc also resembles that of the arc before decay. From the above result, the arc was thermally re-ignited through the original path in this case.

Figure 4.11(b) presents the CO_2-blast arc with an inlet velocity of 1.77 m/s during arc decaying and arc re-igniting. Similarly to the panel (a), the duration from $t=0$ μs to 20 μs is the arc decaying phase, whereas the duration after $t=20$ μs is the arc re-ignition phase for CO_2 arcs. As seen in this figure, the CO_2 arc plasma decayed especially around the nozzle throat inlet, that is, at the upstream side of the throat. This result suggests that the introduced cold CO_2 gas quenched the residual arc there around the nozzle throat inlet. This may be due to the high convection loss with higher gas flow velocity by the introduced cold CO_2 gas flow there. After application of quasi-TRV at $t=20$ μs, the arc is re-ignited between the electrodes in straight shape. In this case, the higher decay region around the nozzle throat in CO_2 gas flow also has the increased radiation intensity there by arc re-ignition at $t=23$ μs. At $t=27$ μs, the thermally re-ignited arc has almost the same shape to the arc at $t=0$ μs. Figure 4.11(c) represents the air-blast arc with inlet velocity of 1.77 m/s
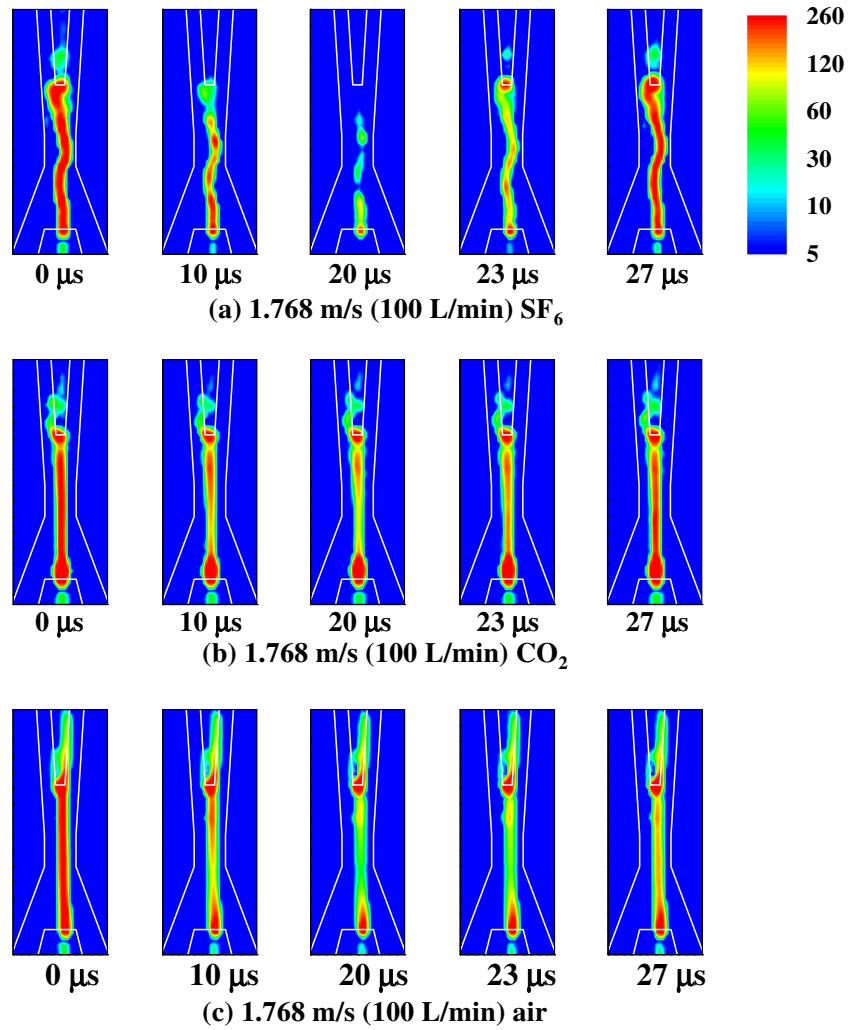
Fig. 4.11: Arc behaviour in the decaying and re-ignition phase in (a) SF_6, (b) CO_2 and (c) air gas flow with inlet velocity of 1.77 m/s (logarithmic scale colour map).

during decaying and re-igniting. The air-blast arc decayed from the more upstream side of the nozzle throat than the other gas flow. However, at $t=20$ μs, rather uniform radiation intensity distribution was observed in the residual air arc region. Just after the re-ignition at $t=20$ μs, the radiation intensity from the re-ignited arc was still weak. At $t=27$ μs, the radiation intensity from the re-ignited arc increases with time almost uniformly on the axis.

The above results indicate that the nozzle throat plays a crucial position for decaying phase and also for arc re-ignition phase for any cases. It is noteworthy that such arc re-ignition process were found under the same condition except gas kinds to study the arc quenching ability of different gases.

4.3.4   Time variation in the electron density in decaying and re-igniting phases in different gas flows

For arc quenching phenomena, the electron density is one key parameter which determines the electrical conductivity in a thermal mode and also a seed of electron avalanche in dielectric mode. On the other hand, the nozzle throat is one important position in decaying phase and re-ignition phase in residual arcs in gas flow. It is therefore crucial to understand the electron density decay around the nozzle throat in both phases.

Figure 4.12 depicts the measured electron density in the nozzle throat as indicated in figure 4.5 using the LTS method. The LTS measurement was conducted more than five times at each timing. The measurement timing was changed from t=0 μs to 30 μs. The timing t=0 μs corresponds to the timing of current commutation for free recovery condition. The vertical axis indicates the electron density, and the horizontal axis represents the time from initiation of the arc decaying. In all of the cases, the gas inlet velocity was 1.77 m/s (flow rate : 100 L/min) and the quasi-TRV was applied at the timing of t=20 μs by the IGBT-SG with a RRRV of 1.7 kV/μs. Panel (a) shows time variation in the electron density at the nozzle throat in SF$_6$ gas flow. At the time t=0 μs, the electron density was estimated as approximately 6×10^{22} m^{-3} in SF$_6$ gas. After that, the electron density decreased rapidly to 2.3×10^{22} m^{-3} at t=10 μs. This value is relatively lower than those in other gases. It was decreased to 1.4×10^{22} m^{-3} until t=20 μs. From t=20 μs to 25 μs, a significant rise in the electron density was observed in several micro seconds after the arc re-ignition. Finally, the electron density rapidly reaches to 6×10^{22} m^{-3} at t=30 μs, that is nearly equal to before the arc decaying. Such the time evolution in the electron density both in decaying phase and re-ignition phase Features of SF$_6$ residual arcs are having a little lower electron density at t=10 μs in decaying phase and large fluctuation in electron density compared to the other gas-blast arcs. Lower electron density in SF$_6$ residual arc at t=10-15 μs in decaying phase may be due to rapid decay of the arc in narrow SF$_6$ arc channel. The large fluctuation in electron density is because the SF$_6$ arc is fluctuated strongly by turbulent effect. Another feature of SF$_6$ residual arcs is that a relatively rapid increase in electron density at t=25 μs just after re-ignition. This seems to correspond to a smaller diameter of SF$_6$ arc at the re-ignition phase. As seen in figure 4.11, most part of SF$_6$ arc along the axis had been quenched rapidly at t=20 μs to have a broken shape. In

this situation, the arc would re-ignite through a narrow and short path. The arc re-ignition in a narrow and short path results in higher electron density due to high current density at re-ignition positions. Thus, these features may be related to a strong arc quenching ability of SF_6.

Figure 4.12(b) presents the electron density in CO_2 residual arcs in decaying phase and re-ignition phase. At $t=0$ μs, the CO_2 arcs have the electron densities around 6×10^{22} m^{-3}, which is similar to those in the SF_6 blast arcs. However, just after the initiation of the arc decaying $t > 0$ μs, the electron density in the CO_2-blast arc first increased to 7.5×10^{22} m^{-3} once at the nozzle throat, and then it decreased monotonously with time. At $t=10$ μs, the electron density in CO_2 arc was 3×10^{22} m^{-3}, which continued to decrease to 1×10^{22} m^{-3} at $t=20$ μs. After the arc re-ignition from $t=20$ μs, the electron density recovered to 5×10^{22} m^{-3} until $t=30$ μs. The temporal variation in the electron density in the O_2-blast arc is indicated in figure 4.12(c). In this case, the electron density was nearly 8×10^{22} m^{-3} at $t=0$ μs. The electron density in O_2-blast arc also decreased smoothly with time but slower than in CO_2 gas flow. At $t=20$ μs, the electron density reaches to 2×10^{22} m^{-3}, which is relatively higher compared to those in SF_6 and CO_2 gas flow at $t=20$ μs. After the arc re-ignition, the electron density is elevated gently around $t=20$-25 μs, and its value became to be 6×10^{22} m^{-3} at $t=30$ μs. On the other hand, the behaviour of N_2 arcs can be seen in figure 4.12(d) in terms of the electron density. The N_2 arcs have higher electron densities around 10×10^{22} m^{-3} at $t=0$ μs than the other five kinds of gases in this work. This electron density decays with time monotonously. At $t=10$ μs, it reached to 4.6×10^{22} m^{-3}. The electron density is 1.8×10^{22} m^{-3} at $t=20$ μs. This value is similar to those in SF_6 and CO_2 at $t=20$ μs. After the arc re-ignition, the electron density is elevated to 8×10^{22} m^{-3} until $t=30$ μs. Similar behaviour in the electron density can be obtained in air arcs in decaying phase and re-ignition phase, as indicated in figure 4.12(e), although the air arcs have lower electron density at $t=0$ μs. Finally, figure 4.12(f) indicates the electron density in Ar-blast arcs. The Ar-blast arc had lower electron densities around 4×10^{22} m^{-3} compared to other gas-blast arcs before the arc decaying. This is because the diameter of Ar-blast arc was much larger than other gas-blast arcs, and thus Ar arcs maintain their arc conductance without higher electron density for arc sustaining. In addition, Ar residual arcs have quite lower decay rates in the electron density than the other gases in this work.

After application of quasi-TRV, the electron density still kept decreasing despite that the arc current increases to 50 A at t=25 μs.

In these ways, the sequence of the electron density in the gas-blast arcs at the nozzle throat from its decaying phase to re-ignition phase was successfully obtained using the LTS method.

4.4   Discussions

4.4.1   Arc decay process in SF_6 gas flow compared with other gases

The experimental results in this work showed the following things.

1. Re-ignition voltage for SF_6-blast arc was higher than other gas-blast arcs for the same timing (t_d=20 μs) of quasi-TRV application.

2. Dielectric recovery in the SF_6 residual arc was several times faster than other gas-blast arcs. From t=20 μs after initiation of the arc decaying, the re-ignition voltage of SF_6-blast arcs rapidly increased and reached to approximately 0.8 kV around t=22.5 μs.

3. The radiation intensities from SF_6 residual arcs decreased in almost the whole part of the arc simultaneously in the decaying phase. On the other hand, the radiation intensity from CO_2 and air residual arcs decreased especially around near the nozzle throat.

4. After the arc re-ignition, the electron density in the SF_6 recovered faster than other gas-blast arcs in re-ignition.

As seen in the results above, the arc re-ignition process of SF_6-blast arcs was clearly different from the other gas-blast arcs. As mentioned before, the radiation intensity from a SF_6-blast arc decayed in the whole part of the arc simultaneously. This is because the gas SF_6 has a higher specific heat ρC_p and thermal conductivity κ at low temperatures of about 1800, 2000 and 2200 K, where ρ is the mass density, C_p denotes the specific heat and
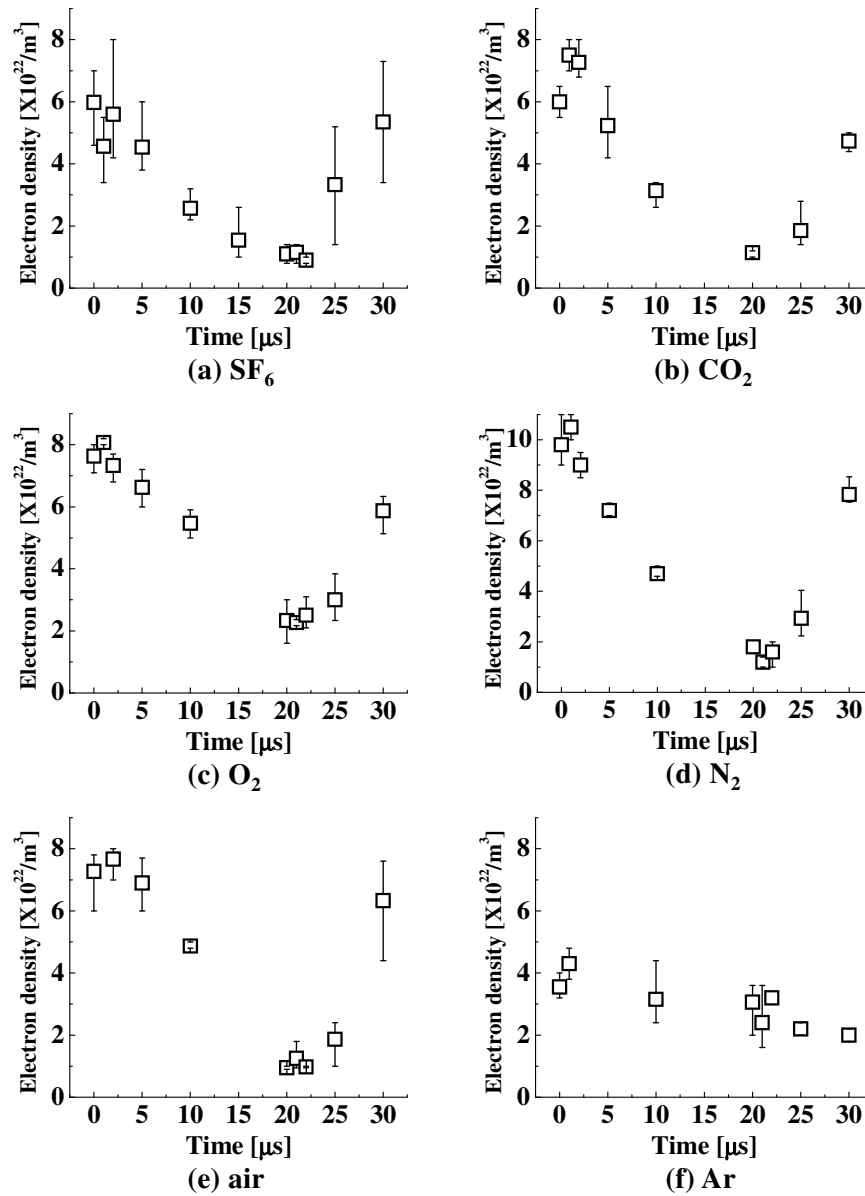
Fig. 4.12: Sequence of electron density of each gas-blast arc at the nozzle throat in the decaying and re-ignition phase in (a) SF_6, (b) CO_2, (c) O_2, (d) N_2, (e) air and (f) Ar gas flow with with inlet velocity of 1.77 m/s.

κ represents the thermal conductivity. The higher specific heat arises from dissociation-association reactions between SF_6 to SF_4, SF_4 to SF_2, and SF_2 to S and F. This ρC_p results in the higher convection loss around there. In addition, mass density of SF_6 is much higher than the other five gases, which tends to result in the turbulent in gas flow. The high ρC_p and the strong turbulent gas flow can make the arc column thinner. The thinner arc plasma is subject to decay rapidly.

4.4.2   Detection results of slow recovering position using perpendicular voltage application

As shown in the previous section, the high speed video camera observation results suggest that the nozzle throat plays an important role for both arc decaying and re-ignition phase. The speed and aspect of the dielectric recovery process may depend on the axial position in the nozzle in different gas flow. In this study, using IGBT-IG, high voltage was applied between three perpendicular electrode pairs to the arc during the arc decaying phase. The position of three electrode pairs was shown in figure 4.3(c), as designated by $\alpha - \alpha'$, $\beta - \beta'$ and $\gamma - \gamma'$. These electrode pairs are electrically independent of the arc main circuit. In other words, these electrode pairs and IGBT-IG are electrically floating, while the downstream electrode of the main circuit, which works as the cathode, was electrically grounded. The electrodes are made of tungsten and their diameter is 1.0 mm. Each pair of electrodes has a gap length of 10 mm. The axial location of $\alpha - \alpha'$ pair is at 10 mm downstream from the center of the nozzle throat. The $\beta - \beta'$ pair is located at the center of the nozzle throat. Whereas, the $\gamma - \gamma'$ pair is placed at 10 mm upstream from the center of the nozzle throat. Instead of the quasi-TRV application to the main electrode pair vertically located, a high voltage was applied simultaneously to between $\alpha - \alpha'$, between $\beta - \beta'$ and between $\gamma - \gamma'$. This high voltage application to these three electrode pairs enables us simply to study the axial dependence of the dielectric recovery process. If the dielectric recovery is slow at one of the positions, the arc is re-ignited between the perpendicular electrodes. This re-ignition arc were observed by the high speed video camera to judge the axial position of arc re-ignition. Applied voltage had a peak of more than 5 kV.

Figure 4.13(a) shows the SF_6-blast arc with inlet velocity of 1.77 m/s ignited between

the electrodes $\alpha - \alpha$'. In this case, voltage was applied to α, β and γ against α', β' and γ'. Voltage application delay time was 10 μs after initiation of the initial arc decaying. Under this condition, only one ignition was obtained at position $\alpha - \alpha'$ in three tests. This is because a SF$_6$-blast arc has small diameter and thus re-ignition is difficult to occur. In spite of that, it should be noted that the arc is ignited at position $\alpha - \alpha$', downstream from the nozzle throat. This result indicates that the dielectric property recovers more slowly at position $\alpha - \alpha'$. When the voltage was applied only between $\beta - \beta'$ and $\gamma - \gamma'$ without connection with α-α', arc ignition never occurred with the voltage application at same timing. These results suggest that the upstream position and the center position of the nozzle throat have higher dielectric withstand compared to downstream side in SF$_6$ gas flow. In this way, dielectric recovery process depends on the axial position. Nevertheless, it was found that SF$_6$-blast arcs has extremely rapid dielectric recovery compared to CO$_2$-blast arcs.

On the other hand, figure 4.13(b) shows the CO$_2$-blast arc with inlet velocity of 1.77 m/s, ignited between $\alpha - \alpha'$. In this case, voltage was applied to all positions and voltage application delay time was 90 μs. The author used longer delay time of 90μs because CO$_2$-blast arcs decreases radiation intensity more slowly than SF$_6$-blast arcs. This suggest the dielectric property recovers more slowly in CO$_2$ gas than in SF$_6$ gas. Even with this longer delay time, five ignitions were obtained in five tests. As seen in figure 4.13(b), arc re-ignition occurs at $\alpha - \alpha'$ for three cases. This means that CO$_2$ arc decays most slowly in downstream from the nozzle throat compared to the nozzle throat center and the upstream portion. Among the five tests, other two tests showed ignition between α' and γ as indicated in figure 4.13(c). This indicates that the upstream and downstream portions were weak in dielectric strength in this case. From the above results, the nozzle throat is inferred to have a rapid dielectric property than the upstream and the downstream in CO$_2$.

If we apply the high voltage between $\beta - \beta'$ and $\gamma - \gamma'$ without voltage application of $\alpha - \alpha'$, we can compare the dielectric strength of $\beta - \beta'$ and $\gamma - \gamma'$. Figure 4.13(d) and (e) shows results of perpendicular arc ignition in CO$_2$-blast arcs in cases that voltage application to only $\beta - \beta'$ and $\gamma - \gamma'$ with the same delay time of 90 μs. Five tests were done under this condition, and one ignition between $\gamma - \gamma$' was obtained. Four ignitions were between $\gamma - \beta$' or $\beta - \gamma$'. Ignition between $\beta - \beta$' was not obtained. These results
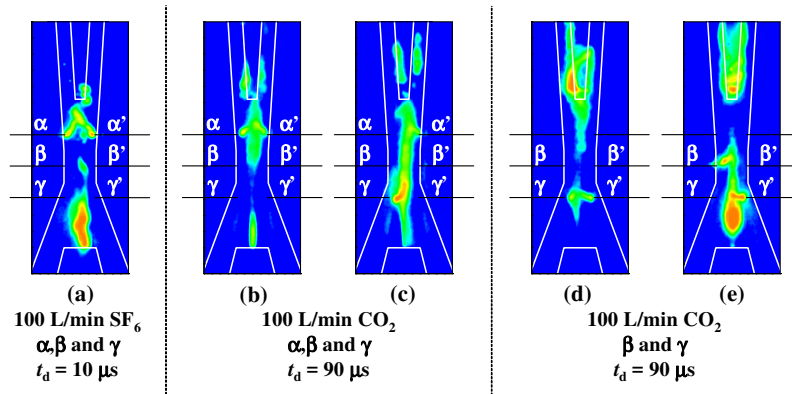
Fig. 4.13: Perpendicular arc ignition by high voltage application in SF_6-blast arc (a) and CO_2-blast arcs (b)-(e).

indicate again that center of the nozzle throat has a rapid recovering rate compared to the upstream.

4.4.3   Issues and future prospects

This paper dealt with arc current of 50 A and gas flow rate of 100 L/min, both are lower than in a practical gas circuit breaker. These conditions were chosen to facilitate arc condition as follows: Lower current was chosen to minimize erosion of the nozzle and the electrodes. The erosion and ablation of the electrode and the nozzle make the arc state complex, which is not adequate to study the influence of gas kind itself on the arc phenomena. Furthermore, lower gas flow rate was selected to reduce complex turbulent effects. Instead of those, the arc current and applied voltage were well controlled with time accuracy. Lower arc current and gas flow rate situation in the present work is quite different from the situation for practical circuit breakers. Nevertheless, it was found that nozzle throat position has significantly rapid dielectric recovery. This means the nozzle throat in this study plays a role to quench the arc more. The author believes the results obtained in this study can be used for more fundamental and precise consideration of arc decaying and re-ignition phenomena.

According to initial dielectric recovery characteristics in Fig. 4.10, there are some interesting time points other than $t=20$ μs after initiation of the arc decaying. For example, they are $t=80$ μs for CO_2-blast arcs, $t=100$ - 120 μs for air-blast arcs and $t=150$ μs for Ar-

blast arcs, at which the dielectric strength recovers rapidly. The author needs to measure the electron density, the electron temperature and their distribution in the arc precisely for elucidation of arc decaying and re-ignition phenomena in a nozzle.

4.5   Summary of chapter 4

This chapter reports fundamental re-ignition process of various gas-blast arcs. A gas-blast arc was intentionally decayed using power semiconductor by producing free recovery condition, and intentionally re-ignited by application of artificial recovery voltage called quasi-TRV. From many tests, initial dielectric recovery properties of SF_6, CO_2, air and Ar-blast arcs were obtained. Results showed that dielectric recovery of SF_6-blast arc is extremely faster than the other five gas flow in this work. It was also found that the re-ignition voltage of SF_6-blast arcs rapidly increases from 20 μs after initiation of the arc decaying. Accordingly, behaviours of various gas-blast arcs were observed during intentional re-ignition process at 20 μs after initiation of the arc decaying using a high speed video camera. Results showed that the radiation intensity in SF_6-blast arcs decreased almost simultaneously in the whole part of the arc. The other gas-blast arc column decayed especially around the nozzle throat. These results showed a clear difference in decaying phase between SF_6 and the other five gases. Finally, the electron density both in decaying phase to re-ignition phase was obtained for each gas-blast arc using laser Thomson scattering (LTS) method. It was found that electron density in the SF_6-blast arc decreases quickly during the arc decaying phase, and after the arc re-ignition the electron density rises more quickly. In this way, the author has successfully measured a sequence of electron density of the arc in the nozzle. The obtained data helps the author to consider thermally arc re-ignition process.

References

[1] IPCC 4th Assessment Report: Climate change 2007 (AR4)

[2] Glaubitz P, Stangherlin S, Biasse J M, Meyer F, Dallet M, Pruefert M, Kurte R, Saida T, Uehara K, Prieur P, Ito H, Kynast E, Janssen A, Smeets R, and Dufournet D 2014 CIGRE position paper on the application of SF$_6$ in transmission and distribution networks *Electra* **34** 274 pp.34-39

[3] IPCC 5th Assessment Report: Climate Change 2013: The Physical Science Basis

[4] Rokunohe T, Yagihashi Y, Endo F and Oomori T 2006 Fundamental Insulation Characteristics of Air, N$_2$, CO$_2$, N$_2$/O$_2$, and SF$_6$/N$_2$ Mixed Gases *Electrical Engineering in Japan* 155(3) pp.9-17

[5] Uchii T, Hoshina Y, Kawano H, Suzuki K, Nakamoto T and Toyoda M 2007 Fundamental Research on SF$_6$-free Gas Insulated Switchgear Adopting CO$_2$ Gas and Its Mixtures *Proceedings of International Symposium on EcoTopia Science 2007, ISETS07* pp.516-520

[6] Cressault Y, Connord V, Hingana H, Teulet P and Gleizes A 2011 Transport properties of CF$_3$I thermal plasmas mixed with CO$_2$, air or N$_2$ as an alternative to SF$_6$ plasmas in high-voltage circuit breakers *J. Phys. D: Appl. Phys.* **44** 495202 (22pp)

[7] Wang W, Rong M, Wu Y and Yan J D 2014 Fundamental properties of high-temperature SF$_6$ mixed with CO$_2$ as a replacement for SF$_6$ in high-voltage circuit breakers *J. Phys. D: Appl. Phys.* **47** 255201 (16pp)

[8] Yang A, Liu Y, Sun B, Wang X, Cressault Y, Zhong L, Rong M, Wu Y and Niu C 2015 Thermodynamic properties and transport coefficients of high-temperature CO$_2$ thermal plasmas mixed with C$_2$F$_4$ *J. Phys. D: Appl. Phys.* **48** 495202 (25pp)

[9] Sun H, Rong M, Wu Y, Chen Z, Yang F, Murphy A B and Zhang H 2015 Investigation on critical breakdown electric field of hot carbon dioxide for gas circuit breaker applications *J. Phys. D: Appl. Phys.* **48** 055201 (16pp)

[10] Guo X, Li X, Murphy A B and Zhao H 2017 Calculation of thermodynamic properties and transport coefficients of CO$_2$-O$_2$-Cu mixtures *J. Phys. D: Appl. Phys.* **50** 345203 (12pp)

[11] Kieffel Y, Biquez F and Ponchon P 2015 Alternative gas to SF$_6$ for use in high voltage switchgears: g^3 *23rd International Conference on Electricity Distribution* Paper0230

[12] Hyrenbach M, Hintzen T, Müller and Owens J 2015 Alternative gas insulation in medium-voltage switchgear *Proc. 23rd Int. Conf. on Electricity Distribution* Paper0587

[13] Wu Y, Wang C, Sun H, Mingzhe R, Murphy A B, Li T, Zhong J, CHen Z, Yang F and Niu C 2017 Evaluation of SF$_6$-alternative gas C5-PFK based on arc extinguishing performance and electric strength *J. Phys. D: Appl. Phys.* **50** 385202 (15pp)

[14] Li X, Guo X, Murphy A B, Zhao H, Wu J and Guo Z 2017 Calculation of thermodynamic properties and transport coefficients of C$_5$F$_{10}$O-CO$_2$ thermal plasmas *J. Appl. Phys.* **122** 143302 (11pp)

[15] Rabie M and Franck C M 2018 Assessment of Eco-friendly Gases for Electrical Insulation to Replace the Most Potent Industrial Greenhouse Gas SF$_6$ *Environ. Sci. Technol.* **52** pp.369-380

[16] 3M 2015 3M^{TM} Novec^{TM} 4710 Insulating Gas Data Sheet

[17] 3M 2015 3M^{TM} Novec^{TM} 5110 Insulating Gas Data Sheet

[18] Seeger M, Smeets R, Yan J, Ito H, Claessens M, Dullni E, Falkingham L, Franck C M, Gentils F, Hartmann W, Kieffel Y, Jia S, Jones G, Mantilla J, Pawar S, Rabie M, Robin-Jouan P, Schellekens H, Spencer J, Uchii T, Li X and Yanabu S 2017 Recent Trends in Development of High Voltage Circuit Breakers with SF$_6$ Alternative Gases *Plasma Physics and Technology Journal* **4**(1)

[19] Saxegaard M, Attar E, Kristoffersen M, Landsverk H, Granhaug O, Di-Gianni A and Scheel S 2017 Low-current interruption in SF$_6$-alternatives *Proc. 24th Int. Conf. on Electricity Distribution*, pp.286-288

[20] Kosse S, Nikolic P G and Kachelriess G 2017 Holistic evaluation of the performance of today's SF$_6$ alternatives proposals *Proc. 24th Int. Conf. on Electricity Distribution*, pp.210-213

[21] Beroual A and Haddad A 2017 Recent Advances in the Quest for a New Insulation Gas with a Low Impact on the Environment to Replace Sulfur Hexafluoride (SF$_6$) Gas in High-Voltage Power Network Applications *Energies* **10**(8) 1216

[22] Crawford F W and Edels H 1960 The Reignition Voltage Characteristics of Freele Recovering Arcs *Proceedings of the IEE - Part A: Power Engineering* **107**(32) pp.202-212

[23] Edels H and Ettinger Y 1962 Arc interruption and thermal reignition *Proceedings of the IEE - Part A: Power Engineering* **109**(43) pp.89-98

[24] Edels H and Fenlon F H 1963 A theory of interruption and thermal-arc reignition *Proceedings of the IEE - Part A: Power Engineering* **110**(11) pp.2082-2092

[25] Edels H, Whittaker D, Evans K G and Shaw A B 1965 Experiments and theory on arc reignition by spark breakdown *Proceedings of the IEE* **112**(12) pp.2343-2352

[26] Murooka Y and Hearne K R 1972 Measurement of Arc Electrode Temperatures and Reignition Characteristics *J. Appl. Phys.* **43**(6) pp.2656-2663

[27] Paul K C, Dawson F P and Sakuta T 2002 Dynamic current-zero behaviour of wall-stabilised arc in different arc-quenching media *IEE Proceedings - Generation, Transmission and Distribution* **149**(5) pp.510-516

[28] Tanaka Y and Suzuki K 2017 Non-Equilibrium Effects on SF_6 Arc Plasmas in Decaying Phases 3rd *International Conference on Electric Power Equipment - Switching Technology ICEPE-ST2015 (Busan, Korea)* GO-181

[29] Zhang J F, Fang M T C and Newland D B 1987 Theoretical investigation of a 2 kA arc in a supersonic nozzle *J. Phys. D: Appl. Phys.* **20** 368-379

[30] Liu J, Zhang Q, Yan J D, Zhong J and Fang M T C 2016 Analysis of the characteristics of DC nozzle arcs in air and guidance for the search of SF_6 replacement gas *J. Phys. D: Appl. Phys.* **49** 435201 (19pp)

[31] Murai K, Nakano T, Tanaka Y, Uesugi Y, Ishijima T, Tomita K, Suzuki K, Iijima T and Shinkai T 2016 The LTE thermofluid simulation of Ar/SF_6 gas-blast arcs in a nozzle space in an arc device *IEEJ Trans. PE* **136**(9) pp.741-748

[32] Sun H, Tanaka Y, Tomita K, Wu Y, Rong M, Uesugi Y and Ishijima T 2015 Computational non-chemically equilibrium model on the current zero simulation in a model N_2 circuit breaker under the free recovery condition *J. Phys. D: Appl. Phys.* **49** 055204 (17pp)

[33] Tanaka Y, Nakano T, Shimizu T, Tomita K and Fujino T and Suzuki K 2015 Fundamental Investigation Technique on Gas-Blast Arc Behaviors in Decaying Re-ignition Processes using Power Semiconductors *Trans.IEEJ* **135**(1) 1-8

[34] Nakano T, Murai K, Tanaka Y, Uesugi Y, Ishijima T, Shiraishi T, Shimizu T, Tomita K, Suzuki K and Shinkai T 2015 Evaluation on Current Interruption Ability of CO_2 and SF_6 using Current and Voltage Application Highly Controlled by Power Semiconductors 3rd *International Conference on Electric Power Equipment - Switching Technology ICEPE-ST2015 (Busan, Korea)* GO-438

[35] Nakano T, Murai K, Tanaka Y, Uesugi Y, Ishijima T, Shiraishi T, Shimizu T, Tomita K, Suzuki K and Shinkai T 2016 Evaluation on Current Interruption Ability of Various Gases using Current and Voltage Application Highly Controlled by Power Semiconductors 21th *International Conference on Gas Discharges and their Applications GD2014 (Nagoya, Japan)* A25 pp.97-100

[36] Nakano T, Tanaka Y, Murai K, Uesugi Y, Ishijima T, Tomita K, Suzuki K and Shinkai T 2017 Evaluation of arc quenching characteristics of various gases using power semiconductors *J. Phys. D: Appl. Phys.* **50** 485602 (16pp)

[37] Tomita K, Gojima D, Nagai K, Uchino K, Kamimae R, Tanaka Y, Suzuki K, Iijima T, Uchii T and Shinkai T 2013 Thomson scattering diagnostics of decay processes of Ar/SF_6 gas-blast arcs confined by a nozzle *J. Phys. D: Appl. Phys.* **46** 382001 (5pp)

[38] Tomita K, Gojima D, Shimizu T, Uchino K, Nakano T, Tanaka Y, Suzuki K, Iijima T and Shinkai T 2015 Thomson scattering diagnostics of SF_6 gas-blasted arcs confined by a nozzle under free-recovery conditions *J. Phys. D: Appl. Phys.* **48** 265201 (14pp)

[39] Inada Y, Kumada A, Ikeda H, Hidaka K, Nakano T, Murai K, Tanaka Y and Shinkai T 2017 Comparative study on extinction process of gas-blasted air and CO_2 arc discharge using two-dimensional electron density imaging sensor *J. Phys. D: Appl. Phys.* **50** 175202

[40] Seeger M, Schwinne M, Bini R, Mahdizadeh N and Votteler T 2012 Dielectric recovery in a high-voltage circuit breaker in SF_6 *J. Phys. D: Appl. Phys.* **45** 395204 (12pp)

Chapter 5

Conclusions

5.1 Introduction

This thesis reported fundamental study about arc quenching technique using solid and gas media. Arc quenching technique is essential for current interruption in a circuit breaker. As an arc quenching medium, solid polymer material can be used due to its potential gas blast ability when it contacts the arc plasma. The author further proposed to apply "spallation" phenomena, which occurs only from polyamide materials. With occurrence of spallation, small polymeric particles can jump into the arc plasma and quench the arc from inside of the arc by thermal decomposition. Discovery of spallation phenomena can lead to improvement of current interruption performance of low voltage circuit breakers.

In addition to solid phase media, gas phase media are important for arc quenching, especially in high voltage gas circuit breakers. SF_6 is existent arc quenching gas due to its extremely high quenching performance. However, SF_6 also has a high global warming potential (GWP) that is 22800 times higher than that of CO_2. Thus, use of SF_6 has been desired to be reduced. One of the solution is development of alternatives to SF_6. There are already strong candidates such as CO_2 + perfluoronitrile, so called g^3. However, further understanding of arc quenching process is necessary because there are still many uncleared issues. In this work, fundamental characteristics of decaying arcs and re-igniting arcs were investigated and quenching performances of various gases were compared. Waveforms measurement, high speed video camera observation, electron density measurement were conducted to SF_6, CO_2, O_2, N_2, air and Ar-blast arcs.

This chapter presents the results derived in this thesis briefly in the following section.

5.2   Summary of results

5.2.1   Spallation occurrence from polyamide during thermal plasma irradiation

In this chapter, water absorption properties of polyamide materials were investigated at first. Water absorption into polyamide materials causes ejection of small polymer particles from the surface when a high heat flux is irradiated to the water absorbed polyamide specimen. The author discovered this phenomenon in this work and named "spallation". If spallation is applied to arc quenching, polymer particles can jump into the arc and quench the arc from the inside effectively. In the experiment, as imitated arc plasmas, inductively coupled thermal plasmas were irradiated to water absorbed polyamide specimens with inclusion of N_2 and O_2. The results showed that O_2 inclusion to the plasma enhances occurrence of spallation significantly. Therefore, spallation can be applied to effective quenching of air arcs. The author further estimated cooling effects of spallation particles on a 10 cc volume of hot air. Solving energy conservation equation, the author estimated that cooling effects of 10 spallation particles on 10 kK hot air will be 3000 K of decrease from the initial temperature. It can be thought to be enough large effect for air arc quenching, the author expects spallation phenomena to be applied to arc quenching in a low voltage circuit breaker.

5.2.2   Evaluation of arc quenching characteristics of various gases

This chapter presented arc quenching characteristics of SF_6, CO_2, O_2, N_2, air and Ar gas. The gas to be tested was blown to the arc in DC 50 A and at the specified time, the arc current was intentionally decreased steply to 0 A. At that time the arc current was controlled by one of power semiconductor, an insulated gate by-polar transistor (IGBT) that can be drive in a micro second of accuracy. In this situation, the blast gas quenched the arc without energy input to the arc under free recovery condition. The author observed the arc behaviour using a high speed video camera and measured electron density using laser Thomson scattering (LTS) method to identify the arc quenching characteristics of the blast gas. The IGBT can not only translocate the current to itself but also return back

the current to the arc. When the current is returned back to the decaying arc, transient voltage appears between the electrode, that was named "quasi-TRV" in this work. The quasi-TRV can be applied to decaying arcs at any specified delay time t_d from initiation of the arc decaying. Using this technique, current interruption tests were conducted. The test results indicated that arc quenching performance of SF_6 is 4 times higher than that of CO_2, which is derived by the result that SF_6 took 28 μs to have 50% probability of interruption and CO_2 took 110 μs to have same probability. The author also confirmed rapid decrease in radiation intensity and electron density in SF_6-blast arc in the decaying phase. In this way, arc quenching characteristics were quantitatively evaluated through the experiments.

5.2.3 Fundamental study on thermal re-ignition process of various gas-blast arcs

In this chapter, SF_6, CO_2, O_2, N_2, air and Ar gas-blast arcs were intentionally re-ignited by quasi-TRV application and waveforms measurement, high speed video camera observation and electron density measurement were conducted. From the measured waveforms of the arc current and voltage, dielectric recovery properties of F_6, CO_2, air and Ar gas-blast arcs were obtained. In addition, sequencing pictures from arc decaying to arc re-ignition were observed that can be used for consideration of arc behaviours of each gas-blast arc. Furthermore, the sequence of electron density at the nozzle throat from arc decaying to re-ignition was obtained for each gas-blast arc. There are still only a few information of precise measured data of electron density of the arc at the nozzle throat. Therefore, the obtained data in this work is quite important for consideration of transient behaviour of gas-blast arcs. This work clarified that dielectric recovery of a SF_6-blast arc rapidly progresses from 20 μs after initiation of the arc decaying and a CO_2-blast arc have an similar inflection point around 80 μs.

5.3 Scope of future researches

This work covered only proposal of a new arc quenching technique using polyamide materials, evaluation of fundamental arc quenching ability of gases and fundamental study

of re-ignition processes of gas-blast arcs. The outcome in this work was obtained with inductively coupled thermal plasmas or small direct current arc, which are different from a high current arc. Not only fundamental ones, but also more practical studies should be conducted in a future. Thus, following issues are necessary to be considered as future work:

(1) Application test of spallation to AC/DC current interruption

Occurrence of "spallation" is confirmed when a water absorbed polyamide material is irradiated by an inductively coupled thermal plasma. Current interruption tests assisted by spallation phenomena should be conducted to have practical information. Spallation phenomena can be expected to be applied to both AC current and DC current interruption. The experimental devices for consideration of AC and DC arc quenching effects have been already developed. Our future works include investigation of dielectric recovery property of air arc affected by water absorbed polyamide materials, probability of current interruption, high speed video camera observation and electron density measurement on transient arc quenched by polymer ablation and spallation.

(2) Higher voltage application as quasi-TRV

In this work, transient recovery voltage (TRV) was imitated by quasi-TRV. The peak voltage of quasi-TRV was 1.2 kV in this work. This voltage is acceptable in consideration of thermally re-ignition of arcs. Now higher peak voltage up to 8 kV is available. The peak voltage has been increased without degradation of time accuracy. Using the new quasi-TRV, not only thermally re-ignition but also spark break down re-ignition can be engendered by the higher peak voltage. It leads to further understanding of dielectric recovery properties of various types of arcs including gas-blast arcs and polymer ablation or spallation assisted decaying arcs.

(3) Arcing tests in a half-cycle AC current

This work used DC 50 A of well-controllable current for the arc experiments for reproducibility and stability of generated arcs. This concept is fundamentally important for comparison between experimental and numerical results. In addition to this, the magnitude of current is also important in terms of consideration of short circuit current interruption. The author has developed a half cycle AC current generator that has a peak of more than 1 kA and frequency of 50 Hz. The half cycle AC current can be injected to various electric conductors, including arcs, with accuracy in time of micro seconds. It helps to understand

arc behaviour in an AC large current, especially around current zero. Dielectric recovery properties of various gas-blast AC arcs after current zero will be investigated in a future.

(4) Current interruption tests with large flow rate gas-blast

Gas circuit breakers (GCBs) blow arc-quenching gas to the arc for current interruption. The practical blast gas flow rate is much higher than that in the experiments in this work. Lower gas flow rates contributed to less turbulent effects and thus high reproducibility of the gas-blast arcs. However, large flow rate gas-blast is also necessary to examine current interruption performance of the blast gas because weak gas flow can't interrupt the current. Accordingly, the author developed gas-blast system that can blow gases with back pressure of 700 kPa and flow rate of about 50 L/s = 3000 L/min. Gas blast timing can be set to specified value and time jitters are less than 1 ms. Combination of this gas-blast system and the half cycle AC current injection system described above can imitate AC current interruption in a GCB practically.